Remote sensing of phytoplankton in the Arctic Ocean : development, tuning and evaluation of new algorithms

Thèse en cotutelle
Doctorat interuniversitaire en océanographie

Juan Li

Université Laval
Québec, Canada
Philosophiæ doctor (Ph. D.)

et

Wuhan University
Wuhan,Chine

© Juan Li, 2022

Remote sensing of phytoplankton in the Arctic Ocean: development, tuning and evaluation of new algorithms

Thèse en cotutelle
Doctorat en Océanographie

Juan Li

Sous la direction de:

Marcel Babin, directeur de recherche
Xiaoping Pang, directrice de cotutelle

Résumé

Au cours des dernières décennies, l'augmentation de la production primaire (PP) dans l'océan Arctique (AO) a en partie été associée à une augmentation de la biomasse phytoplanctonique, comme l'ont montré des études de télédétection. La concentration en chlorophylle a (Chl), un indicateur de la biomasse phytoplanctonique, est un facteur clé qui peut biaiser les estimations de la PP quand elle comporte des erreurs de mesure. En d'autres mots, une estimation précise de la Chl est cruciale pour améliorer notre connaissance de l'écosystème marin et de sa réponse au changement climatique en cours. Cependant, la télédétection de la couleur de l'océan dans l'océan Arctique présente plusieurs défis. Tout d'abord, il est bien connu que l'échec des algorithmes standards de la couleur de l'océan dans l'AO est dû à l'interférence des matières colorées et détritiques (CDM) dans le spectre visible, mais comment et dans quelle mesure cela va biaiser l'estimation de la Chl reste inconnu. En outre, la Chl étant un facteur clé utilisé pour estimer la PP, la propagation des erreurs des estimations de la Chl aux estimations de la PP doit être évaluée. Le dernier mais le plus important est qu'un algorithme robuste avec une incertitude raisonnable, en particulier pour les eaux côtières complexes et productives, n'est pas encore disponible. Pour résoudre ces problèmes, dans cette étude, nous avons d'abord compilé une grande base de données bio-optiques in *situ* dans l'Arctique, à partir de laquelle nous avons évalué de manière approfondie les algorithmes de couleur de l'océan actuellement disponibles du point de vue des impacts des CDM. Nous avons constaté que plus le niveau de CDM par rapport à la Chl dans la colonne d'eau était élevé, plus il biaisait les estimations de la Chl. L'analyse de sensibilité des estimations de la PP sur la Chl a montré que l'erreur des estimations de la Chl était amplifiée de 7% lorsqu'elle était passée dans l'estimation du PP en utilisant un modèle de PP résolu spectralement et verticalement. En outre, pour obtenir de meilleurs résultats, nous avons optimisé un algorithme semi-analytique (Garver-Siegel-Maritorena, GSM) pour l'AO en ajoutant la bande spectrale de 620 nm qui est moins affectée par le CDM et le signal ici est généralement élevé pour les eaux riches en CDM, devenant anisi important pour le GSM afin d'obtenir des estimates précises de la Chl. Notre algorithme ajusté, GSMA, n'a amélioré la précision que de 8% pour l'AO, mais l'amélioration pour les eaux côtières a atteint 93%. Enfin, étant donné que les algorithmes qui n'exploitent pour la plupart que les parties bleue et verte du spectre visible sont problématiques pour les eaux très absorbantes/obscures, nous avons introduit un modèle d'émission de fluorescence pour tenir compte des propriétés bio-optiques du phytoplancton dans la partie rouge du spectre visible. En se couplant avec le GSMA, le nouvel algorithme à spectre complet, FGSM, a encore amélioré la précision des estimations de la Chl de ~44% pour les eaux eutrophes. À l'avenir, des couplages sont nécessaires à des fins de validation en ce qui concerne l'application satellitaire. De plus, de nouvelles approches pouvant être appliquées pour détecter le maximum de chlorophylle sous la surface (SCM), les efflorescences en bordure de glace et/ou sous la glace, les types fonctionnels de phytoplancton (PFT), sont attendues.

Abstract

In the recent decades, the raise of primary production (PP) in the Arctic Ocean (AO) is mainly driven by the increase of phytoplankton biomass as multiple remote sensing studies have suggested. Chlorophyll *a* concentration (Chl), a proxy of phytoplankton biomass, is a key factor that biases PP estimates. In terms of bottom-up control, accurate Chl estimate is crucial to improve our knowledge of marine ecosystem and its response to ongoing climate change. However, there are several challenges of ocean color remote sensing in the Arctic Ocean. Firstly, it is well known that the failure of standard ocean color algorithms in the AO is due to the interference of colored and detrital material (CDM[1]) in the visible spectrum, but how and to what extend it will bias the estimation of Chl remains unknown. Besides, Chl as a key factor used to estimate PP, error propagation from Chl estimates to PP estimates needs to be assessed. The last but most important is that a robust algorithm with reasonable uncertainty, especially for the complex and productive coastal waters, is not yet available. To address these problems, in this study, we first compiled a large Arctic in *situ* bio-optical database, based on which we thoroughly evaluated presently available ocean color algorithms from a perspective of the impacts of CDM. We found that the higher the level of CDM relative to Chl in the water column, the larger it would bias Chl estimates. Sensitivity analysis of PP estimates on Chl showed that the error of Chl estimates was amplified within 7% when passed into the estimation of PP using a spectrally- and vertically-resolved PP model. Besides, to obtain better results, we tuned GSM for the AO by adding 620 waveband which is less affected by CDM and the signal here is generally high for CDM-rich waters thus become important for GSM to retrieve accurate Chl estimates. Our tuned algorithm, GSMA, merely improved the accuracy by 8% for the AO, but the improvement for coastal waters reached up to 93%. Finally, given that algorithms that only exploits visible spectrum are problematic for highly-absorbing/dark waters, we introduced the fluorescence emission model to account for the bio-optical properties of phytoplankton in the near infrared spectrum. By coupling with GSMA, the novel full-spectrally algorithm, FGSM, further improved the accuracy of Chl estimates by ~44% for eutrophic waters. In the future, matchups are needed for validation purposes with respect to satellite application. Moreover, new approaches that can be applied to detect subsurface chlorophyll maximum (SCM), ice-edge and/or under-ice blooms, phytoplankton functional types (PFT) and so on are expected.

[1] The term CDM used in this study is refer to the combination of colored dissolved organic matter and non-algae particles.

Table des matières

Liste des figures

Liste des tableaux

Liste des abréviations et symboles

Abréviation	Définition
AO	Arctic Ocean
AOP	Apparent Optical Property
AUV	Autonomous Underwater Vehicle
BGC-Argo	Biogeochemical-Argo floats
C2RCC	Case 2 Regional Agency
OC-CCI	Ocean Color Climate Change Initiative
CDM	Colored and Detrital Material
CDOM	Colored Dissolved Organic Matter
CF	Cost Function
Chl	Chlorophyll a concentration
COASTlOOC	Coastal Surveillance Through Observation of Ocean Color
C-OPS	Compact Optical Profiling System
DOC	Dissolved Organic Carbon
ESA	European Space Agency
FLH	Fluorescence Line Height
GIOP	Generalized Inherent Optical Property model
GSM	Garver, Siegel, and Maritorena model
HPLC	High Performance Liquid Chromotography
LIDAR	Light Detection and Ranging
IOCCG	The International Ocean-Colour Coordinating Group
IOP	Inherent Optical property
MAE	Mean Absolute Error
MAPD	Mean Absolute Percentage Error
MERIS	Medium Resolution Imaging Spectrometer
MIZ	Marginal Ice Zone

MODIS	Moderate Resolution Imaging Spectroradiometer
NAP	Non-algae Particulate
NN	Neural Network
OCRS	Ocean Color Remote Sensing
OLCI	Ocean and Land Colour Instrument
ONNS	OLCI Neural Network Swarm
PAR	Photosynthetically Active Radiation
PFT	Phytoplankton Functional Type
PP	Primary Production
PPARR	Primary Production Algorithm Round Robin activity program
PUR	Photosynthetically Usable Radiation
QAA	Quasi-analytical Algorithm
RMA	Reduced Major Axis
RMSE	Root Mean Square Error
ROV	Remotely Operated Vehicle
RTE	Radiative Transfer Equation
SCM	Subsurface Chlorophyll Maximum
SeaWiFS	Sea-viewing Wide Field-of-view Sensor
SICF	Sun-induced Chlorophyll a Fluorescence
WARM	Warming and Irradiance Measurements buoy system
TOA	Top-of-Atmosphere
VIIRS	Visible Infrared Imaging Radiometer Suite

Avant-propos

This thesis has five sections: a general introduction, three chapters of scientific results in the form of articles, and a general conclusion. The three chapters of scientific results are written for publication in peer-reviewed journals. They are supposed to submitted shortly. My role in the preparation of these articles was to conceptualize the studies, compile the available Arctic datasets, conduct the associated analyses, integrate with previous research, present and discuss the results, and reflect on future efforts.

Li J., Matsuoka A., Pang X., and Babin M. (2022), Performance of algorithms for retrieving chlorophyll-a concentrations in the Arctic Ocean: impact on primary production estimates, Article in preparation.

Li J., Matsuoka A., Hooker S.B., Pang X., and Babin M. (2022), A newly tuned algorithm for the Arctic Ocean: a preliminary solution for CDM-rich waters, Article in preparation.

Li J., Matsuoka A., Hooker S.B., Pang X., and Babin M. (2022), A novel coupled full-spectral chlorophyll a algorithm: a fluorescence-based approach, Article in preparation.

Introduction

Changes in the AO

Climate change has influenced a wide spectrum of marine, cryospheric, terrestrial, and atmospheric environments, especially in the Arctic Ocean (AO), which is one of the most sensitive areas to the ongoing climate change. It has been evidenced that temperatures in the Arctic have increased more than twice as fast as the global average (AMAP, 2017; Cohen et al., 2014; Screen and Simmonds, 2010; Serreze et al., 2009). As a consequence, Arctic sea ice extent has been shrinking in all seasons over the last 4 decades (Onarheim et al., 2018), particularly during summer by nearly 40% (Comiso et al., 2008; Stroeve et al., 2007; Stroeve et al., 2012). It is predicted that there will be near ice-free summer conditions sometime in the coming decades (Serreze et al., 2007) or even much earlier (Wang and Overland, 2012). Sea ice is also thinning (Lindsay and Schweiger, 2015) and becoming more dominated by younger ice types (Comiso, 2012; Maslanik et al., 2011; Parkinson and Comiso, 2013). In addition to changes in space, on temporal scale, Bliss and Anderson (2014) and Stroeve et al. (2014) have observed an earlier onset of ice surface melt and a longer melt season. The increased melt season length is due to later freeze up more than to earlier melt onset, but the earlier melt onset is more important in terms of the input of solar radiation to the sea ice (Perovich et al., 2011). On average, the melt season has been documented to be lengthened by 5 days per decade, and for coastal regions, the increase in the length of melt season reaches up to 11 days per decade (AMAP, 2017). These changes in the AO are manifested due to Arctic Amplification and associated feedback. For instance, the dark melted surface areas with significant lower albedo absorb more solar energy, offering a positive feedback to the loss of sea ice (Flanner et al., 2011; Wadhams, 2012). As a consequence, the under-water light fields are experiencing pronounced alterations, which impact marine ecosystem dynamics (Ardyna and Arrigo, 2020).

The AO contains only 1% and 3% of the global seawater volume and area respectively, but is receiving 11% of the world's river flow (Carmack et al., 2016; Lammers et al., 2001). Its drainage basin covers 19 million km^2, even larger than the AO area (14.2 million km^2), making it the most river-influenced and landlocked of all oceans (Lammers et al., 2001; Vörösmarty et al., 2000). Annual mean freshwater input to the AO is dominated by river discharge (38%) which has been reported to increase over most of the Arctic (Feng et al., 2021; Overeem and Syvitski, 2010; Peterson et al., 2002). The rising sea level (Church et al., 2013) and increasing storm surges (Vermaire et al., 2013) are putting coastal areas at greater risk of erosion. Accompanied by the melt of ice sheets, glaciers and permafrost, large amounts of terrestrial materials across various vegetation and soil types from the Arctic watersheds are now delivered by river runoff into the AO, replenishing the water bodies with nutrients and complicating water optical properties by various intricate biogeochemical processes.

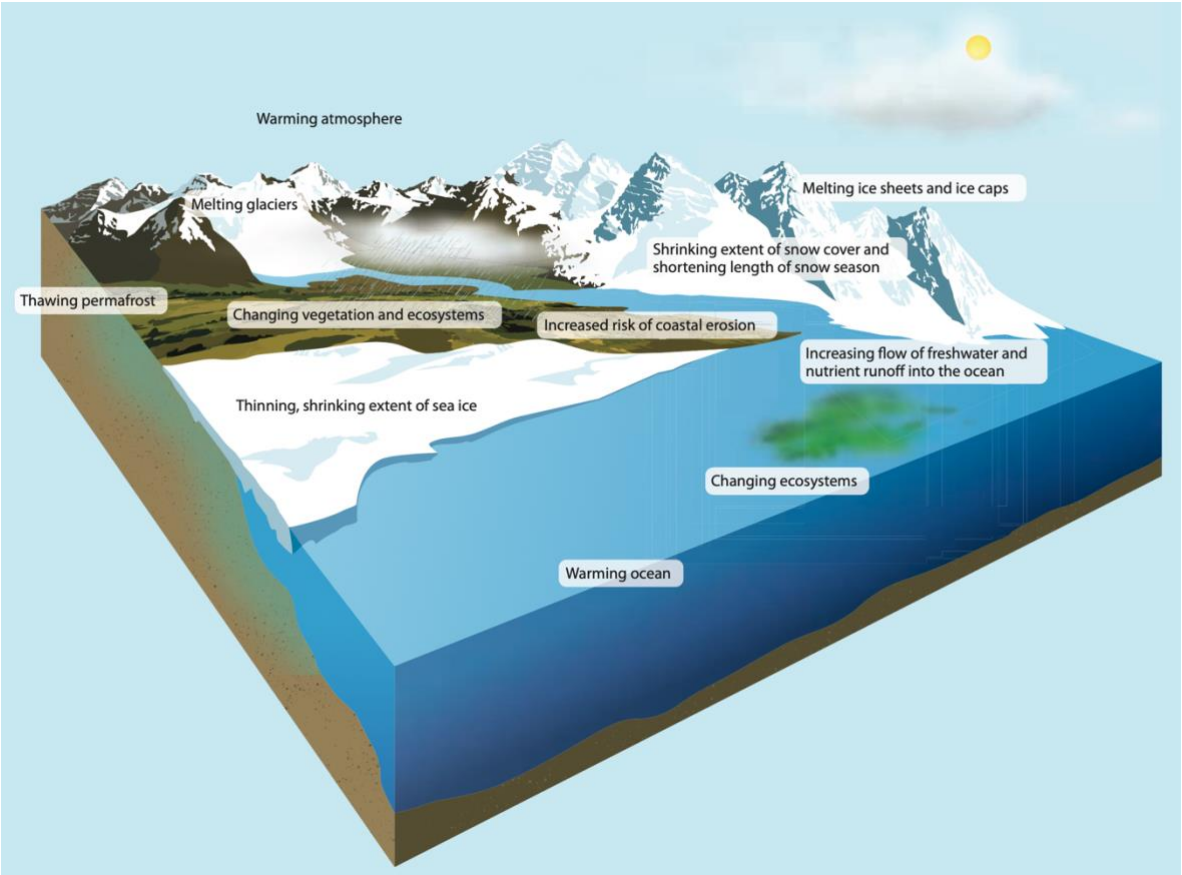

Figure 0.1 Schematic representation of major observed changes in the Arctic caused by global warming (AMAP, 2017).

However, changes in the AO are wide in scope. As sea ice extent in the AO continues to decrease, light penetration into the ocean increases, accompanied by a long-term increase in river discharge containing significant amounts of organic and inorganic materials (Frey and McClelland, 2009). Annual primary production (PP) of the AO has been reported to increase as a series of ocean color remote sensing studies suggest (Ardyna and Arrigo, 2020; Arrigo and van Dijken, 2015; Bélanger et al., 2013b; Pabi et al., 2008). In the period from 1988~2012, the increase of PP was driven primarily by the loss of sea ice (Figure 0.2). The increased open-water habitat incubated more phytoplankton, accompanied with longer growing season. The pan-Arctic PP in the open water has increased by 30% from 1998~2012 (Arrigo and van Dijken, 2015). While from 2012~2018, without significant change in both open-water phytoplankton habitat and the length of growing season, the entire Arctic annual PP increased at a rate of 13.5 TgC yr^{-1}, which was twice of that during the period from 1998~2012 (Ardyna and Arrigo, 2020; Lewis and Arrigo, 2020). The faster increase of PP during this period was highly correlated to the increase of phytoplankton biomass likely resulting from increased nutrient supplies, indicating that the controlling factor of PP switched from the loss of sea ice (1988~2012) to the increase of phytoplankton biomass (2012~2018) (Ardyna and Arrigo, 2020).

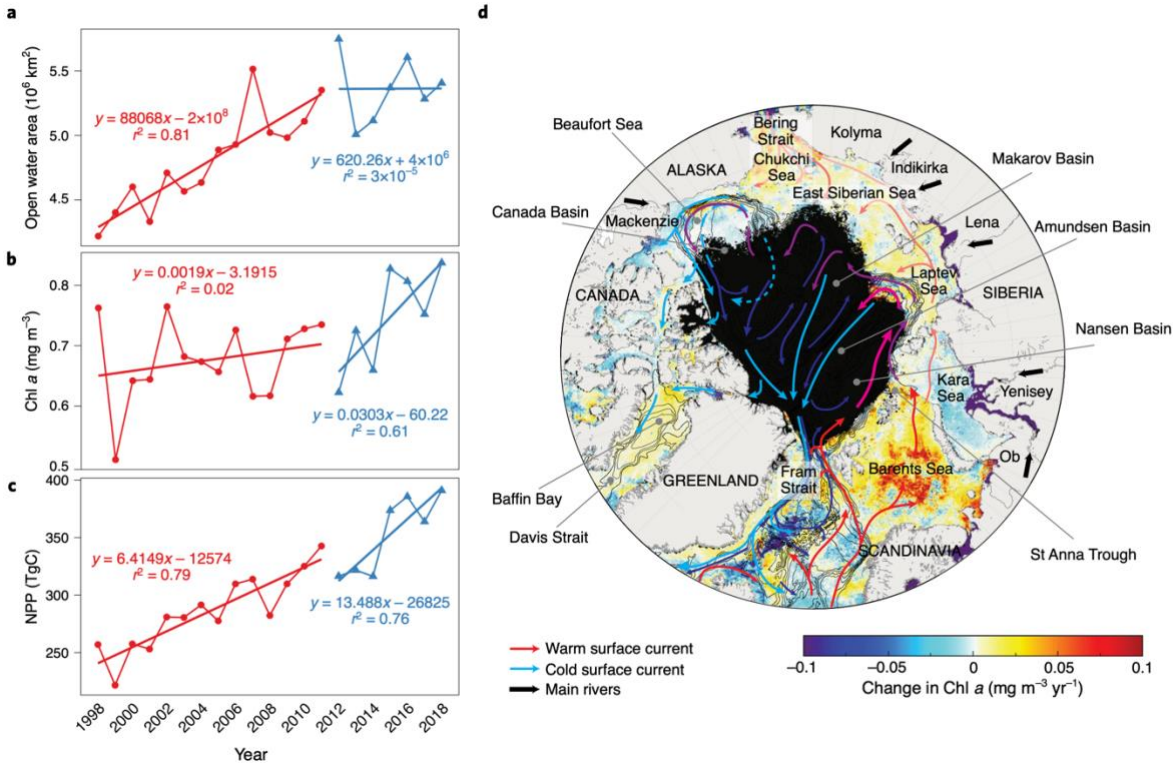

Figure 0.2 Global trends in Arctic primary production over the last two decades. a–c, Annual time series of Arctic Ocean mean open-water area (a), mean Chl (b) and NPP (c). The time series is separated into two time periods because from 1998–2012, loss of sea ice was responsible for the increase in NPP for the Arctic Ocean. After that time, the loss of sea ice slowed considerably but NPP continued to increase. This increase from 2012–2018 was due primarily to an increase in phytoplankton biomass, likely because of increased nutrient supply into Arctic surface water. (d) Map showing the rate of change in Chl (mg m^{-3} yr^{-1}) between 1998 and 2018. (Ardyna and Arrigo, 2020)

Phytoplankton

Phytoplankton are photosynthesizing microorganisms that inhabit the sunlit top layers of oceans. They harvest light to create organic compounds from carbon dioxide dissolved in the water. As primary producers, phytoplankton form the base of the marine food web and are responsible for energy transfer to higher trophic levels. They only take up 1% of the global plant biomass, but account for about half of global photosynthetic activity and at least half of the oxygen production (Chapman, 2013). Through photosynthesis, inorganic carbon is fixed into organic matter, some of this carbon is carried to the deep ocean when phytoplankton die, and some is transferred to different layers of the ocean as phytoplankton are eaten by other creatures. After a series of biological processes, carbon are then sequestered away from the atmosphere into the deep ocean. Worldwide, this "biological carbon pump" transfers about 11 gigatonnes of carbon from the atmosphere to the deep ocean each year (Basu and Mackey, 2018). Even small changes in the growth of phytoplankton may affect atmospheric carbon dioxide concentrations, which would in return impact global warming through associated feedback.

Chlorophyll *a*, the primary pigment for photosynthesis of organic carbon in the ocean, can be found in all phytoplankton species. Chlorophyll *a* concentration (Chl), a proxy of phytoplankton biomass, is widely used for primary productivity studies to evaluate the aquatic ecosystems and monitoring eutrophication (Ardyna and Arrigo, 2020; Arrigo and van Dijken, 2015; Bélanger et al., 2013a). The main uncertainty in primary production estimates obtained using ocean color remote sensing lies in the most important input Chl (Bélanger et al., 2013a; Mustapha et al., 2012). Therefore, accurate estimation of Chl is crucial for a better understanding of spatio-temporal trends of primary production over recent decades as a consequence of climate change.

Challenges in satellite-based surface chlorophyll *a* concentration retrieval

Due to the harsh environment, logistical difficulties, and cost constraints, in *situ* measurements in the AO are scarce. But they are of significant importance as they provide the most accurate data required for calibration and validation of airborne and satellite observations. In this context, ocean color remote sensing (OCRS) has become a powerful tool for providing a quantitative assessment of the biological state of the surface ocean at synoptic and temporal scales inaccessible from traditional field observations, and it has been used extensively by oceanographers. Even though, OCRS has its limitations when applied to the Arctic Ocean.

Challenges in data acquisition

Prevailing low solar elevations

The Sun zenith angle in the Arctic is often larger than 70°. Due to relative larger pathlength, water-leaving signal in the blue band reached at sensor in the space accounts less than 10% of the total signal. Therefore, higher accuracy of atmospheric correction in the AO is required, which is still a challenge and needs to be addressed.

Persistence of clouds and fog

AO is located in the sub-polar low pressure systems, associated with heavy cloud cover and substantial precipitation in all seasons. The mixed-phase clouds are largely distributed and can persist several days which influences solar radiation field. As a consequence, strict cloud filters are needed to avoid any cloud contamination during the process of atmospheric correction. In addition, fog develops near the sea surface when sea ice starts to melt. These features impact ocean color data availability which may make it difficult to monitor changes in the Arctic Ocean over short time scales (Perrette et al., 2010).

Impact of ice on remotely sensed reflectance

Sea ice has a bright surface, 80% of the sunlight that strikes it is reflected back into space. The resulting sea ice adjacency and sub-pixel ice contamination presents problems when deriving ocean color products. Adjacency effect enhances the water-leaving reflectance toward the shorter wavelength, leading to an underestimation of Chl. Sub-pixel contamination by sea ice depends on the type and age of sea ice. It tends to be seen as an aerosol

resulting in overcorrection in the blue band, and consequently leads to an overestimation of Chl (Wang et al., 2009). But the extent of these impacts in the Arctic Ocean Color studies remains poorly known.

Complex optical properties

Besides challenges with regard to data acquisition from space by ocean color sensors, the main problems that must be overcome in order to derive accurate observation of Chl are associated with the complex optical properties of the AO, that is higher package effects of phytoplankton pigments (Cota et al., 2004; Matsuoka et al., 2011; Matsuoka et al., 2007) and high proportion of colored dissolved organic matter (CDOM) (Bélanger et al., 2008; Matsuoka et al., 2013, 2012; Matsuoka et al., 2011; Matsuoka et al., 2007) observed in the AO.

Higher package effect

As a consequence of photoacclimation to low irradiance in the Arctic, phytoplankton cells often exhibit high intracellular pigment concentrations (Falkowski and Owens, 1980) which decreases the efficiency of light absorption. This phenomenon, known as package effect (Falkowski et al., 1985), generally strengthens with the increase of cell size and intracellular pigment concentrations, making the chlorophyll-specific phytoplankton absorption coefficient (a_{ph}^*, defined as phytoplankton absorption coefficient a_{ph} normalized by Chl) a nonlinear function of Chl (Morel and Bricaud, 1981). Figure 0.3 illustrates the relationships between $a_{ph}(440)$ and Chl for various water bodies. Red, green, blue, and black lines refer to the relationships obtained from various areas of world ocean (Bricaud et al., 1998), the Labrador Sea (Cota et al., 2003), the Beaufort and Chukchi Seas (Wang et al., 2005), and western Arctic Ocean (Matsuoka et al., 2007) respectively. It can be seen that the black and blue lines belonging to the AO lie below the others corresponding to lower latitude waters, indicating the mean a_{ph}^* is generally lower in the AO, which is also an evidence suggesting that package effects in the AO is relative higher than that in lower latitude waters.

This higher package effect flattens the absorption spectrum of chlorophyll a especially at the blue absorption peak. As a consequence, when applying global empirical algorithms to the AO, relatively larger decrease of a_{ph}^* at blue wavelengths than green wavelengths yields larger maximum blue-to-green band ratio, which will lead to a certain underestimation of Chl (Lewis et al., 2016).

CDOM-dominated optical property

The AO receives the largest amount of river discharge relative to its volume (11% of global river discharge but its volume is only 1% of global ocean, Carmack et al., 2016), and its drainage basin is even larger than its area, making it characterized by high CDOM relative to other optically significant components when compared to the other oceans. In addition, under the pressure of global warming, large amounts of dissolved organic carbon (DOC) due to the thawing of permafrost are delivered into the AO with a long-term increasing river discharge (Peterson et al., 2002; Raymond et al., 2007). As a result, unlike other oceans, the optical properties of the AO are dominated by CDOM as multiple studies have suggested (IOCCG, 2015; Matsuoka et al., 2015, 2007; Matsuoka et al., 2012; Matsuoka et al., 2011). The ternary plot is taken from IOCCG 2015 (see Figure 0.3b,)

to get a basic idea of the proportion of a_{cdom} to total non-water absorption (a_w),. It can be seen that the mean proportion of a_{cdom} at 443 nm reached up 62%, which is about three times that of the other components (i.e., phytoplankton and non-algae particles).

It is known that CDOM exhibits high absorption in the ultraviolet portion of the spectrum, and in the visible. The absorption decays approximately exponentially to the red. When applying global empirical algorithms to the AO, the presence of CDOM at levels higher than the global mean will reduce the reflectance signal at blue wavelengths due to its strong absorption, yielding lower maximum blue-to-green band ratio, which will lead to an overestimation of Chl (Lewis et al., 2016).

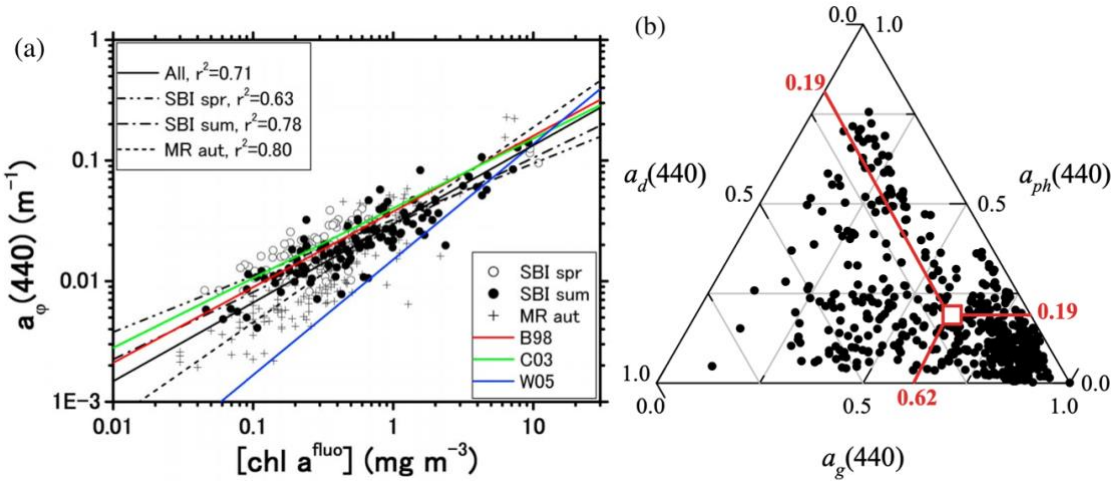

Figure 0.3 (a) Relationship between $a_{ph}(440)$ and Chl^{fluo} showed in Matsuoka et al., 2011. SBI spr and sum refer to data collected through the Western Arctic Shelf Basin Interaction cruise in spring and summer 2004, respectively. MR aut stands for the data obtained in the Chukchi and Beaufort Seas via the Japanese R/V Mirai cruise in autumn 2004. All represents the combination of SBI spr, SBI sum and MR aut. Regression curves from literature are also shown for comparison: B98 (various area of world ocean, Bricaud et al., 1998), C03 (Labrador Sea, Wang and Cota 2003), and W05 (summer in the Beaufort and Chukchi Seas, Wang et al., 2005). (b) Ternary plot depicting the relative partitioning of the non-water absorption coefficient at 440 nm into contributions by phytoplankton (a_{ph}), non-algal particles (a_d), and coloured dissolved organic matter (a_g) for observations from the polar data set. The red square and solid lines represent the mean values for the contribution by each component. (figure from IOCCG, 2015)

Heterogeneous optical properties

The AO is a spatially heterogeneous sea. In other words, the composition of non-water constituents and its bio-optical properties significantly differ from region to region due to various degree of river inputs, nutrient levels, sea ice coverage, shelf widths, and circulation patterns (Lewis et al., 2016; Matsuoka et al., 2013). Such a degree of variability makes it difficult to establish a standard empirical formulation between observed reflectance and Chl that can provide robust predictions with acceptable error limits, at least on the scale of the entire Arctic region.

Turbid coastal waters

As the most river-influenced and landlocked ocean (Vörösmarty et al., 2000), most Arctic coastal regions, especially large river plumes, are experiencing various intricate biogeochemical changes. River discharge, coastal erosion, and permafrost thaw are responsible for a significant supply of organic matter from coastal land. Besides, ice melt and glacial run-off from nearby land also represents a large input in sediment loading. Under the pressure of climate change, these changes are manifested due to Arctic amplification and associated feedback, leading to increased coastal turbidity. Due to the complex optical properties, the estimation of Chl for coastal waters is one of the main problems of OCRS.

Given that coastal phytoplankton blooms are a major ecological event providing a substantial part of the annual primary production and energy transfer supporting the entire marine food web (Field et al., 1998; Winder and Sommer, 2012), the estimation of Chl for turbid coastal waters draw more attention nowadays, and needs to be addressed for better understanding the marine ecosystem and its response to ongoing climate change.

General overview of existing chlorophyll *a* algorithms for the AO

Since the bio-optical relationships between ocean color and Chl in polar regions differ markedly from lower latitude waters, existing operational ocean color algorithms perform poorly when applied to the Arctic waters as many studies have reported (Cota et al., 2004, 2003; Matsuoka et al., 2007; Mitchell, 1992; Mustapha et al., 2012; Naik et al., 2010; Sathyendranath et al., 2001; Stramska et al., 2003; Wang and Cota, 2003). These failures are often explained by the adaptation/acclimation of polar phytoplankton to the extreme environmental characteristics (such as low solar radiation, cold temperature) and different composition of optically-significant constituents.

Empirical algorithms

It was shown more than four decades ago that ocean color, often expressed by the ratio of above-water remote-sensing reflectance (R_{rs}, sr^{-1}) at blue (~440 nm) and green (~550 nm) wavelengths, provides a good index of Chl in oceanic waters (Morel and Prieur, 1977). This empirical way of analyzing ocean color data is the most reliable, robust, and computationally simple approach. It does not require knowledge of the fundamental relationships between R_{rs} and inherent optical properties (IOPs), but requires an adequate data set to develop the empirical coefficients of the relationship. Since they do not necessarily represent all natural variations, the performance of such algorithms is always subject to compatibility between the waters under study and the waters from which data were obtained for algorithm development (see Table 0.4).

Basically, Chl is derived empirically as $Chl = 10^{a_0+a_1R+a_2R^2+a_3R^3+a_4R^4}$, where R is the maximum blue-to-green band ratio, and a_0 to a_4 are empirical coefficients which are derived from in *situ* data sets. Table 0.1 summarizes the global operational and available Arctic empirical algorithms.

Table 0.1 Summary of global operational and available Arctic empirical chlorophyll a algorithms.

Algorithm	Sensor	Area	Reflectance	Blue	Green	a_0	a_1	a_2	a_3	a_4	References
OC3Mv6	MODIS	Global	R_{rs}	443>488	547	0.2424	-2.7423	1.8017	0.0015	-1.2280	(O'Reilly et al., 2000, 1998)
OC4v6	SeaWiFS		R_{rs}	443>490>510	555	0.3272	-2.9940	2.7218	-1.2259	-0.5683	
OC4E	MERIS		R_{rs}	443>490>510	560	0.3255	-2.7677	2.4409	-1.1288	-0.4990	(Antoine and Morel, 1999)
OC4Me	OLCI		R	443>490>510	555	0.4503	-3.2595	3.5227	-3.3594	0.9496	(Antoine, 2010)
OC3V	VIIRS		R_{rs}	443>486	551	0.2228	-2.4683	1.5867	-0.4275	-0.7768	(Wang et al., 2013)
OC4P	SeaWiFS	Beaufort and Chukchi Seas	R_{rs}	443>490>510	555	0.2710	-6.2780	26.29	-60.94	45.31	(Wang and Cota, 2003)
OC4L	SeaWiFS		R_{rs}	443>490>510	555	0.5920	-3.6070	-	-	-	(Cota et al., 2004)
OC3L	SeaWiFS	Chukchi Sea	R_{rs}	443>490	555	0.3364	-3.4388	-	-	-	(Lewis et al., 2016)
SC2S	SeaWiFS	Western coastal waters of Svalbard	R_{rs}	490	555	1.1663	-3.493	-	-	-	(Son and Kim, 2018)
SC3M	MODIS		R_{rs}	443>488	551	1.1699	-3.683	-	-	-	
SC4	SeaWiFS		R_{rs}	443>490>510	555	1.3608	-3.8	-	-	-	
AO.emp	SeaWiFS	Arctic Ocean	R_{rs}	443>490>510	555	0.1746	-2.8293	0.6592	-	-	(Lewis and Arrigo, 2020)
AOReg.emp	SeaWiFS	Arctic interior	R_{rs}	443>490>510	555	-0.3047	-1.5698	-	-	-	
AOReg.emp	SeaWiFS	Arctic outflow/inflow	R_{rs}	443>490>510	555	0.3347	-3.428	1.121	-	-	

The performance of global operational algorithms (including their previous versions) in the AO have significant regional variability (see Table 0.3). Stramska et al. (2003) has reported that the NASA global algorithms (i.e., OC2 and OC4 developed for SeaWiFS (Sea-viewing Wide Field-of-view Sensor) overestimate Chl by a factor of about 2 when Chl<0.2 mg m^{-3} in the north polar region of the Atlantic Ocean. Later, OC4v4 has been documented to overestimate Chl in the low range (<0.6 mg m^{-3}) but underestimate at the other ranges (Cota et al., 2004; Matsuoka et al., 2007) in the Western AO. The latest version, OC4v6, obtained 4.83 and 2.15 MAPDs (mean absolute percentage difference) in the Mackenzie Shelf and Amundsen Gulf and coastal waters of Svalbard, respectively (Mustapha et al., 2012; Son and Kim, 2018). As for MODIS (Moderate-resolution Imaging Spectroradiometer) algorithms, chlor-MODIS leads to two-fold underestimation when Chl>2.5 mg m^{-3} in the north polar region of the Atlantic Ocean (Stramska et al., 2003). OC3M shows an overestimation when Chl<0.6 mg m^{-3} for the western AO (Matsuoka et al., 2007), while in the Chukchi Sea, it tends to lead an underestimation when Chl<0.9 mg m^{-3} but an overestimation at the other values (Lewis et al., 2016). The MAPDs of OC3M-derived Chl are 2.0 for the Beaufort and Chukchi Seas (Chaves et al., 2015), 2.09 for the coastal waters of Svalbard (Son and Kim, 2018), 4.8 for the Mackenzie Shelf and Amundsen Gulf (Mustapha et al., 2012), and 2.36 at a pan-Arctic scale (Lewis and Arrigo, 2020). The MERIS (Medium Resolution Imaging Spectrometer) algorithm OC4E generates a MAPD of 5.2 in the Mackenzie Shelf and Amundsen Gulf (Mustapha et al., 2012).

There are multiple regional Arctic algorithms, such as OC4L (Cota et al., 2004), OC3L (Lewis et al., 2016), OC4P (Wang and Cota, 2003), SC2S/SC3M/SC4 (Son and Kim, 2018), and AOReg.emp (Lewis and Arrigo, 2020). They can yield quite good performance locally (e.g., RMSE=0.13, Matsuoka et al. 2007), but due to the compatibility problem, they exhibit even pronounced regional variability compared to global algorithms when applied to the AO. For instance, OC4L obtained 1.31 MAPD when applied to the Beaufort and Chukchi Seas. However, when used in the Mackenzie Shelf and Amundsen Gulf, the MAPD reached up 5.64, which was larger than that of the global operational algorithms (Mustapha et al., 2012). Therefore, given the large variability in water bio-optical properties within the AO, it seems to be difficult to establish standard empirical formulations to estimate Chl with reasonable uncertainty from observed reflectance at a pan-Arctic scale. However, thanks to the efforts by ocean color researchers, there is an Arctic Ocean empirical algorithm available–AO.emp (Lewis and Arrigo, 2020). Before applying this algorithm routinely to satellite images for the AO, plenty of validations are still needed.

Semi-analytical algorithms

Ocean color semi-analytical algorithms are based on the fundamental relationships of ocean optics. Several assumptions of biogeophysical conditions are incorporated to retrieve certain IOPs, and then in-water constituents from apparent optical properties (AOPs). Currently well-known semi-analytical algorithms are GSM (Garver-Siegel-Maritorena semi-analytical model, Maritorena et al., 2002), FLH (Fluorescence Line Height, Huot et al., 2005), GIOP (Generalized Inherent Optical Property model, Werdell et al., 2013), and QAA (Quasi-Analytical Algorithm, Lee et al., 2002). Note that, only GSM directly targets Chl, while the others

retrieve a_{ph} instead of Chl, but can be converted to Chl based on empirical relationship obtained through in *situ* data sets. Since these algorithms adopt several bio-optical models to describe IOPs, their performance depends on the validity of the assumptions related to the parameterization of the IOP spectral shapes of the model. Thus, model parameters are often optimized for waters under study before application. However, we should keep in mind that these optimized IOPs spectral do not always properly represent all combinations of water constituents.

GSM

The GSM01 model was initially developed by Garver and Siegel (1997) and later updated by Maritorena et al. (2002). And it was designed for use with SeaWiFS data over non-polar Case 1 waters (Morel and Prieur, 1977). The basic idea is to minimize the difference between the modeled and measured below-surface remote-sensing reflectance r_{rs}, using non-linear optimization until a predefined converge threshold is met. In order to simulate the r_{rs} spectrum, GSM01 incorporates 3 bio-optical models to describe the spectral dependency of the absorption coefficient of phytoplankton, a_{ph} (m^{-1}), and colored and detrital material, a_{cdm} (m^{-1}), and of particle backscattering coefficient, b_{bp} (m^{-1}) respectively with 3 empirical parameters (Table 0.2). However， these empirically adjusted parameters optimized for the non-polar case 1 waters may not properly represent the combination of water constituents in the AO. This has been confirmed by Maritorena et al. (2010) that the errors of the GSM01 model are greater in high-latitude regions, as well as the coastal regions. Besides, Mustapha et al. (2012) have also documented that the MAPD of GSM01 reached up to 2.84 in the western AO.

Besides the original GSM01, there are two Arctic-tuned versions: One is GSM01-MOD (Mustapha et al., 2012) which is tuned locally for the western AO. It has been reported to perform quite well in the western AO (MAPD=0.81). Whether it can be applied to other Arctic regions, however, needs to be assessed. The other one is AO.GSM tuned for the entire AO, with a MAPD of 2.23, which is slightly higher than that of AO.emp (Lewis and Arrigo, 2020).

Table 0.2 Summary of available GSM algorithms.

	GSM01	GSM01-MOD	AO.GSM
Region	Non-polar	Southeastern Beaufort Sea	Arctic Ocean
$a_{ph}^{*}(412)$	0.00665	0.00931	0.28503
$a_{ph}^{*}(443)$	0.05582	0.07815	0.21099
$a_{ph}^{*}(490)$	0.02055	0.02877	0.089298
$a_{ph}^{*}(510)$	0.01910	0.02674	0.066926
$a_{ph}^{*}(555)$	0.01015	0.01421	0.029377
$a_{ph}^{*}(670)$	0.01424	0.01994	0.15073
S	0.0206	0.018	0.018996
η	1.0337	1.4	1.3309
Reference	(Maritorena et al., 2002)	(Mustapha et al., 2012)	(Lewis and Arrigo, 2020)

Fluorescence-based algorithms

About 10 years after Lorenzen (1966) introduced the idea to determine Chl from in *vivo* fluorescence, Neville and Gower (1977) brought the idea to airborne remote sensing. After a series of successful applications (Coleman et al., 2000; Cullen et al., 1997; Fell et al., 1999; Fischer and Kronfeld, 1990; Kiefer et al., 1989) and the launch of 3rd generation sensors (e.g., MERIS, MODIS, etc.) which configured with several fluorescence wavebands, algorithms based on Sun-induced Chlorophyll a fluorescence (SICF) became one of the main approaches to retrieve Chl via OCRS.

As a result of photosynthesis and heat dissipation, only a small fraction (usually less than 5%) of absorbed energy is re-emitted as fluorescence (Babin et al., 1996; Huot, 2004). That is to say, in oceanic waters where Chl is generally low, the fluorescence signal is too weak to be detected precisely. Therefore, empirical algorithms based on blue-to-green band ratio are more efficient for this type of water. While in coastal eutrophic waters where Chl is generally high, traditional empirical algorithms perform poorly as the signal in the blue range is likely to drop below the limits of detection due to the high absorption by algae and/or CDOM. Thus, the use of fluorescence-based approach there is crucial to Chl estimates as it has been demonstrated to be more powerful and efficient.

There are several prominent advantages when utilizing fluorescence-based algorithm to retrieve Chl for coastal eutrophic waters: 1) The present fluorescence signal is uniquely attributed by Chl, in other words, it is unlikely to be confused with anything else, such as yellow substance or suspended matters (Xing et al., 2007), and it is one of the most powerful probes of phytoplankton photosynthesis and physiology (Huot, 2004). 2) When blue light signal drops below the detection limits for eutrophic waters with extremely high Chl, unlike other algorithms relying on the signal observed in blue, the fluorescence signal is still powerful to probe. 3) The impact of atmosphere on the red spectrum is smaller than that on the blue-green, thus fluorescence algorithm is less dependent on the accuracy of atmospheric correction.

FLH is the most widely used approach to describe the satellite-observed fluorescence signal. The basic idea is to firstly form the baseline by a linear interpolation of two baseline bands (e.g., 673.75 and 708.75 nm for OLCI), and then subtracted from radiance of fluorescence band (e.g., 681.25 nm for OLCI) to obtain the FLH. Finally, Chl can be derived by comparing the observed FLH with modeled water-leaving fluorescence radiance using the vertical-resolved fluorescence emission model (Huot et al., 2005). However, due to the complex physiological mechanisms, particular spectral characteristics and simplified assumptions adopted, there is still some problems in the application of FLH to derive Chl for coastal eutrophic waters. Firstly, the bio-optical models incorporated in FLH were established for case 1 waters. For instance, the attenuation coefficient for upwelling fluoresced radiance was approximated as the sum of water and phytoplankton absorption, which is not valid for waters with high CDOM. Besides, since FLH contains information of both fluorescence quantum yield (ϕ) and Chl, to obtain information about a given one requires assumptions/measurements of the other one (Huot et al., 2005). Therefore, it is difficult to distinguish Chl from ϕ to obtain accurate estimates. Furthermore,

when Chl increases, the fluorescence peak position tends to shift toward infrared, thus the FLH algorithm would be inappropriate or even useless.

Nonetheless, with the development SICF remote sensing, fluorescence-based algorithm is becoming more and more important for coastal eutrophic waters. Although the performance in the AO remains unknown, fluorescence-based algorithms have a good prospect in the AO, especially for the turbid and productive coastal waters.

GIOP

GIOP is also a spectral-matching approach. The only difference between GIOP and GSM is that GIOP uses a_{ph} rather than Chl to describe phytoplankton spectral absorption. Chaves et al. (2015) has applied GIOP to generate Chl in the Beaufort and Chukchi Seas through the relationship $a_{ph}(443) = 0.055$ Chl, and found that Chl was overestimated by 56%.

QAA

QAA was developed by Lee et al. (2002) to derive inherent optical properties. It is mathematically simple and physically transparent. Basically, it has two consecutive sections in the inversion process. The first section is the derivation of coefficients of total absorption and backscattering coefficients, which are of high accuracy regardless of water types as there is no involvement of spectral models for non-water constituents. In the second section, the derived total absorption coefficient is decomposed into the absorption spectra of three major components, namely absorption of CDOM (a_{cdom}), absorption of non-algal particles (a_{nap}), and a_{ph} using 2 bio-optical models for a_{cdm} and b_{bp} with empirical parameters as well. Zheng et al. (2014) have shown that the absorption-partitioning component of the QAA significantly underestimated a_{ph} and overestimated a_{nap} in the Arctic waters, indicating that these empirical parameters are not suitable for the AO. Note that Chl is not a direct retrieval, but it can be converted from $a_{ph}(670)$ according to their in *situ* relationship (e.g. Bricaud et al. (1995); Bricaud et al. (1998); Bricaud et al. (2004)). The performance of QAA in the AO remains unknown.

Table 0.3 Summary of performance of currently available ocean color algorithms in the AO.

Algorithm	Region	N	Performance
(Stramska et al., 2003)	The north polar region of the Atlantic Ocean	50	OC2, OC4: overestimate by a factor of about 2 at low Chl (<0.2 mg m^{-3}) and underestimate by 20% when Chl>2.5 mg m^{-3}
			Chlor-MODIS: underestimate by nearly a factor of 2 at high Chl> 2.5 mg m^{-3}
(Cota et al., 2004)	The Beaufort, Chukchi, and Labrador Seas	686	OC4v4: overestimate at Chl<0.6 mg m^{-3} and underestimate by nearly a factor of 2 at high Chl (>0.6 mg m^{-3})
(Matsuoka et al., 2007)	Western AO	24	OC4v4: overestimate at Chl<0.6 mg m^{-3} and underestimate at Chl>0.6 mg m^{-3}
			OC3M: overestimate at Chl<0.6 mg m^{-3} and underestimate at Chl>0.6 mg m^{-3}
			OC4L: RMSE=0.13
(Mustapha et al., 2012)	The Mackenzie Shelf and Amundsen Gulf	44	OC4v6: MAPD=4.83
			OC3Mv6: MAPD=4.80
			OC4E: MAPD=5.20
			OC4L: MAPD=5.64
			OC4P: MAPD=5.27
			GSM01: MAPD=2.84
		42	GSM01-MOD: MAPD=0.81
(Chaves et al., 2015)	The Beaufort and Chukchi Seas	33	OC3M: overestimate by a factor of 2, RMSE=0.295
		32	GIOP: overestimate by 56%, RMSE=0.245
(Lewis et al., 2016)	The Beaufort and Chukchi Seas	62	OC3M: MAPD=1.97, RMSE=4.91
			OC4L: MAPD=1.31, RMSE=4.42
			OC4P: MAPD=7.18, RMSE=803
			OC3L: MAPD=0.82, RMSE=2.9
(Son and Kim, 2018)	Western coastal waters of Svalbard	34	OC2: MAPD=2.42
			OC3Mv6: MAPD=2.09
			OC4v6: MAPD=2.15
		33	OC4L: MAPD=2.62
		31	SC2S: MAPD=0.51
			SC3M: MAPD=0.51
			SC4: MAPD=0.49
(Lewis and Arrigo, 2020)	Arctic Ocean	501	OC3M: MAPD=2.36
			OC4L: MAPD=2.35
			OC3L: MAPD=2.17
			AO.emp: MAPD=2.16
			AOReg.emp: MAPD=1.97
		418	GSM01: MAPD=2.34
		393	AO.GSM: MAPD=2.23

Neural Network algorithms

Since the direct use of a purely Radiative Transfer Equation (RTE) approach is hindered by complexity and lack of underlying physical models, empirical data driven models are still a good choice if the underlying

characteristics of the water properties can be assimilated into the algorithms. One possible solution is the application of artificial neural network algorithms which work for both open ocean and complex coastal waters. NNs are very generic, accurate, and convenient mathematical models that emulate complicated nonlinear input/output relationships through statistical learning algorithms. They approximate the transfer functions between a large number of possibly-interconnected inputs and multiple outputs, even for nonlinear and not well known relationships.

For ocean color applications, the NN approaches are complementary to empirical and semi-analytical approaches as they are capable of inverting directional water-leaving radiance reflectance directly into absorption and scattering coefficients or concentrations of different constituents present in waters using a highly non-linear system. But they require a large data set to be trained to determine a set of weights so that the given input produced the desired output. Therefore, they are dependent of the simulated data set and the choice of architecture inside. In the end, a forward optical model must be used, with assumptions similar to those made in semi-analytical algorithms. Besides, the training process is usually computationally expensive and time-consuming. After training, computation is however very cheap and fast, making NN-based algorithms, such as C2RCC (Case 2 Regional CoastColor, Brockmann et al. (2016)), capable for operational and near-real time satellite observations. ONNS (OLCI Neural Network Swarm, Hieronymi et al. (2017)) is a novel one coupled with several NNs and incorporate water type classification.

C2RCC Processor

The MERIS Case-2 water algorithm, originally developed by Doerffer and Schiller (2007), uses a large database of radiative transfer simulations inverted by neural networks as basic technology. After amended by a set of additional NNs performing specific tasks to cover extreme ranges of scattering and absorption, it has been renamed as C2RCC and is applicable to all past and current ocean color sensors. Generally, the C2RCC processor relies on a large database of simulated water-leaving reflectances, and related TOA (top-of-atmosphere) radiances. NNs are trained in order to perform the inversion of spectrum for the atmospheric correction, i.e. the determination of the water-leaving radiance from the TOA radiances, the retrieval of IOPs, as well as bio-optical components in the water column. It is one of the very few algorithms actually developed and validated for Case 2 waters, and it is used to generate the Case 2 water products in Sentinel 3 OLCI (Ocean and Land Colour Instrument) standard ESA (European Space Agency) products.

ONNS

ONNS is a novel in-water algorithm for the retrieval of ocean color products from Sentinel-3 OLCI images using a series of classification-based NNs (Hieronymi et al., 2017). The distinctive feature of this algorithm is the wide range of applicability in terms of optical water properties ranging from oligotrophic ocean waters to extremely turbid (scattering) or dark (absorbing) waters. However, since it is an in-water processor. Its performance relies strongly on the accuracy of atmospheric correction.

So far, the existing state-of-the-art NNs have not been tested for Arctic waters. But once appropriately trained, NN is believed to make a difference in the current situation of OCRS in the Arctic.

Table 0.4 Summary of the advantages and disadvantages of 3 types of algorithms.

Algorithm type	Advantages	Disadvantages
Empirical	Simple Robust Computationally simple	Dependent on simulated data set Subject to compatibility
Semi-analytical	Direct Multiple retrievals Independent of simulated data set Non-linear	Require fundamental relationships of ocean optics Convergence problem CPU intensive Require initial guess
Neural network	Plenty of retrievals Always converges Non-linear	Dependent on simulated data set Slow training CPU intensive Choice of architecture

Objectives

It is known that the operational ocean color algorithms perform poorly in the AO due to its complex bio-optical properties that significantly distinguish it from other oceans. Hence, the aim of this thesis (composed of three research papers, i.e., chapter 1-3) is to better detect phytoplankton in the Arctic Ocean using OCRS, especially for CDOM-rich turbid coastal waters. This thesis is based on the premise that, adding longer wavelengths that are less affected by CDOM to semi-analytical algorithms is important to better describe the roles of optical-significant components, thus leading to better results.

The main objective of the first chapter is to thoroughly evaluate currently available chlorophyll a algorithms from the perspective of the impacts by CDM. This is motivated by the fact that one of the main problems of OCRS in the AO is the interference of CDM with the phytoplankton signal in the visible spectrum. We want to figure out how and to what extent that CDM will bias the estimation of Chl, especially in and around large river plumes with high level of CDM. In addition, since Chl is a key variable used for PP estimation, there is a complementary objective in this chapter, which is to assess the error propagation from algorithm-derived Chl to PP estimates.

In the second chapter, we tune GSM for the AO by adding 620 nm waveband. Lewis et al., 2020 has tuned GSM with original 6 wavebands for the AO, and found that the MAE (mean absolute error) of their tuned algorithm AO.GSM improved by 11% when compared with the original version (GSM01). We want to know how much further improvement we can make by tuning the GSM through the addition of 620 nm. The reasons for doing so are 1) AO.GSM fails too often for waters with high CDM, thus is not robust when applied to coastal waters; 2) signal observed at 620 nm is believed to be useful to better distinguishing absorption by phytoplankton and CDM, and absorption from scattering, which would in return lead to more accurate retrievals for the CDOM-rich coastal waters; 3) signals at 620 nm can be detected by OLCI (Ocean and Land Colour Instrument), therefore, the newly tuned GSM model is able to be widely used for satellite applications.

The third chapter is to propose a novel full-spectral algorithm by coupling GSM and fluorescence emission model. We get an impression that a single algorithm is not likely to work out for the heterogenous AO, at least for extremely turbid coastal waters. For instance, in extremely dark/absorbing waters, the blue signal would drop below the detection limits, then algorithms rely on blue signal (e.g., empirical algorithms, GSM) become useless. Although the fluorescence signal in the red spectrum is powerful to probe, FLH is still not applicable as the background signal can not simply assumed spectrally flat. The coupling of GSM with fluorescence-based algorithm might be a solution as they complement each other. That it, for oligotrophic waters where fluorescence algorithm is weak, we should make full use of GSM, while for eutrophic waters, although GSM is not good at, but it is very useful to describe the background signal to make the fluorescence algorithm work.

Chapitre 1 Performance of algorithms for retrieving chlorophyll-a concentrations in the Arctic Ocean: impact on primary production estimates

Juan Li, Atsushi Matsuoka, Xiaoping Pang, Marcel Babin

1.1 Résumé

La concentration en chlorophylle a (Chl) est une variable clé pour estimer la production primaire (PP) à l'aide de la télédétection de la couleur de l'océan (OCRS). Une estimation précise de la Chl est essentielle pour mieux comprendre les tendances spatio-temporelles de la PP au cours des dernières décennies en raison du changement climatique. Cependant, de nombreuses études ont rapporté que les algorithmes de chlorophylle a actuellement disponibles sont peu performants dans l'océan Arctique (AO), ce qui s'explique principalement par l'interférence des matériaux colorés et détritiques (CDM) avec le signal du phytoplancton dans le spectre visible. Afin de déterminer comment et dans quelle mesure le CDM pourrait biaiser l'estimation de la Chl, nous avons évalué les performances des algorithmes de couleur de l'océan actuellement disponibles: trois algorithmes empiriques globaux - OC4v6 (SeaWiFS), OC3Mv6 (MODIS), OC3V (VIIRS), deux algorithmes régionaux - OC4L et OC4P, un algorithme arctique AO.emp et deux algorithmes semi-analytiques - GSM01, AO.GSM du point de vue de l'impact du CDM. Il a été constaté que plus le niveau de MDP dans la colonne d'eau était élevé, plus il biaisait les estimations de la Chl. Pour les eaux avec un niveau élevé de CDM, c'est l'AO.GSM qui était le moins biaisé avec une MAE (erreur absolue moyenne) inférieure à 2,02. Cependant, l'AO.GSM présentait 16,2 % d'échecs pour ces types d'eau, ainsi, un algorithme de chlorophylle a capable de discriminer et de quantifier les rôles des constituants non-phytoplanctoniques et donc de générer des estimations de Chl aussi raisonnables que possible est toujours attendu dans les recherches futures. En outre, l'analyse de sensibilité de la Chl sur l'estimation de la PP en utilisant le modèle de production primaire de l'Arctique résolu spectralement et verticalement suggère que les erreurs de la Chl se propagent principalement proportionnellement à la PP, et ont été amplifiées de moins de 7%.

1.2 Abstract

Chlorophyll a concentration (Chl) is a key variable to estimate primary production (PP) through ocean color remote sensing (OCRS). Accurate Chl estimate is crucial for better understanding of spatio-temporal trends of PP over recent decades as a consequence of climate change. However, many studies have reported that currently available chlorophyll a algorithms perform poorly in the Arctic Ocean (AO), which is mainly explained by the interference of colored and detrital material (CDM) with phytoplankton signal in the visible spectrum. To determine how and to what extent that CDM would bias the estimation of Chl, we evaluated the performances of current available ocean color algorithms: three global empirical algorithms - OC4v6 (SeaWiFS), OC3Mv6 (MODIS), OC3V (VIIRS), two regional algorithms - OC4L and OC4P, one Arctic algorithm AO.emp and two semi-analytical algorithms - GSM01, AO.GSM from a perspective of the impact of CDM. It was found that the higher the level of CDM in the water column, the larger it would bias Chl estimates. For waters with high CDM, it was AO.GSM that was least biased with MAE (mean absolute error) less than 2.02. However, AO.GSM had 16.2% failures for such water types, thus, chlorophyll a algorithm that is capable to discriminate and quantify the roles of non-phytoplankton constituents and hence generate as much as reasonable Chl estimates is still expected in future researches. In addition, sensitivity analysis of Chl on PP estimation using the Arctic spectrally- and vertically-resolved primary production model suggests that errors in Chl mostly propagate proportionally to PP, and were amplified less than 7%.

1.3 Introduction

The Arctic Ocean (AO) is one of the most sensitive areas to ongoing global warming on Earth. As sea ice extent in the AO continues to decrease, light penetration into the ocean increases which concomitantly increases the growth of phytoplankton when sufficient amounts of nutrients are available. As a consequence, primary production (PP) of the AO is likely to increase as many ocean color remote sensing (OCRS) studies have suggested (Ardyna and Arrigo, 2020; Arrigo et al., 2008; Bélanger et al., 2013a; Pabi et al., 2008). Chlorophyll *a* concentration (Chl), a proxy of phytoplankton biomass, is a key variable used for PP estimate through OCRS. Accurate Chl estimate is crucial for better understanding of spatio-temporal trends of PP over recent decades as a consequence of climate change.

Due the unique bio-optical properties of the AO, operational chlorophyll *a* algorithms perform poorly in the AO as multiple studies have suggested. Stramska et al. (2003) has reported that the NASA global algorithms (i.e., OC2 and OC4 developed for SeaWiFS (Sea-viewing Wide Field-of-view Sensor) overestimate Chl by a factor of about 2 when Chl<0.2 mg m^{-3} in the north polar region of the Atlantic Ocean. Later, OC4v4 has been documented to overestimate Chl in the low range (<0.6 mg m-3) but underestimate at the other ranges (Cota et al., 2004; Matsuoka et al., 2007) in the Western AO. The latest version, OC4v6, obtained 4.83 and 2.15 MAPDs (mean absolute percentage difference) in the Mackenzie Shelf and Amundsen Gulf and coastal waters of Svalbard, respectively (Mustapha et al., 2012; Son and Kim, 2018). As for MODIS (Moderate-resolution Imaging Spectroradiometer) algorithms, chlor-MODIS leads to two-fold underestimation when Chl>2.5 mg m^{-3} in the north polar region of the Atlantic Ocean (Stramska et al., 2003). OC3M shows an overestimation when Chl<0.6 mg m^{-3} for the western AO (Matsuoka et al., 2007), while in the Chukchi Sea, it tends to lead an underestimation when Chl<0.9 mg m^{-3} but an overestimation at the other values (Lewis et al., 2016). The MAPDs of OC3M-derived Chl are 2.0 for the Beaufort and Chukchi Seas (Chaves et al., 2015), 2.09 for the coastal waters of Svalbard (Son and Kim, 2018), 4.8 for the Mackenzie Shelf and Amundsen Gulf (Mustapha et al., 2012), and 2.36 at a pan-Arctic scale (Lewis and Arrigo, 2020). The MERIS (Medium Resolution Imaging Spectrometer) algorithm OC4E generates a MAPD of 5.2 in the Mackenzie Shelf and Amundsen Gulf (Mustapha et al., 2012).

As for Arctic empirical algorithms, there is one Arctic algorithm AO.emp (Lewis and Arrigo, 2020) and several regional algorithms: OC4P (Wang and Cota, 2003), OC4L (Wang et al., 2005) and OC3L (Lewis et al., 2016). Usually, OC4P performs worse than OC4L as many studies have reported (Lewis et al., 2016; Matsuoka et al., 2007; Mustapha et al., 2012). OC4L outperforms global empirical global algorithms in the western Arctic Ocean (Lewis et al., 2016; Matsuoka et al., 2007), but the contrary is showed for the Mackenzie Shelf and Amundsen Gulf (Mustapha et al., 2012). While at a pan-Arctic scale, AO.emp outperforms OC3L and OC4L, but the MAPD is still as high as 2.16 (Lewis and Arrigo, 2020).

In addition to these empirical ocean color algorithms, semi-analytical algorithms, such as GSM01 (non-polar case 1 water, Maritorena et al. (2002)) and AO.GSM (tuned version for the AO, Lewis and Arrigo (2020)) do not work well in the AO either. It has been documented that GSM01 underestimates Chl by ~50% for the

Beaufort and Chukchi Seas (Wang and Cota, 2003), but overestimates Chl by a factor of 2 in Mackenzie Shelf and Amundsen Gulf (Mustapha et al., 2012). Although AO.GSM has better performance than GSM01 in the AO, but the MAPD reaches up to 2.23 which is larger than the empirical algorithm AO.emp.

These poor performances are mainly due to the interference with phytoplankton signal in the visible spectrum by high level of CDM (colored and detrital material) in the water column as multiple studies have suggested (Lewis et al., 2016; Lewis and Arrigo, 2020; Matsuoka et al., 2012; Matsuoka et al., 2011; Matsuoka et al., 2007). However, how and to what extent it will bias Chl estimates remain unknown. In addition, Chl as a key variable used for PP estimates, the impact of algorithm-derived Chl on PP estimates needs to be investigated as well.

To address these issues, we first built an in *situ* high-quality bio-optical data set at a Pan-Arctic scale. Based on which, the objectives of this study were to 1) evaluate the performances of current available ocean color algorithms from a perspective of the impacts from CDM; 2) determine how errors of algorithm-derived Chl would propagate to PP estimates using an Arctic spectrally- and vertically-resolved primary production model.

1.4 Data

1.4.1 In *situ* data

The Arctic data set used for algorithm evaluation was composed of the following five cruises: the France-Canada-USA joint Arctic campaign MALINA (http://www.obs-vlfr.fr/proof/php/malina/), ICESCAPE (Impacts of Climate on Ecosystems and Chemistry of the Arctic Pacific Environment, https://seabass.gsfc.nasa.gov/) 2010 and 2011, Tara Oceans Polar Circle expedition (https://oceans.Taraexpeditions.org/), and GREEN EDGE (http://www.obs-vlfr.fr/proof/php/GREENEDGE/). Sampling of MALINA and GREEN EDGE (ship operation) was conducted aboard the Canadian icebreaker *CCGS Amundsen*. The two ICESCAPEs were aboard the US icebreaker *USCGC Healy*. The Tara expedition was conducted using the French schooner, *Tara*.

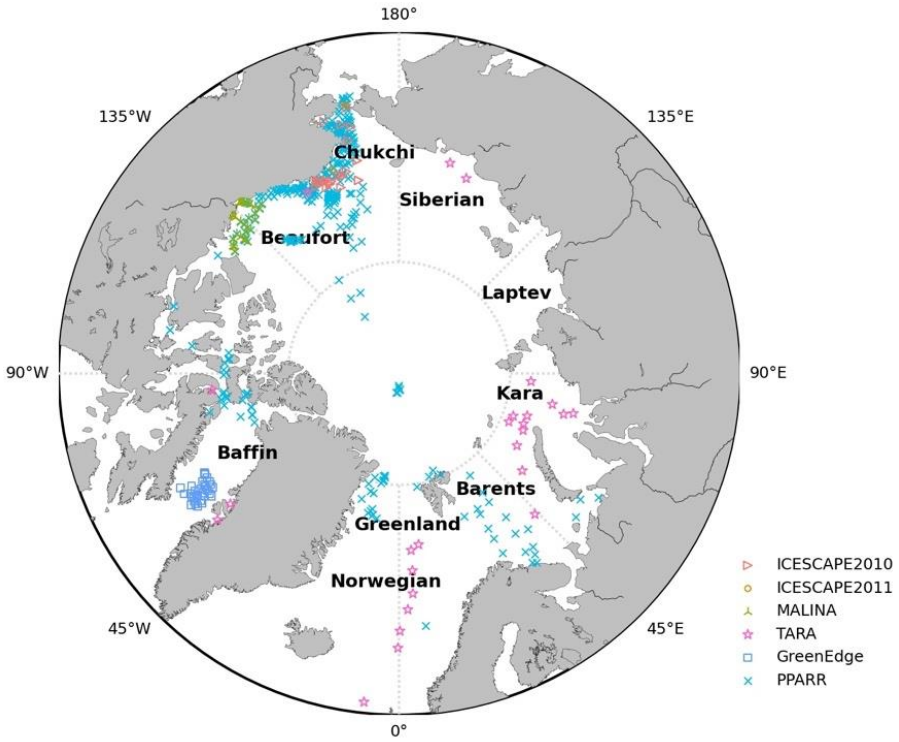

Figure 1.1 Map of the Arctic Ocean showing the locations of stations from various datasets.

Table 1.1 Summary of in *situ* datasets.

Data	Station	Year	Month	Region	Source
MALINA	37	2009	July-August	Southern Beaufort Sea	SeaBASS
ICESCAPE2010	34	2010	June-July	Chukchi and Beaufort Sea	SeaBASS
ICESCAPE2011	18	2011	June-July	Chukchi and Beaufort Sea	SeaBASS
TARA	27	2013	May-November	Polar circle	SeaBASS
GREEN EDGE	34	2016	June-July	Baffin Bay	Individual
PPARR	973	1959-2011	August	Arctic Ocean	NOAA NCEI

Among the measured variables, remote-sensing reflectance $R_{rs}(\lambda)$ and Chl are the two most important variables. In the present study, all $R_{rs}(\lambda)$ were determined with the same instrument, the Compact-Optical Profiling System (C-OPS, Biospherical Instrument Inc.). Specific information about the C-OPS is provided by Hooker et al. (2013). Briefly, the C-OPS consists of two 7 cm diameter radiometers: one measures in-water upwelling radiance $L_u(\lambda, z)$ and the other measures in-water downward irradiance $E_d(\lambda, z)$, pressure/depth, and dual axes tilts. The above-water downward solar irradiance ($E_s(\lambda)$) was also measured to account for changes in the incident light field during in-water profiles. All radiometers are equipped with 19 state-of-the-art microradiometers spanning the 320–780 nm spectral range, and only data with tilt angle less than 5° were used. Subsurface $L_u^-(\lambda)$ and $E_d^-(\lambda)$ were derived by loess extrapolating $L_u(\lambda, z)$ and $E_d(\lambda)$ through progressively optimized depth interval within the first optical depth. Finally, $R_{rs}(\lambda)$ was calculated as: $R_{rs}(\lambda) = 0.52L_u^-(\lambda)/E_d^-(\lambda)$. Details of the process protocols are described in Antoine et al. (2013). Only common wavebands (412,443,490,510,555,670 nm) of these 5 cruises were used in this study.

Chl was determined by High-Performance Liquid Chromatography (HPLC). Generally, 25 mm GF/F filters were used to collect phytoplankton from seawater samples. Filters were extracted in 100% methanol, disrupted by sonication and clarified by filtration (GF/F Whatman) before being analyzed by HPLC later in the laboratory to obtain separated pigments. HPLC measurements for ICESCAPEs samples followed the protocols described in Van Heukelem and Thomas (2001), while for MALINA, Tara-Arctic, and GREEN EDGE samples, we applied a protocol modified from Ras et al. (2008) to increase sensitivity in the analysis of ultra-oligotrophic waters. Finally, total chlorophyll-a pigment concentration was defined as the sum of mono and divinyl chlorophyll a concentrations, chlorophyllide a and the allomeric and epimeric forms of chlorophyll a (Hooker and Zibordi, 2005; Reynolds et al., 2016).

Absorption coefficient of colored detrital material ($a_{cdm}(\lambda)$) is the sum of absorption coefficient of colored dissolved organic matter ($a_{cdom}(\lambda)$) and non-algal particles ($a_{nap}(\lambda)$). $a_{cdom}(\lambda)$ was measured using a liquid core waveguide system, UltraPath (WPIInc.,http://www.wpi-europe.com/products/spectroscopy/ultrapath.htm) following (Bricaud et al., 2010; Matsuoka et al., 2012). $a_{nap}(\lambda)$ was determined following the methodology described in (Bricaud et al., 2010; Kishino et al., 1985; Stramski et al., 2015). Note that, in this study, $a_{cdm}(443)$ was only used for classification purpose.

Data collected through PPARR in this study was used for comparison purpose with the satellite climatology products only. Briefly, at each station, surface Chl was measured via fluorometric method between 0 and 5 m depth, while PP was measured at various depths using ^{13}C- or ^{14}C-labeled compounds. Details were described at https://www.ncei.noaa.gov/access/metadata/landing-page/bin/iso?id=gov.noaa.nodc:0161176. Numbers of stations, sampling dates, sampling regions and data source from all expeditions are summarized in Table 1.1, the locations of sampling stations are shown in Figure 1.1.

1.4.2 Satellite products

OC-CCI (Ocean Color Climate Change Initiative, https://esa-oceancolour-cci.org/) L3b daily chlorophyll a products and reflectance products, MODIS atmospheric products (MYD08, https://ladsweb.modaps.eosdis.nasa.gov) on August from 2003 to 2018 were downloaded to generate climatology Chl and PP products for the AO. Note that the OC-CCI chlorophyll a products are merged products based on SeaWiFS, MERIS, aqua-MODIS and VIIRS (Visible Infrared Imaging Radiometer Suite) data to get as many as pixels, Chl values are calculated using blending algorithms based on the water types as documented in ATBD-OCAB (Algorithm Theoretical Baseline Document (Ocean Color Algorithm Blending)) (Jackson and Grant, 2016), which is substantially an empirical approach.

1.5 Methods

1.5.1 Descriptions of existing operational ocean color algorithms

In this study, global empirical algorithms for SeaWiFS (OC4v6), MODIS (OC3Mv6), VIIRS (OC3V), two regional empirical algorithms - OC4L and OC4P, one AO empirical algorithm AO.emp, and two semi-analytical algorithm GSM01 and GSM.AO were evaluated.

Empirical algorithms

All empirical algorithms use polynomial functions to fit the relationship between Chl and the maximum blue-to-green ratio of remote sensing reflectance:

$$\mathrm{Chl} = 10^{a_0+a_1R+a_2R^2+a_3R^3+a_4R^4} \quad (1)$$

Where R is the base 10 logarithm of the maximum blue-to-green band ratio of R_{rs} and a_i are empirically-derived coefficients listed in Table 1.2.

Note that wavelengths used for the blue and green bands varies slightly among sensors (see Table 1.2) and they were designed for different water bodies. OC3Mv6, OC4v6, and OC3V were obtained using a global in *situ* data set mainly from Case 1 and non-polar waters (O'Reilly et al., 2000; O'Reilly et al., 1998). OC4P and OC4L were tuned using in *situ* measurements made in the Canadian Arctic waters (in the vicinity of Resolute Bay and in Labrador sea, Wang and Cota (2003)) and the western Arctic (Chukchi and Beaufort Seas, Cota et al. (2004)), respectively. AO.emp was optimized using a large data set compiled at a pan-Arctic scale (K. Lewis et al., 2020; Lewis and Arrigo, 2020).

Table 1.2 Band configurations and coefficients of the empirical chlorophyll *a* algorithms evaluated.

Algorithms	Blue	Green	a_0	a_1	a_2	a_3	a_4
OC3Mv6	443>488	547	0.2424	-2.7423	1.8017	0.0015	-1.2280
OC3V	443>486	551	0.2228	-2.4683	1.5867	-0.4275	-0.7768
OC4v6	443>490>510	555	0.3272	-2.9940	2.7218	-1.2259	-0.5683
OC4P	443>490>510	555	0.2710	-6.2780	26.29	-60.94	45.31
OC4L	443>490>510	555	0.5920	-3.6070	-	-	-
AO.emp	443>490>510	555	0.1746	-2.8293	0.6592	-	-

Semi-analytical algorithm - GSM

The GSM semi-analytical ocean color model was initially developed by Garver and Siegel (1997) and later updated by Maritorena et al. (2002). It was initially designed for SeaWiFS over non-polar Case 1 waters. The basic principle is to minimize the difference between the measured and modeled below-surface remote-sensing reflectance r_{rs} using non-linear optimization until a predefined convergence threshold is met. A detailed description of the GSM01 model and values of model parameters can be found in Maritorena et al. (2002).

The GSM model can be easily tuned by reparameterization model parameters using bio-optical data. Lewis and Arrigo (2020) optimized the model parameters using a genetic optimization method for the AO using the Arctic dataset described in Lewis et al. (2020), and the tuned model was named AO.GSM. They found that the

optimized parameters represent the unique bio-optical characteristics of the AO more accurately. Details of the genetic optimization procedure and parameter values were described in Lewis and Arrigo (2020).

1.5.2 Evaluation criteria

The performance of each ocean color algorithm was assessed following the metrics described in Seegers et al. (2018). First is the number of effective retrievals. For example, GSM01 might generate negative Chl values due to the optimization regime. Next two metrics are bias and mean absolute error (MAE) which have been proven to be robust and straightforward quantities for evaluating ocean color algorithms with non-Gaussian distributions and outliers (Seegers et al., 2018).

$$\text{bias} = 10^{\text{mean}(log10(X^M)-log10(X^E))} \quad (2)$$

$$\text{MAE} = 10^{\text{mean}|log10(X^M)-log10(X^E)|} \quad (3)$$

Bias illustrates the systematic direction of error, as either underestimation or overestimation on average. A bias close to 1 means minimum bias, while a value lower than 1 reflect underestimation. A bias of 0.8 for instance reflects 20% underestimation on average. The same reasoning holds for overestimations. MAE indicates the random error. It is always larger than 1. For instance, a MAE of 1.2 means average 20% relative error in retrievals compared to measured values.

The fourth metric is wins, which is obtained through pair-wise comparison. That is, for each pair of estimated and measured variable, residuals (defined as estimated value minus measured value) for model A and model B are calculated, the model with lower residual is the winner, model failures are directly designated as loser. Wins is the percentage of winners to the total number of pairs, which can be used to tell which model performs better and help to decide which model should be used in applications.

Besides, slope and coefficient of determination (r^2) for log-transformed variable were also produced via type II reduced major axis (RMA) regression (Legendre, 1998) as complementary metrics.

1.5.3 Classification

Based on measured median value of Chl (0.35 mg m^{-3}), we split the in *situ* dataset by half. For the part with Chl $\leq$ 0.35 mg m^{-3}, samples with $a_{cdm}(443) \leq 0.067$ m^{-1} were classified as chl.acdm, the others with $a_{cdm}(443) >$ 0.067 m^{-1} were regarded as chl.ACDM. The same procedure was applied to the other part of the dataset with Chl > 0.35 mg m^{-3}. Therefore, we got CHL.acdm and CHL.ACDM. The illustration of the classification approach is summarized in Table 1.3.

Table 1.3 Classification criteria.

Water type	Threshold	Number
chl.acdm	Chl $\leq$ 0.35 mg m^{-3}, $a_{cdm}(443) \leq 0.067$ m^{-1}	48
CHL.acdm	Chl > 0.35 mg m^{-3}, $a_{cdm}(443) \leq 0.067$ m^{-1}	26
chl.ACDM	Chl $\leq$ 0.35 mg m^{-3}, $a_{cdm}(443) > 0.067$ m^{-1}	26
CHL.ACDM	Chl > 0.35 mg m^{-3}, $a_{cdm}(443) > 0.067$ m^{-1}	48

1.5.4 Primary production model

The spectrally-resolved primary production model for the Arctic waters developed by Bélanger et al. (2013a) was adopted in the present study. One advantage of this model relative to others (Arrigo et al., 2008; Pabi et al., 2008; Perrette et al., 2010) is the consideration of the propagation of spectral light in the atmosphere and the ocean using methods appropriate for both Case 1 and Case 2 waters. In recent years, this model has been further optimized to account for subsurface chlorophyll a maxima often observed in the AO. This was achieved using the statistical relationships between Chl at surface and at depth published by Ardyna et al. (2013). Besides, instead of using R_{rs} and Chl data from the GlobColour dataset as in Bélanger et al. (2013a), in the present study, $R_{rs}(\lambda)$ merged products based on SeaWiFS, MERIS, aqua-MODIS and VIIRS data from OC-CCI were used, and Chl products were derived through the merged $R_{rs}(\lambda)$ products using the chlorophyll a algorithms mentioned above.

The structure of this spectrally- and vertically-resolved Arctic primary production model is illustrated in Figure 1.2. Basically, the daily rates of the carbon fixation PP in unit of mgC m^{-2} d^{-1} by phytoplankton cells is estimated using the classical photosynthesis versus light model (Platt and Gallegos, 1980):

$$\mathrm{PP} = \mathrm{P_B^{max}} \int_{t=0}^{24h} \int_{z_{0.1\%}}^{z_{100\%}} \mathrm{Chl}\,(z)\left(1 - e^{-\frac{\mathrm{PUR}(z,t)}{E_k(\mathrm{PUR})}}\right)\mathrm{d}z\mathrm{d}t \quad (4)$$

Where P_B^{max} (mgC $mgChl^{-1}$ h^{-1}) is the light-saturated chlorophyll-normalized carbon fixation rate, which is assumed constant at 2.0 mgC $mgChl^{-1}$ h^{-1} (see Bélanger et al., 2013a and references therein). $\mathrm{Chl}\,(z)$ is chlorophyll a concentration at a given depth z, which can be propagated from surface values following Ardyna et al. (2013). $\mathrm{PUR}(z,t)$ is the photosynthetically usable radiation expressed in µmol photons m^{-2} s^{-1} (Morel, 1978), which can be estimated using input atmospheric data and satellite-observed $R_{rs}(\lambda)$, and the spectral model of light propagation through the atmosphere and ocean has been described in Bélanger et al. (2013a). $E_k(z)$ (µmol photons m^{-2} s^{-1}) is the saturation irradiance, parameterized here as a function of $\mathrm{PUR}\,(z,t)$ (Bélanger et al., 2013a). In this study, in order to perform sensitivity analysis to assess the impact of Chl on PP estimates, all the other inputs and parameters except Chl were kept unchanged.

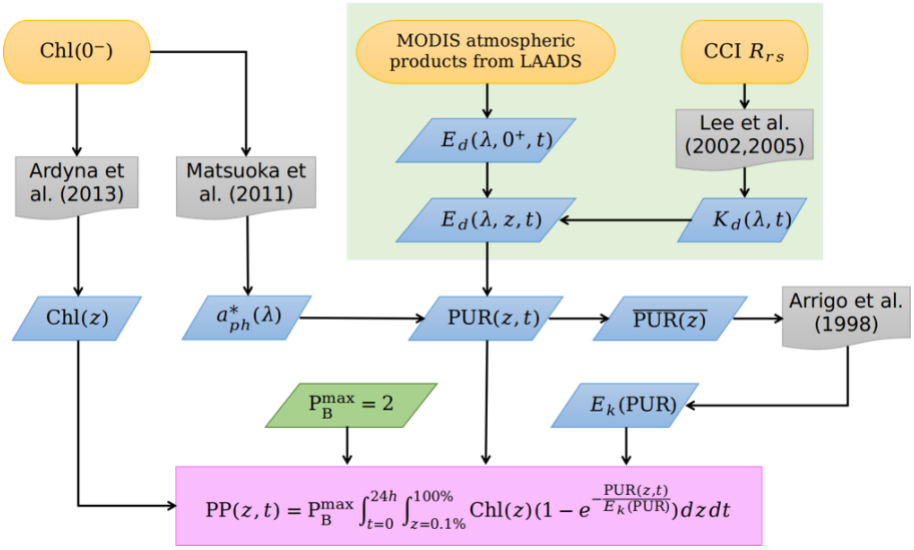

Figure 1.2 Structure of the spectrally- and vertically-resolved Arctic primary production model. Yellow, gray, blue, green and red frames refer to model inputs, methods described in literature, intermediate variables, constant values and photosynthesis model, respectively (by courtesy of Marcel Babin and Simon Bélanger).

1.5.5 Climatology products

Chl climatology product on August was obtained by averaging all the CCI daily Chl products collected in August from 2003 to 2018. While for PP climatology product in August, firstly, each daily Chl product acquired in August was passed into the Arctic primary production model (described in section 1.5.4) along with corresponding daily reflectance product and MODIS atmospheric product to derive daily PP product. Then all daily PP products were averaged to obtain the climatology PP product.

1.6 Results

1.6.1 Overview of product performances

Given the lack of in *situ* and satellite matchups, to get a general insight of the accuracy of Chl product at a pan-Arctic scale, climatology Chl product in August (Figure 1.3(a)) was compared with the in *situ* Chl measurements taken in August from PPARR by a kernel density plot (Figure 1.3(b)). It can be seen that the Chl product shows a general trend of overestimation (median Chl = 0.66 mg m^{-3}) when compared with in *situ* values (median Chl = 0.40 mg m^{-3}), mainly in the section where Chl < 1.2 mg m^{-3} (accounts for nearly 2/3 of all pixels). Besides, there is a small percentage of noticeable overestimation in the range from 4.0 to 11.0 mg m^{-3}. Combining Chl distribution showed in Figure 1.3(a), this part of overestimations happened along the eastern coastal areas where there are large amounts of CDM resulting from river discharge.

The corresponding climatology PP product is shown in Figure 1.3(c), and the density curve compared with PP measurements from PPARR (same pairs of Chl measurements showed in Figure 1.3(b)) is illustrated in Figure 1.3(d). We can see that PP estimates were also overestimated overall (median PP = 0.33 gC $m^{-2}d^{-1}$) when compared with in *situ* values (median PP = 0.22 gC $m^{-2}d^{-1}$). There is only one crest located at 0.33 gC $m^{-2}d^{-1}$. 1/3 of all the PP estimates in the lower range (from 0.007 to 0.2 gC $m^{-2}d^{-1}$) were overestimated, which was likely due to the overestimation of input Chl. In the higher range (PP > 0.6 gC $m^{-2}d^{-1}$), another 1/3 PP estimates were however underestimated. The overestimation on the left side and underestimation on the right side steepened the crest, making the density at the crest is nearly 8 times that of the in *situ* one. It is noticeable that the overestimation of Chl estimates along the eastern coastal areas did not lead to overestimation in PP estimates. It is likely that the high proportion of CDM in the water column highly absorbs the sunlight, which in return resulting in less PUR for the absorption by phytoplankton (Hessen et al., 2010).

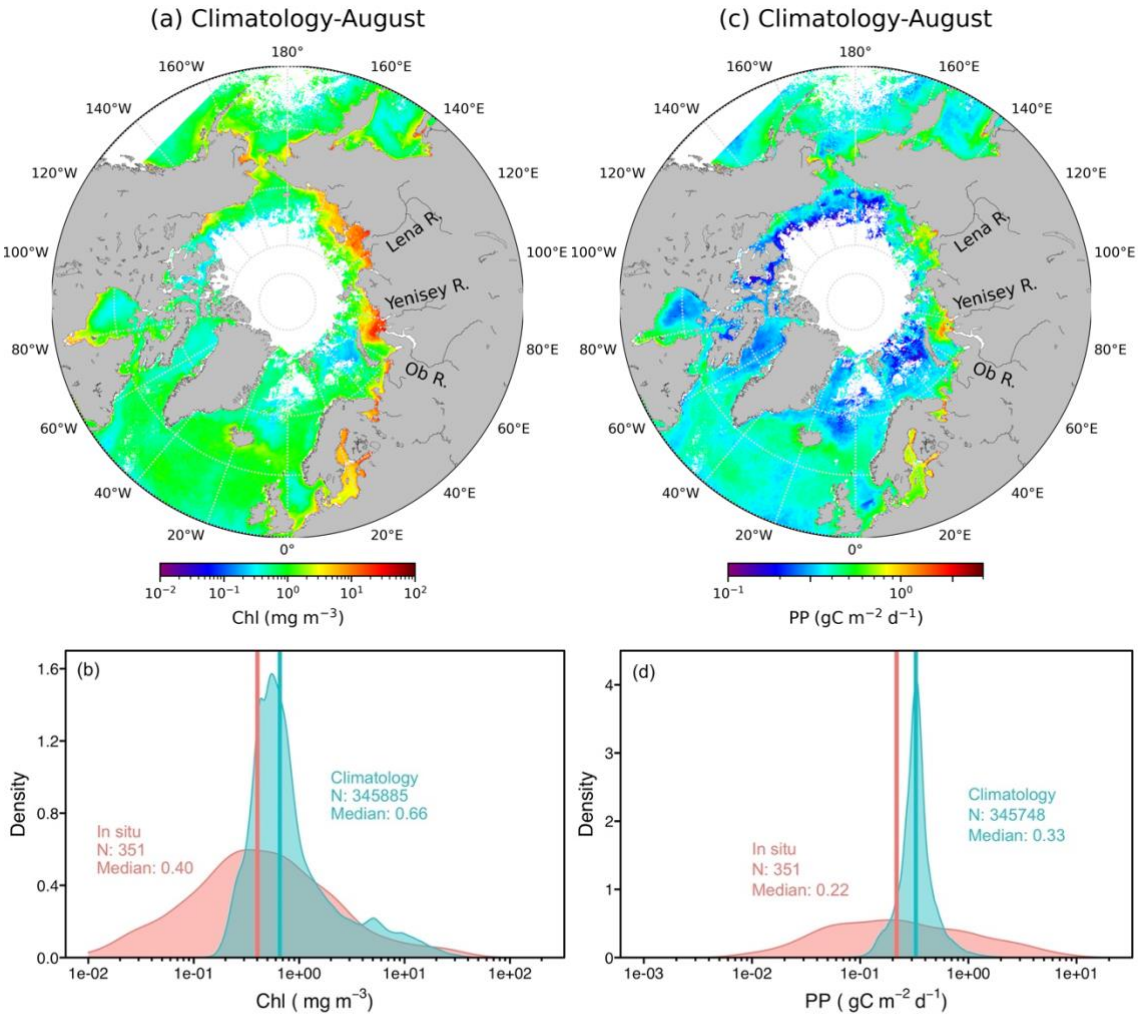

Figure 1.3 (a) Climatology chlorophyll product in August derived through empirical blended algorithm, (c) climatology primary product in August produced through the Arctic primary production model using OC-CCI daily reflectance and chlorophyll products. Kernel density comparison of Chl (b), PP (d) between measurements from PPARR and climatology product.

1.6.2 Bio-optical algorithms evaluations

Chl is one of the most critical variables influencing PP estimates (Bélanger et al., 2013a). Because several chlorophyll *a* algorithms are available, the performance of those chlorophyll *a* algorithms need to be examined first. Figure 1.4 shows the comparison between estimated and measured Chl using various algorithms mentioned above for the 4 water types (see definition in section 1.5.3). Overall, all the algorithms showed a trend of overestimation. OC4v6 and OC4L overestimated the most by 132%. Chl derived from OC4P was the least biased but had the largest MAE (Table 1.4). The MAE of AO.GSM was the smallest, followed by GSM01 and AO.emp, and lastly by the three global algorithms. It was noticeable that the MAE of OC4L was larger than that of the global algorithms, indicating that regional Arctic empirical algorithm was not suitable for the

pan-Arctic Ocean because regional algorithms were subject to the compatibility between the waters under study and the waters from which data were obtained for algorithm development. As for the performance of regression, AO.GSM has the largest r^2, but the slope is not as close to 1 as the other algorithms except the two Arctic regional algorithms OC4P and OC4L.

To rank the overall performances of all the algorithms tested, percent wins between all possible pairs of algorithms were calculated (Table 1.5). Among the three global algorithms, OC3Mv6 performed the best and OC4v6 was the worst. They all outperformed the two regional Arctic algorithms, but lost when compared with AO.emp, GSM01 and AO.GSM. OC4L only performed better than OC4P which had the worst performance among all. As for GSM01, it outperformed the other algorithms except AO.emp and AO.GSM. Percent wins of AO.emp was equal to that of AO.GSM. However, AO.emp had larger overall wins (65.6%). Thus AO.emp was the best algorithm of all.

When look closer between water types, symbols represent waters with high CDM (i.e., 'diamonds' for chl.ACDM and 'plus' for CHL.ACDM) are more scattered distributed than waters with low CDM for all empirical algorithms and GSM01 (Figure 1.4). While this phenomenon is not obvious for AO.GSM. That was because for waters with high CDM, AO.GSM obtained 24 failures (accounts for 16.2% of the total sample) which were excluded for comparisons (see Figure 1.6 and Table 1.6). In other words, AO.GSM is more likely to fail for waters with high CDM. These findings indicate that the high proportion of CDM in the water column is the main obstacle for the success of these empirical and semi-analytical algorithms.

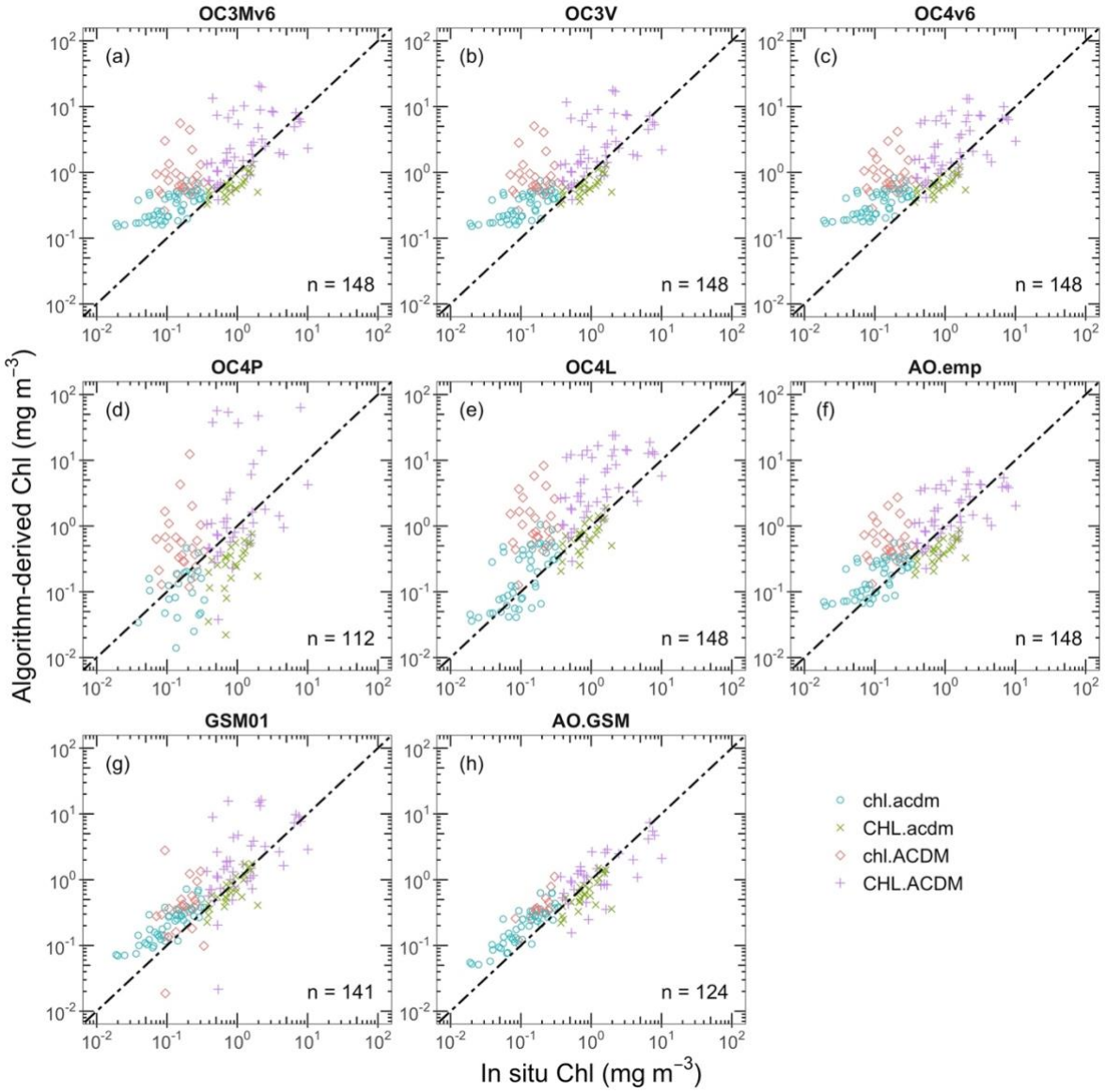

Figure 1.4 Comparisons between estimated and measured Chl for individual chlorophyll *a* algorithm at 4 water types (see context for definition).

Table 1.4 Performance metrics of the various algorithms evaluated.

Algorithm	n	bias	MAE	Overall Wins (%)	r^2	slope
OC3Mv6	148	2.22	2.68	48.9	0.49	0.86
OC3V	148	2.17	2.64	48.0	0.49	0.83
OC4v6	148	2.32	2.75	37.2	0.52	0.83
OC4P	112	1.08	3.16	38.8	0.21	1.61
OC4L	148	2.30	2.82	43.2	0.55	1.28
AO.emp	148	1.36	2.15	65.6	0.54	0.92
GSM01	141	1.59	2.08	58.6	0.62	0.97
AO.GSM	124	1.24	1.73	58.0	0.79	0.77

Table 1.5 Algorithm performance assessed through pair-to-pair comparison.

	Percent Wins							
Algorithm	OC3Mv6	OC3V	OC4v6	OC4P	OC4L	AO.emp	GSM01	AO.GSM
OC3Mv6	-	46.6	27.7	39.9	41.9	72.3	66.9	62.2
OC3V	53.4	-	29.1	39.2	42.6	71.6	67.6	60.8
OC4v6	72.3	70.9	-	39.2	46.6	73.0	73.0	64.9
OC4P	60.1	60.8	60.8	-	56.1	67.6	60.8	55.4
OC4L	58.1	57.4	53.4	43.9	-	67.6	63.5	53.4
AO.emp	27.7	28.4	27.0	32.4	32.4	-	42.6	50.0
GSM01	33.1	32.4	27.0	37.2	36.5	57.4	-	59.5
AO.GSM	37.8	39.2	35.1	39.9	46.6	50.0	35.8	-
Overall Wins	48.9	48.0	37.2	38.8	43.2	65.6	58.6	58.0
Failure				36 (24.3%)			7 (4.7%)	24 (16.2%)

Boxplots were deployed to quantify the difference between measured and estimated Chl by individual algorithm for each water type (Figure 1.5). The MAEs were also labeled. Generally, the MAE of every algorithm (except OC4P and AO.emp) was the smallest for CHL.acdm (1.33 to 1.44), but the largest for chl.ACDM (2.02 to 7.11). Combined with the finding that the MAE for chl.acdm was smaller than that for CHL.ACDM, we can see that the higher the level of CDM relative to Chl, the larger the uncertainties on Chl estimates. Given OC4P had the largest MAE (3.16) and failures (24.3%), it was excluded from further analysis. For chl.acdm, the three global algorithms had the highest MAE up to 2.86, followed by OC4L, GSM01 and AO.GSM. AO.emp got the lowest MAE (1.75), however, it obtained the largest MAE (2.01) for CHL.acdm, which was confirmed by the notable underestimation showed by the 'x' symbols in Figure 1.4. MAEs of the other algorithms were just around 1.4 for CHL.acdm, with GSM01 being the smallest (1.33). As for chl.ACDM and CHL.ACDM, OC4L obtained the largest MAEs (7.11 and 3.48 respectively), indicating that this regional Arctic empirical algorithm is more inapplicable for CDM-rich waters than the global empirical algorithms. AO.emp got the smallest MAE among all empirical algorithms tested for waters with high CDM, but the contrary was found for CHL.acdm. It seems that empirical algorithms only consider the main characteristic of the water bodies, thus not able to work well for all types of waters. The two GSM models had the smallest MAEs for chl.ACDM, and obtained quite good performance for other water types. Although these semi-analytical algorithms tend to generate failures for CDM-rich waters, they seem to be a solution for waters had heterogenous bio-optical properties, such as the AO.

AO.GSM obtained smaller MAEs than GSM01 for waters with high CDM, but it also had 11.5% more failures than GSM01. It is hard to tell which one performs better for such water types. Therefore, the two GSM models were taken out for further statistic comparisons for each water type. Table 1.6 summarizes the performance metrics of GSM01 and AO.GSM for each water type. According to the wins, AO.GSM outperformed GSM01 for chl.acdm and chl.ACDM, but lost for CHL.acdm and CHL.ACDM. Note that even though AO.GSM had 11 failures (accounted 42.3%), it still worked better than GSM01. Figure 1.6 shows the pair-to-pair comparisons, the diamond symbols represent the samples which failed with AO.GSM but succeeded with GSM01. They all belonged to water types with high CDM, and most of them located far from the 1:1 regression line. When excluding the diamonds, AO.GSM outperformed GSM01 with 71.0% wins (see Table 1.6). It seems that AO.GSM has the ability to eliminate retrievals with poor performance to remain robust.

Considering the overall wins, AO.emp was the best chlorophyll *a* algorithm tested, followed by GSM01 and AO.GSM. For water types with high proportion of CDM, the existence of CDM biased the two Arctic regional algorithms OC4P and OC4L most, followed by the three global algorithms, and lastly by AO.emp and the two GSM models. AO.GSM performed better than GSM01 for chl.ACDM, but worse for CHL.ACDM.

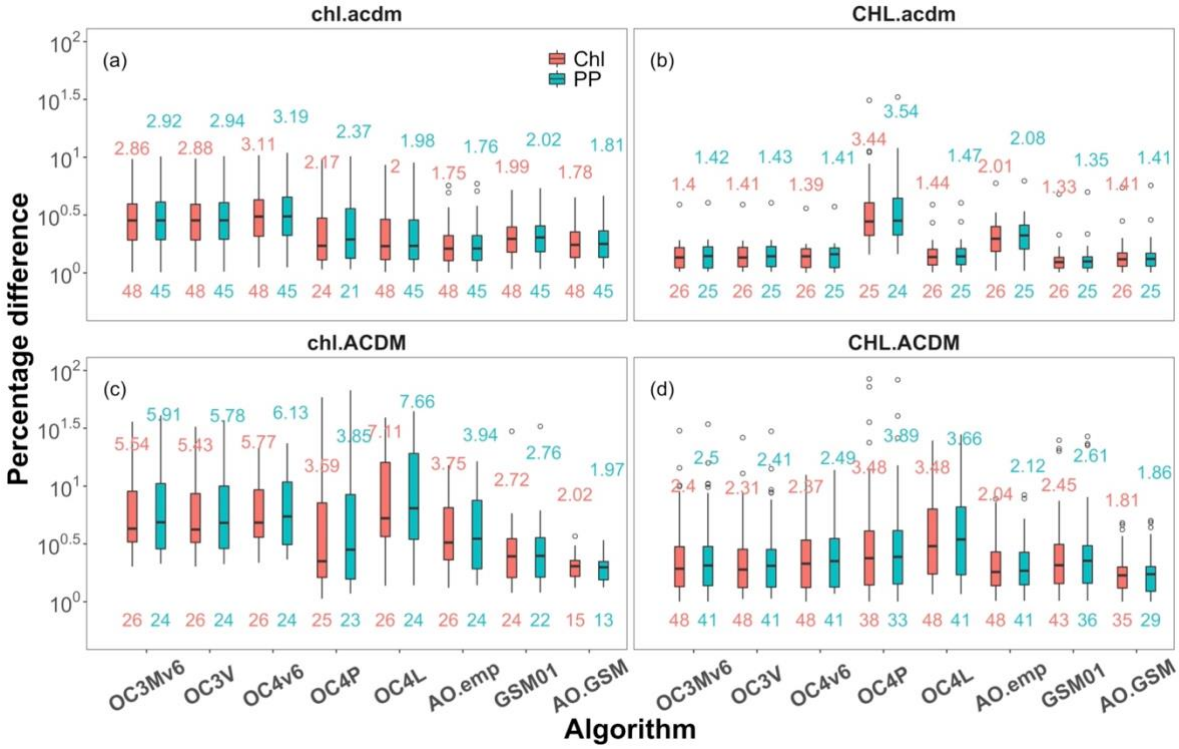

Figure 1.5 Boxplots of absolute difference between measured and estimated Chl (red), between PP derived using measured Chl and PP estimated from algorithm-derived Chl (green) for 4 water types (see context for definition). Labels above boxplots are MAE, below are numbers of samples classified into a certain water type.

Table 1.6 Performance metrics of GSM01 and AO.GSM by individual water type and across all water types.

Water Type	Algorithm	n	bias	MAE	Wins (%)	Failure	r^2	slope
chl.acdm	GSM01	48	1.96	1.99	6.2		0.71	0.85
	AO.GSM	48	1.74	1.78	93.8		0.75	0.92
CHL.acdm	GSM01	26	0.83	1.33	69.2		0.52	1.09
	AO.GSM	26	0.74	1.41	30.8		0.50	1.11
chl.ACDM	GSM01	24	2.10	2.72	34.6	2 (7.7%)	0.08	1.03
	AO.GSM	15	2.02	2.02	57.7	11 (42.3%)	0.65	1.25
CHL.ACDM	GSM01	43	1.57	2.45	47.9	5 (10.4%)	0.27	1.03
	AO.GSM	35	0.92	1.81	41.7	13 (27.1%)	0.47	0.79
Across all	GSM01[a]	124	1.47	1.81	29.0		0.80	0.81
	AO.GSM	124	1.24	1.73	71.0		0.79	0.77

[a]subset of GSM01-derived retrievals with common data to that of AO.GSM.

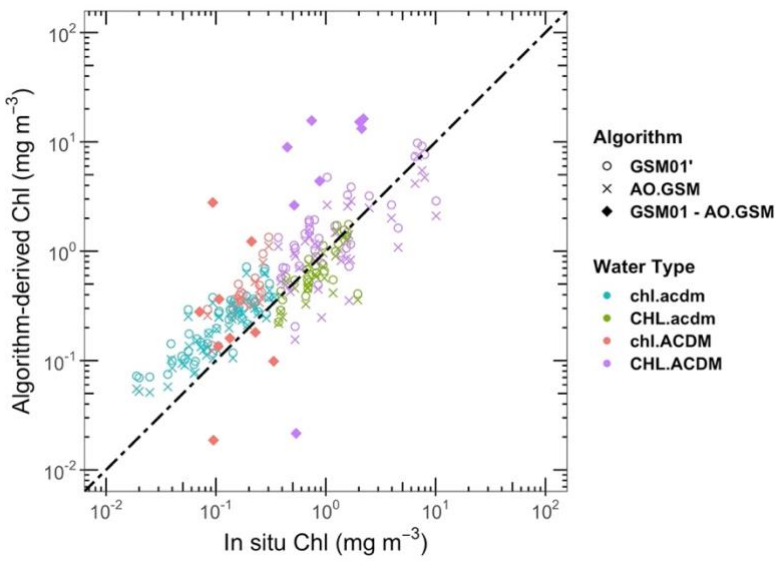

Figure 1.6 Pair-to-pair comparison between GSM01 and AO.GSM, circles and x symbols refer to the same data pairs derived from GSM01 and AO.GSM, diamonds refer to the data failed using AO.GSM but succeeded using GSM01.

1.6.3 Error propagation from Chl to PP

A sensitivity analysis of PP on measured and various algorithms-derived Chl was applied using the Arctic primary production model described above to quantify the error propagation. Briefly, measured Chl and $R_{rs}(\lambda)$ along with the temporally and geographically matched atmospheric parameters were put into the Arctic primary production model to derive spectrally- and vertically-resolved PP (named as PP-Ref). Then only the Chl input was replaced by the Chl estimates derived through various chlorophyll a algorithms mentioned above using measured $R_{rs}(\lambda)$ to obtain PP estimates (named as PP-Algorithm, for instance, PP generated via OC4L derived Chl was called PP-OC4L). Note that, since the primary product model is a bin-based approach, several samples might project to a same bin, therefore the total number of PP estimates was 135 rather than 148. Figure 1.7 shows the comparisons between PP-ref and each PP-Algorithm. Generally, the distributions of PP were more contracted than that of Chl, and the bounds of water types became vague. For instance, some 'plus' symbols which represented water type CHL.ACDM went to the left of some 'circle' symbols which referred to water type chl.acdm, indicating that PP was suppressed in waters with high proportion of CDM even though Chl level was high.

The same boxplots of absolute difference between PP-ref and PP-Algorithm are showed in Figure 1.5. It can be seen that the absolute differences followed the trend of Chl, and the rankings of MAE kept the same as that of Chl but with relative larger values. Taking the best algorithm AO.emp as an example, the MAEs of PP were 0.5%, 3.4%, 5.1%, and 3.9% larger than that of Chl for water type chl.acdm, CHL.acdm, chl.ACDM and CHL.ACDM respectively. The amplifications of difference from Chl to PP were larger in waters with relative

high proportion of CDM. However, considering all the algorithms, the amplification of difference from Chl to PP did not exceed 7%.

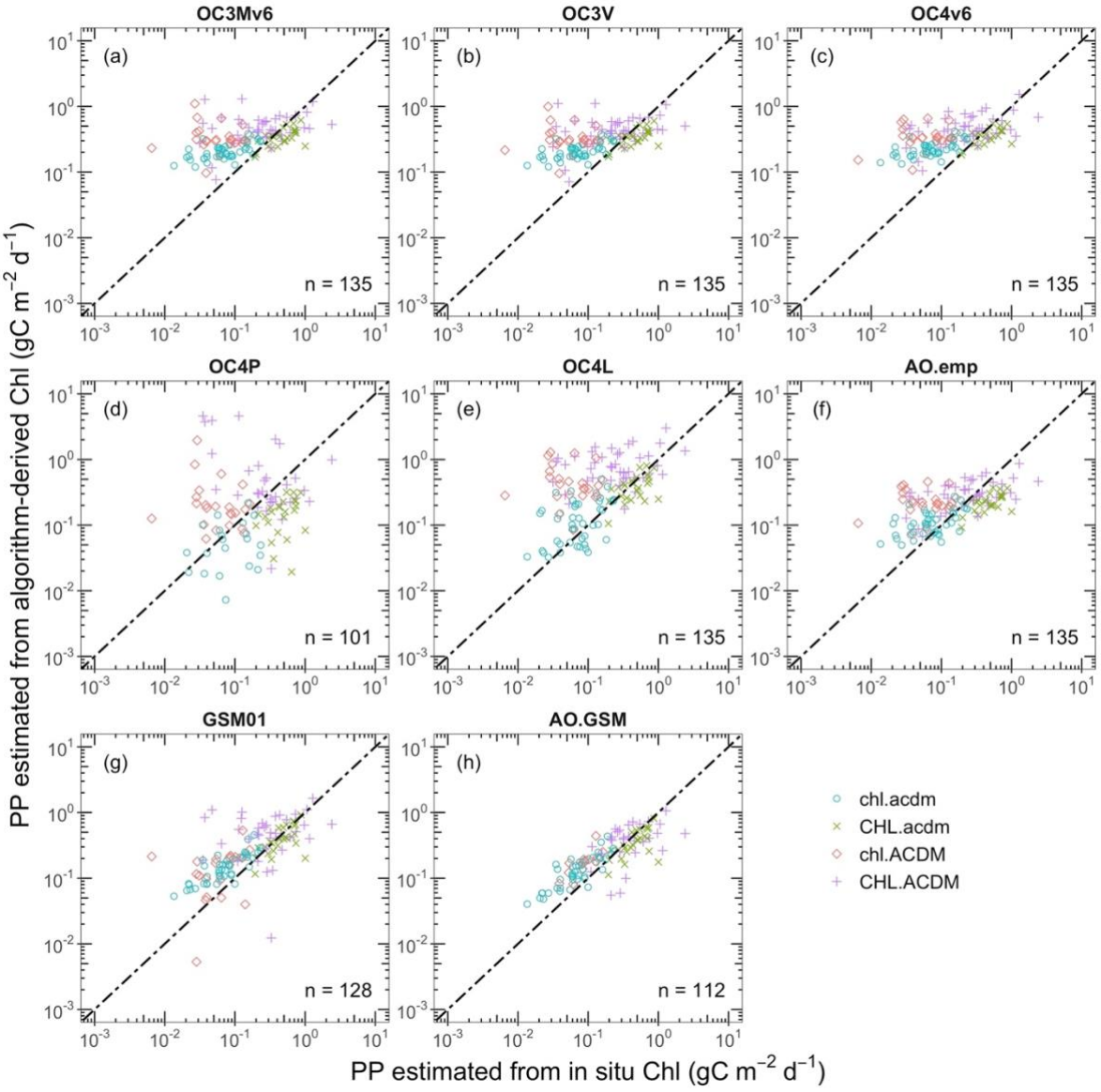

Figure 1.7 Comparisons between PP estimated from in *situ* Chl and PP estimated from algorithm-derived Chl for 4 water types (see context for definition).

1.7 Discussion

1.7.1 Chl retrieval error

Difference between simulated and measured Chl is due to the fact that these chlorophyll a algorithms are not capable to properly estimate the biomass for the AO with distinguish bio-optical characteristics.

For the three global chlorophyll a algorithms - OC3Mv6, OC3V and OC4v6, because the absorption properties of the AO are fundamentally different from typical Case 1 waters, the relationship between R_{rs} and Chl assumed for global waters are problematic for the AO. Many studies (Bélanger et al., 2008; Matsuoka et al., 2013, 2012; Matsuoka et al., 2011; Matsuoka et al., 2007; Mustapha et al., 2012; Wang et al., 2005) have documented that the non-water absorption of the AO is dominated by CDOM even at the phytoplankton absorption peak at 443 nm. Thus, the presence of CDOM at levels higher than the global mean will reduce the R_{rs} signal at blue wavelengths due to its strong absorption. As a consequence, global empirical algorithms using maximum blue-to-green R_{rs} ratio tend to have lower maximum band ratio, leading to an overestimation of Chl. Generally, the predominant influence of CDOM is to increase the intercept of the in *situ* versus algorithm-derived Chl regression and only minimally change the slope (Lewis et al., 2016).

In addition, as a consequence of photo-acclimation to low irradiance and cold temperature of the Arctic, an increase in phytoplankton cell size and/or in intra-cellular pigment concentration decreases the light absorption coefficient per unit Chl (Cota et al., 2004; Matsuoka et al., 2011; Matsuoka et al., 2007). This higher package effect flattens the absorption spectrum of chlorophyll a, especially at the blue absorption peak. Thus, in contrast to the effect of CDOM, relatively larger decrease of a_{ph}^{*} at blue wavelengths than green wavelengths yields larger maximum band ratio, leading to an underestimation of Chl when using global empirical algorithms for the AO. Thus, relative higher pigment package effect decreases the slope of the in *situ* versus estimated Chl regression without appreciably changing the intercept (Lewis et al., 2016).

Overall, difference between simulated and measured Chl is a consequence of combined effects of Chl overestimation due to relative higher CDOM absorption and underestimation due to relative higher pigment package effects. In this study, the three global algorithms showed obvious overestimation at all Chl ranges (Figure 1.4a-c), indicating that relative higher CDOM absorption was the dominant factor that biased Chl estimates in the AO.

The failure of the two Arctic regional chlorophyll a algorithms were imputed to the significant spatial variance of bio-optical properties at a pan-Arctic scale. The AO is a spatially heterogeneous sea. That is the composition of non-water constituents and their bio-optical properties significantly differ from region to region due to various degree of river inputs, nutrient levels, sea ice coverage, shelf width, and circulation patterns (Lewis et al., 2016; Matsuoka et al., 2013). Hence, a single regional empirical algorithm, like OC4L or OC4P tuned for the Beaufort and Chukchi seas, is not appropriate for the entire AO. This is likely reflected in the worse performance than the global empirical algorithms evaluated in the present study (see Figure 1.4 and Table 1.4). Such a degree of variability makes it difficult to establish a standard empirical formulation that provides robust

predictions with acceptable error limits, at least on the scale of the entire Arctic region. Such was the case of AO.emp. Although the MAE of AO.emp was lower than the other algorithms for chl.acdm, for CHL.acdm the MAE was even larger than the global algorithms. Thus, it is recommended to use a semi-analytical algorithm which compensates optical properties in a given location through an optimization process and allows discrimination and quantification of the roles of non-phytoplankton constituents to the optical properties of seawater, to improve the accuracy of Chl estimates from OCRS in polar waters.

The standard semi-analytical algorithm GSM01, with parameters optimized for non-polar Case 1 waters, could not properly represent the combination of water constituents of the AO. In other words, due to the high CDOM proportion in the AO, spectral slope for a_{cdm} should be sharper, and $a_{ph}^{*}(\lambda)$ should be lower to account for higher package effect. That may be the reason why the performance of GSM01 was worse than AO.emp (see Table 1.4). After reparameterized for the AO, AO.GSM outperformed GSM01 in the pair-wise comparison and showed the lowest MAEs for waters at water types chl.ACDM and CHL.ACDM. However, for these two water types, AO.GSM had 24 failures, which represents 16.2% of the total samples. Therefore, in future research, chlorophyll a algorithm which can produce as much as possible effective retrievals with reasonable uncertainty should be sought for.

1.7.2 PP estimate error

PP was estimated using the classical photosynthesis versus light model based on the integration of carbon fixation by phytoplanktonic cells in the present study. The prime determinant of PP variations for ice-free waters in such models designed for OCRS data is Chl, except during seasons when incident irradiance becomes highly limiting. It is expected that errors in Chl should mostly propagate proportionally to PP, especially when all other variables are kept constant from one set of simulations to another, as in our study. In the model we used, however, Chl also drives the vertical distribution of chlorophyll concentration, as well as the chlorophyll-specific absorption coefficient of phytoplankton. Nevertheless, our results suggest and largely confirm that errors in Chl mostly propagate proportionally to PP.

In the present study, because of the lack of coincident PP measurements in the dataset used for algorithm evaluation, we do not know exactly the errors of PP estimates, but we could get an insight by comparing it with the relationship between in *situ* PP and Chl. Figure 1.8(a) shows the relationship between in *situ* PP and Chl using PPARR dataset. It can be seen that, in the range from 0.1 to 1.0 mg m^{-3}, PP varied across three orders from 0.01 to 10.0 gC m^{-2} d^{-1}. Besides, when Chl < 6.0 mg m^{-3}, the triangle symbols were likely evenly distributed along the regression line, while Chl > 6.0 mg m^{-3}, all triangles lay below the regression line. Figure 1.8(b) illustrates the relationship between estimated PP and measured Chl using the dataset used for algorithm evaluation, the regression line of Figure 1.8(a) was also showed for comparison. All symbols were more likely to locate at right of regression line, indicating the estimated PP was somewhat underestimated.

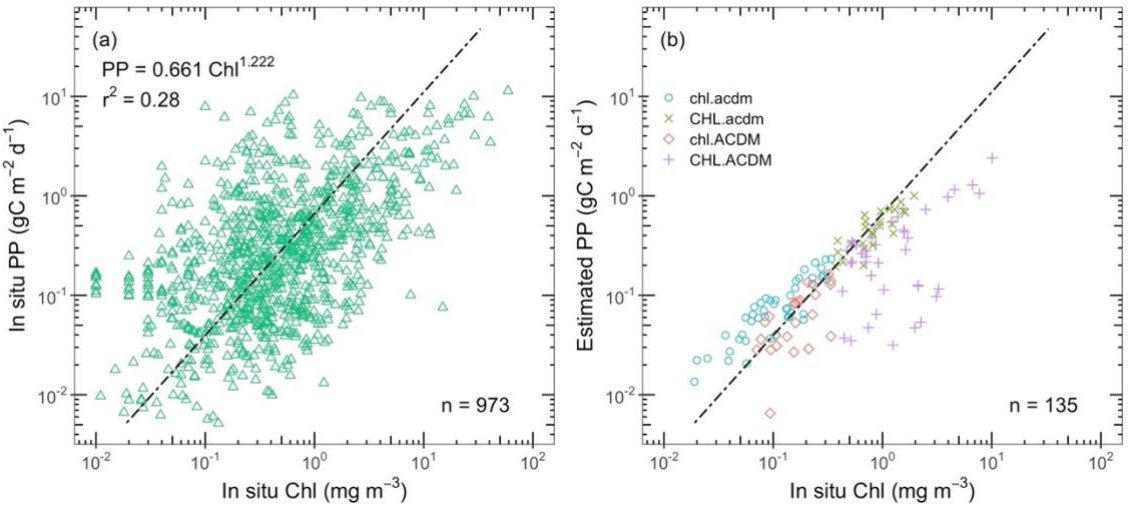

Figure 1.8 (a) Relationship between in *situ* PP and Chl from PPARR, (b) relationship between PP estimates and in *situ* Chl using the dataset used for algorithm evaluation. The dash black line is the regression line between in *situ* PP and Chl from PPARR.

1.7.3 Conclusion

Given that the failure of standard empirical algorithms in the AO is due to the interference by CDM on phytoplankton signal in the visible spectrum, in this study, we evaluated currently available algorithms from a perspective of the impact of CDM. We found that the higher the level of CDM in the water column, the larger it would bias the estimation of Chl. For waters with high CDM, the existence of CDM biased the Arctic regional algorithms (i.e., OC4P and OC4L) the most, followed by the global algorithms, lastly by AO.emp and the two semin-analytical algorithms. Therefore, the use of an empirical algorithm for the entire AO should be avoided when possible. It is recommended to use semi-analytical algorithm (such as AO.GSM) which can discriminate and quantify the roles of non-phytoplankton constituents for the heterogenous AO. However, AO.GSM is more likely to fail for waters with high CDM, thus, semi-analytical algorithm that can produce as much as possible effective retrievals with reasonable uncertainty is still expected in future researches.

Through the sensitivity analysis of Chl on PP estimation, we found that errors in Chl mostly propagate proportionally to PP, and were amplified less than 7%. In addition, by comparing with the relationship between in *situ* PP and Chl, we discovered that the Arctic spectrally- and vertically-resolved primary production model used in this study underestimated PP to some extent. However, sea-truth data is still needed to quantify the error of PP estimations. Our PP calculations provide some quantitative appreciation of the uncertainty in PP estimates that should be expected in Arctic, for different seawater optical categories as defined here.

Chapitre 2 A newly tuned algorithm for the Arctic Ocean: a preliminary solution for CDM-rich waters

Juan Li, Atsushi Matsuoka, Stanford B. Hooker, Xiaoping Pang, Marcel Babin

2.1 Résumé

L'océan Arctique (AO) est l'océan le plus influencé par les rivières. Situés à l'interface terre-mer, les plans d'eau côtiers de l'Arctique où la prolifération du phytoplancton est fréquente sont parmi les plus touchés par le changement climatique. Étant donné que le phytoplancton joue un rôle essentiel dans le transfert d'énergie qui soutient l'ensemble du réseau alimentaire, une estimation précise de la concentration de chlorophylle a (Chl, un indicateur de la biomasse du phytoplancton) est essentielle pour améliorer notre connaissance de l'écosystème marin de l'Arctique et de sa réaction au changement climatique en cours. Cependant, étant donné qu'actuellement le meilleur algorithme semi-analytique AO.GSM échoue trop souvent pour les eaux côtières où le niveau de CDM (matériel coloré et détritique) est généralement élevé, dans cette étude, nous avons optimisé davantage le modèle GSM en ajoutant 620 nm qui pourrait aider à distinguer l'absorption du phytoplancton du CDM, et l'absorption de la diffusion. Nos résultats suggèrent que notre algorithme ajusté GSMA a donné des résultats similaires à AO.GSM en termes de performance de Chl pour les eaux océaniques où le niveau de CDM est généralement faible, mais était beaucoup plus robuste que AO.GSM pour les eaux avec un CDM élevé. Lorsqu'elle a été testée à l'aide du jeu de données COASTlOOC, la GSMA a amélioré la performance des estimations de la Chl de 93%. De plus, l'amélioration concernant les estimations de $a_{cdm}(443)$ (coefficient d'absorption du CDM à 443 nm) était encore plus importante, atteignant jusqu'à 168 %. Ces résultats impliquent que, en l'absence d'autres algorithmes pouvant être appliqués aux eaux côtières avec une grande précision, le GSMA pourrait être une alternative pour récupérer simultanément la Chl et $a_{cdm}(443)$.

2.2 Abstract

The Arctic Ocean (AO) is the most river-influenced ocean. Located at the land-sea interface, Arctic coastal waterbodies where phytoplankton blooms are common are among those most affected by climate change. Since phytoplankton is critical for energy transfer supporting the entire food web, accurate estimation of chlorophyll a concentration (Chl, a proxy of phytoplankton biomass) is critical to improve our knowledge of the Arctic marine ecosystem and its response to the ongoing climate change. However, since currently the best semi-analytical algorithm AO.GSM fails too often for coastal waters where CDM (colored and detrital material) level is usually high, in this study, we further optimized the GSM model by adding 620 nm which help to distinguish the absorption of phytoplankton from CDM, and absorption from scattering. Our results suggest that our tuned algorithm GSMA performed similarly to AO.GSM in terms of the performance of Chl for oceanic waters where CDM level is generally low, but was much more robust than AO.GSM for waters with high CDM. When tested using COASTlOOC data set, GSMA improved the performance of Chl estimates by 93%. In addition, the improvement regarding $a_{cdm}(443)$ (absorption coefficient of CDM at 443 nm) estimates was even larger, reaching up to 168%. These findings imply that, in the absence of other algorithms that can be applied to coastal waters with high accuracy, GSMA might be an alternative to retrieve Chl and $a_{cdm}(443)$ simultaneously.

2.3 Introduction

The Arctic Ocean (AO) contains only 1% of the global volume of seawater but is receiving 11% of the world's river flow (Lammers et al., 2001). Its drainage basin covers 19 millions km^2, even larger than the Arctic Ocean area (14.2 million km^2), making it the most river-influenced and landlocked of all oceans (Lammers et al., 2001; Vörösmarty et al., 2000). Being located at the land-sea interface, Arctic coastal waterbodies are subjected to the combined changes from a wide range of physical-chemical processes, such as large amounts of nutrients input into the AO from river inflow (Dittmar and Kattner, 2003; Frey and McClelland, 2009), coastal upwelling (Tremblay et al., 2011; Williams and Carmack, 2008), wind-mixing (Crawford et al., 2020; Uchimiya et al., 2016), loss of sea ice (Ardyna et al., 2014; Arrigo et al., 2008) and so on, which would foster phytoplankton blooms, making these coastal waterbodies highly dynamic and productive. Given that coastal phytoplankton blooms are a major ecological event providing a substantial part of the annual primary production and energy transfer supporting the entire marine food web (Field et al., 1998; Winder and Sommer, 2012), accurate estimation of phytoplankton biomass in these coastal waterbodies is essential to improve our knowledge about marine ecosystem and its response to ongoing climate change.

IOCCG Polar Seas Working Group has suggested to use semi-analytical algorithm in the AO, especially coastal waters where there are large amounts of CDM (colored and detrital material) resulting from river discharge (IOCCG, 2015). Multiple studies have showed that GSM models might be a good choice. Mustapha et al. (2012) have documented that GSM01, a broadly-used semi-analytical algorithm (Maritorena et al., 2002) outperforms the global (OC4v6, OC3Mv6, OC4Mev6) and Arctic regional (OC4L and OC4P) empirical algorithms for the southeast Beaufort Sea. Besides, they have optimized the parameters of GSM model for the southeast Beaufort Sea and obtained a regional GSM model (N=45, slope = 1.1, R^2=0.76). Recently, Lewis and Arrigo (2020) have tuned the GSM model at a pan-Arctic scale using a large bio-optical database (Lewis et al., 2020), and proven their tuned algorithm AO.GSM performs better than any other algorithms yet applied to the AO. In addition, according to our evaluation of AO.GSM from a perspective of the impact of CDM, AO.GSM-derived Chl estimates are indeed the least biased for waters with high CDM, but the MAE (mean absolute error) is still as high as 2.02. Besides, we noticed that AO.GSM obtained 16.2% failures for CDM-rich waters. It seems that AO.GSM is not that robust for coastal waters.

In this context, we further tuned the GSM model for the AO by adding 620 nm waveband using a high-quality bio-optical in *situ* data set. This is motivated by the fact that for CDM-rich Arctic waters, the signal observed at the additional channel (620 nm) is generally high and less interfered by CDM compared to blue-green wavelengths. Therefore, the tuned model with extra effective and important information at 620 nm should help GSM-like models to obtain better results for such waters. Besides, the tuned model is able to be widely used for satellite applications, such as OLCI (Ocean and Land Colour Instrument). After tuning, it was tested using an Arctic data set which is different from the tuning data set, a non-Arctic coastal data sets and an OLCI satellite image taken at the Lena River Delta.

2.4. Data

2.4.1. Bio-optical in *situ* data sets

Three bio-optical datasets were used in this study. The first dataset was collected in the Arctic Ocean and was used to tune the GSM model (from hereafter referred to as T-Arctic). The second dataset is also from the Arctic Ocean and was used in this study for validation purpose (named as V-Arctic), together with a non-Arctic coastal dataset, the COASTlOOC (Coastal Surveillance Through Observation of Ocean Color) one.

The T-Arctic dataset is composed of five cruises: MALINA, ICESCAPE2010, ICESCAPE2011, Tara Oceans Polar Circle expedition, and GREEN EDGE. There are 148 samples in total containing concurrent measurements of above-water remote-sensing reflectance ($R_{rs}(\lambda)$) and Chl. Numbers of coincident phytoplankton absorption spectra $a_{ph}(\lambda)$, absorption coefficient of CDM at 443 nm ($a_{cdm}(443)$), and backscattering coefficient at 443 nm ($b_{bp}(443)$) are 101, 96 and 36, respectively.

The V-Arctic data set includes in *situ* measurements from ArcticNet2011, ArcticNet2013, and AREX2017 cruises. Data contributed by SB Hooker are also involved. As for COASTlOOC dataset, it consists of measurements in various coastal waters around Europe during six campaigns in 1997 and 1998. Details can be found in (Babin et al., 2003; Doron et al., 2007). For these two validation datasets, only samples have concurrent measurements of $R_{rs}(\lambda)$ and Chl were kept in this study, and the total numbers of samples are 77 and 168 for V-Arctic and COASTlOOC, respectively. Details about numbers of stations, sampling dates, sampling regions and data sources of the two Arctic datasets are summarized in Table 2.1, station locations are shown in Figure 2.1.

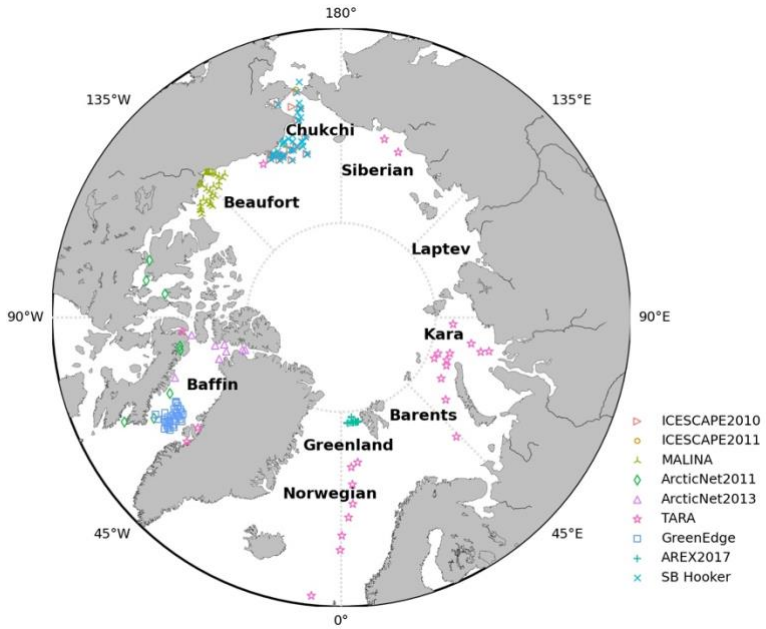

Figure 2.1 Map of the Arctic Ocean showing the locations of stations from various datasets.

Table 2.1 Summary of in *situ* datasets.

Data	Station	Year	Month	Region	Source
MALINA	37	2009	July-August	Southern Beaufort Sea	SeaBASS
ICESCAPE2010	34	2010	June-July	Chukchi and Beaufort Sea	SeaBASS
ICESCAPE2011	18	2011	June-July	Chukchi and Beaufort Sea	SeaBASS
ARCTICNET2011	9	2011	August	Baffin Bay	Individual
ARCTICNET2013	9	2013	August	Baffin Bay	Individual
TARA	27	2013	May-November	Polar circle	SeaBASS
GREEN EDGE	34	2016	June-July	Baffin Bay	Individual
AREX	11	2017	July	Greenland Sea	Individual
SB Hooker	48	2010, 2013-2017	March-December	Arctic Ocean	Individual
COASTlOOC	168	1997-1998	January-December	Europe coastal areas	Individual

$R_{rs}(\lambda)$ measurements

$R_{rs}(\lambda)$ (sr^{-1}) in the two Arctic data sets were determined with the same instrument, the Compact-Optical Profiling System (C-OPS, Biospherical Instrument Inc.) which has been comprehensively documented in Hooker et al. (2013). Briefly, in-water upwelling radiance $L_u(\lambda, z)$, in-water downward irradiance $E_d(\lambda, z)$, above-water downward solar irradiance ($E_s(\lambda)$), pressure/depth, and dual axes tilts were measured simultaneously. After normalization by $E_s(\lambda)$ and 5° tilt filtering, $L_u(\lambda, z)$ and $E_d(\lambda, z)$ were extrapolated to subsurface values $L_u^{0-}(\lambda)$ and $E_d^{0-}(\lambda)$ through progressively optimized depth interval within the surface layer. Finally, $R_{rs}(\lambda)$ was calculated as: $R_{rs}(\lambda) = 0.54L_u^{0-}(\lambda)/(E_d^{0-}(\lambda)/0.97)$. Details of the process protocols are described in Antoine et al. (2013).

For the COASTlOOC data set, in-water upwelling irradiance $E_u(\lambda, z)$ and downwelling irradiance just above the sea surface $E_d^{0+}(\lambda)$ were measured with a Satlantic free-fall SPMR (SeaWiFS Profiling Multichannel Radiometer) and SMSR (SeaWiFS Multichannel Surface Reference), respectively (Bélanger et al., 2008). $E_u^{0-}(\lambda)$ was obtained by extrapolating $E_u(\lambda, z)$ to subsurface by fitting an exponential function. Then $L_u^{0-}(\lambda)$ was calculated as $L_u^{0-}(\lambda) = E_u^{0-}(\lambda)/3.8$ (Bélanger et al., 2008). Afterwards, $R_{rs}(\lambda)$ was obtained by the same process described above. Note that, in the present study, only common wavebands (412, 443, 490, 510, 555, 620, 670 nm) were used.

Chl measurements

All Chl measurements were determined by High-Performance Liquid Chromatography (HPLC). Generally, 25 mm GF/F filters were used to collect phytoplankton from seawater samples. Filters were extracted in 100% methanol, disrupted by sonication and clarified by filtration (GF/F Whatman) before being analyzed by HPLC later in the laboratory obtain separated pigments (Ras et al., 2008; Van Heukelem and Thomas, 2001). Finally, total chlorophyll a pigment concentration was defined as the sum of mono- and divinyl chlorophyll a concentrations, chlorophyllide a and the allomeric and epimeric forms of chlorophyll a (Hooker and Zibordi, 2005; Reynolds et al., 2016).

Absorption measurements

Only the absorption measurements of the T-Arctic dataset were used in this study for algorithm tuning. Absorption spectra of particulate $a_p(\lambda)$ (m^{-1}) and non-algal particles $a_{nap}(\lambda)$ (m^{-1}) were determined using a Perkin-Elmer Lambda-19 spectrophotometer equipped with a 15 cm integrating sphere following the methodology described in (Bricaud et al., 2010; Kishino et al., 1985; Stramski et al., 2015). Phytoplankton absorption spectra $a_{ph}(\lambda)$ were calculated by subtracting $a_{nap}(\lambda)$ from $a_p(\lambda)$. The chlorophyll-specific absorption spectra for phytoplankton $a^*_{ph}(\lambda)$ (m^2 mg^{-1}) are defined as $a_{ph}(\lambda)$ normalized by Chl. $a_{cdom}(\lambda)$ was measured using a liquid core waveguide system, UltraPath following (Miller et al., 2002). Absorption spectra of CDM ($a_{cdm}(\lambda)$, m^{-1}) is the sum of $a_{cdom}(\lambda)$ and $a_{nap}(\lambda)$. Spectral slope of $a_{cdm}(\lambda)$ (S) was calculated by fitting individual spectra (350~500 nm) to equation (10) below with reference waveband $\lambda_0 = 443$.

2.4.2 Satellite image

For application purposes, a Sentinel 3B OLCI image (file name: S3B_OL_2_WFR____20200910T031808_20200910T032108_20200911T114327_0179_043_175_1620_MAR_O_NT_002.SEN3) of full resolution (~300 m) around the Lena River delta taken on 10 September 2020 was downloaded from https://catalogue.onda-dias.eu. $R_{rs}(\lambda)$ was derived from reflectance product by dividing by π, which was then used to generate Chl and $a_{cdm}(443)$ through GSM models.

2.5 Methods

2.5.1. GSM model

Gordon et al. (1988) have found the following functional relationship between $r_{rs}(\lambda)$ and Inherent Optical Properties (IOPs):

$$r_{rs}(\lambda) = g_0 \frac{b_b(\lambda)}{a(\lambda)+b_b(\lambda)} + g_1\left(\frac{b_b(\lambda)}{a(\lambda)+b_b(\lambda)}\right)^2 \quad (5)$$

Where $g_0 \approx 0.0949$ and $g_1 \approx 0.0794$ for oceanic case 1 waters. Backscattering $b_b(\lambda)$ and absorption spectra $a(\lambda)$ can be expanded as:

$$b_b(\lambda) = b_{bw}(\lambda) + b_{bp}(\lambda) \quad (6)$$

$$a(\lambda) = a_w(\lambda) + a_{ph}(\lambda) + a_{cdm}(\lambda) \quad (7)$$

Absorption spectra and backscattering spectra of seawater ($a_w(\lambda)$ and $b_{bw}(\lambda)$ respectively) are assumed to be known constants (Morel, 1974; Pope and Fry, 1997). The non-water IOP spectra are then parameterized in terms of a known shape but an unknown magnitude:

$$b_{bp}(\lambda) = b_{bp}(\lambda_0)(\lambda/\lambda_0)^{-\eta} \quad (8)$$

$$a_{ph}(\lambda) = \mathrm{Chl}\, a^*_{ph}(\lambda) \quad (9)$$

$$a_{cdm}(\lambda) = a_{cdm}(\lambda_0)e^{-S(\lambda-\lambda_0)} \quad (10)$$

Where $a^*_{ph}(\lambda)$ is the chlorophyll a specific absorption coefficient, S is the spectral decay constant for $a_{cdm}(\lambda)$, η is the power-law exponent for the particulate backscattering spectra, and λ_0 is a scaling wavelength (443 nm). These 3 model parameters (termed as a vector Ψ hereafter) are pre-optimized and then used as model parameters of GSM. Afterwards, a certain optimization method (e.g., Ameoba, Quasi-Newton, Gauss-Newton, etc. Mu et al. (2011)) is applied to retrieve the 3 unknowns ($\Theta = \{\mathrm{Chl}, a_{cdm}(443), b_{bp}(443)\}$) by minimizing the mean square difference between modeled and measured $r_{rs}(\lambda)$.

2.5.2 Simulated annealing optimization

In order to optimize the parameters of GSM model, the simplest way is to list all potential interacting sets of Ψ within the assumed limits for each parameter. For a^*_{ph}, S and η, the associated limits are [0.001, 0.3 m^2 mg^{-1}], [0.01, 0.035 nm^{-1}], and [0, 4.3], respectively. But since the number of possible sets of Ψ is too large and the GSM model is highly nonlinear, this simplest exhaustive method would be extremely time-consuming and labor costly. To circumvent this complicated problem, an iterative heuristic method, simulated annealing, was deployed as it has been proven very useful to search for global optimization of complex non-linear objective function with large numbers of optima (Xiang et al., 2013). Basically, simulated annealing is a hill-climbing method except that, instead of picking the best move, it picks a random move. This randomness introduced allows it to ultimately find a global optimum by accepting worse move with a certain probability. This feature

also reduces the importance of the first guess used to initiate the process which is often a critical aspect of minimization techniques based on the steepest descent methods.

Simulated annealing includes three basic elements: 1) a cost function to evaluate the performance of the model when a set of Ψ is given, 2) a candidate generator that randomly proposes new values for Ψ, and 3) a decreasing temperature that introduces the randomness in the process and controls the overall progress.

Firstly, cost function was used for the quantification of the model performance for a given set of Ψ proposed by the candidate generator. It was also the objective to be optimized. In this study, a modified version of the cost function described in (Kostadinov et al., 2007) was adopted:

$$CF = 0.2N_{INV} + \sum_{k=1}^{N_\Theta}(a_k|1 - r_k^2| + b_k|1 - Slope_k| + c_k\, RMSE_k) \quad (11)$$

N_{INV} is the number of invalid retrievals. The effective ranges of Chl, $a_{cdm}(443)$, and $b_{bp}(443)$ are [0.01, 64 mg m^{-3}], [0.0001, 20 m^{-1}], and [0.0001, 1.0], respectively. r_k^2 and $Slope_k$ are the square of the determination coefficient and the slope generated through type II regression between the kth measured and estimated variable in log scale, respectively. $RMSE_k$ is the root mean square error of the kth variable. a_k, b_k, and c_k are subjective weights associated with R_k^2, $Slope_k$ and $RMSE_k$. For the first retrieval Chl, a_1, b_1, and c_1 were assigned 1, 1.5, and 1 separately. For the second retrieval $a_{cdm}(443)$, because only 96 of the total 148 samples have concurrent $a_{cdm}(443)$ measurements, thus a_2, b_2 and c_2 were set as 0.65, 0.98, and 0.65 to keep the weight relative to Chl. Since merely 24.3% of the total samples has coincident $b_{bp}(443)$ measurements, the performance of $b_{bp}(443)$ estimates was not determined in this study. Therefore, the number of retrievals N_Θ in this case is 2.

GenSA package in R program was adopted to realize the parts of candidate generator and temperature control process as it has been proven to be robust and efficient in searching for global optimal solution compared with other packages (such as differential evolution algorithm "DEoptim" (Mullen et al., 2011) and genetic algorithm "rgenoud" (Mebane Jr and Sekhon, 2011)) (Xiang et al., 2017). Inside the package, the candidate generator is highly dependent on temperature in the optimization process. That is, the next candidate is generated accordingly to Cauchy-Lorentz distribution with scale proportional to the actual temperature (Xiang et al., 2017), which needs to be initialized and will decrease according to the logarithmic cooling schedule described in (Bélisle, 1992). Note that, the starting temperature is of significant importance because it directly influences the likelihood of accepting worse responses and thus the stochastic part of the optimization. When temperature is high, solution that is worse than the current solution is kept more often. This property allows for a more extensive search for the global optimum, making it the fundamental part of simulated annealing optimization. Apart from these 3 basic elements, GenSA also provides other controlling parameters, such as the upper and lower bounds of Ψ to be optimized, maximum number of iterations, maximum running time, etc. In this study, the upper and lower bounds of Ψ were set according to their limits mentioned above, the other controlling parameters were kept as the default values assigned inside the package as they have been proven to work well for general optimization cases (Xiang et al., 2017). The flowchart of the whole tuning process is illustrated in Figure 2.2.

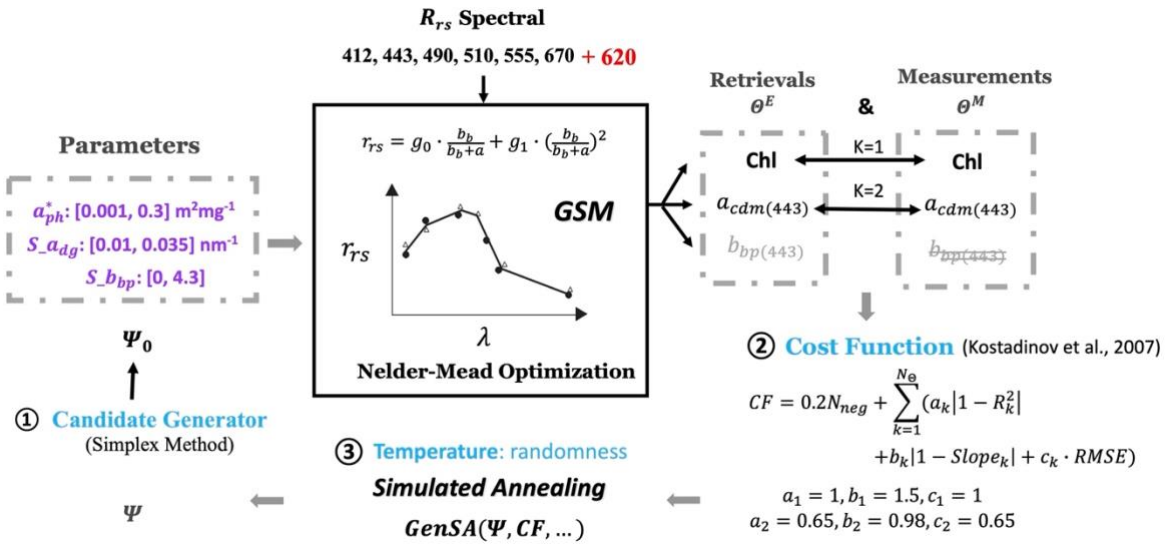

Figure 2.2 Flow chart illustrating the strategy used to find the best set of input parameters of the GSM model (see context for variable definitions). To be brief, firstly, candidate generator was used to propose new set of parameters φ. Then for a given φ, the performance was quantified using the cost function. The third part is temperature which is used to control the whole process and also introduce the randomness to enable the model to jump out of local minimum thus to find global minimum. Finally, when the process cool down as designed, it will return the best parameter for the AO.

Table 2.2 Model Parameters for GSM01, AO.GSM, and GSMA.

Parameters	GSM01	AO.GSM	GSMA	MM[a]
$a^*_{ph}(412)$	0.00665	0.28503	0.00646	0.05120
$a^*_{ph}(443)$	0.05582	0.21099	0.06243	0.05923
$a^*_{ph}(490)$	0.02055	0.089298	0.02471	0.04157
$a^*_{ph}(510)$	0.01910	0.066926	0.03181	0.02626
$a^*_{ph}(555)$	0.01015	0.029377	0.01407	0.00884
$a^*_{ph}(620)$	-	-	0.00677	0.00770
$a^*_{ph}(670)$	0.01424	0.15073	0.01670	0.02431
S	0.0206	0.018996	0.0196	0.0142
η	1.0337	1.3309	1.0316	-

[a]MM refers to measured median values.

2.5.3 Evaluation metrics

The performance of GSM models are assessed following the metrics described in Seegers et al. (2018), that is, the number of effective retrievals, bias and mean absolute error (MAE), percent wins through pair-wise comparison, slope and coefficient of determination (r^2) for log-transformed variable via type II reduced major axis (RMA) regression (Legendre, 1998):

$$\text{bias} = 10^{\text{mean}(log10(X^M) - log10(X^E))} \quad (12)$$

$$\text{MAE} = 10^{\text{mean}|log10(X^M) - log10(X^E)|} \quad (13)$$

Where X stands for Chl or $a_{cdm}(443)$.

2.5.4 Classification

Based on measured median value of Chl (0.35 mg m^{-3}), we split the in *situ* data set by half. For the part with Chl $\leq$ 0.35 mg m^{-3}, samples with $a_{cdm}(443) \leq 0.067$ m^{-1} were classified as chl.acdm, the others with $a_{cdm}(443) > 0.067$ m^{-1} were regarded as chl.ACDM. The same procedure was applied to the other part of the dataset with Chl > 0.35 mg m^{-3}. Therefore, we also got CHL.acdm and CHL.ACDM classes. The classification approach is summarized in Table 2.3.

Table 2.3 Classification criteria.

Water type	Threshold	Number
chl.acdm	Chl ≤ 0.35 mg m^{-3}, $a_{cdm}(443) \leq 0.067$ m^{-1}	48
CHL.acdm	Chl > 0.35 mg m^{-3}, $a_{cdm}(443) \leq 0.067$ m^{-1}	26
chl.ACDM	Chl ≤ 0.35 mg m^{-3}, $a_{cdm}(443) > 0.067$ m^{-1}	26
CHL.ACDM	Chl > 0.35 mg m^{-3}, $a_{cdm}(443) > 0.067$ m^{-1}	48

2.6 Results and discussions

2.6.1 Optimized algorithm GSMA

One innovation of our tuned GSM algorithm (GSMA) compared to AO.GSM (Lewis and Arrigo, 2020) was the addition of 620 nm waveband. For optimization, 148 coincident in *situ* measurements of R_{rs} (at 412, 443, 490, 510, 555, 620 and 670 nm) and Chl, accompanied by 96 concurrent $a_{cdm}(443)$ were used in the simulated annealing optimization strategy to find out the optimal $\Psi = \{a_{ph}^*(\lambda), S, \eta\}$ (section 2.2). Table 2.2 lists the Ψ for GSM01, AO.GSM and GSMA. The measured median values of $a_{ph}^*(\lambda)$ and S are also showed for comparison, η is missing due to the lack of concurrent measurements.

In Table 2.2, we can see that $a_{ph}^*(\lambda)$ of GSMA are closer to the measured median values when compared with GSM01 and AO.GSM, especially at 620 nm. Looking more closely at GSMA, $a_{ph}^*(510)$ is higher than the value at 490 nm, and $a_{ph}^*(412)$ is much smaller than the measured median value, which is not realistic. However, the side effects of these anomalous parameters are somewhat compensated by the influences of higher S and lower η used in the model (Lewis and Arrigo, 2020; Maritorena et al., 2002). Although the optimized Ψ is not ideal, we accept it as long as it helps to improving the accuracy of Chl estimates.

Since AO.GSM algorithm is currently the best semi-analytical chlorophyll a algorithm in the AO (Lewis and Arrigo, 2020), Chl retrievals generated via AO.GSM were compared with that derived through our tuned algorithm GSMA using the T-Arctic data set (Figure 2.3(a) and Table 2.4). Seen from Figure 2.3(a), when measured Chl < 0.1 and Chl > 5.0 mg m^{-3}, 'x' symbols represented GSMA distributed closer to the 1:1 line, indicating better performance. In the range from 0.1 to 5.0 mg m^{-3}, GSMA produced 14 (accounts for 9.5% of the total samples) more retrievals belonging to either chl.ACDM or CHL.ACDM water type, than AO.GSM (see the diamonds in Figure 2.3(a)). As for the performance matrices showed in Table 2.3, both GSMA and AO.GSM had positive biases (1.09 and 1.24 respectively), showing a trend of overestimation. GSMA-derived Chl retrievals were less biased, and the regression slope was much closer to 1. However, because several 'x' symbols and diamonds distributed far from the 1:1 line (see Figure 2.3(a)), resulting in the higher MAE and lower determination coefficient r^2 of GSMA than that of AO.GSM. In terms of the decision metric wins, GSMA outperformed AO.GSM with 59.5% wins overall. As for each water type, except CHL.acdm, GSMA performed better than AO.GSM. The percentage wins at chl.acdm, chl.ACDM and CHL.ACDM were 89.6%, 69.2% and 52.1%, respectively. However, we must recognize that the improvement of GSMA is limited to some extent. For chl.acdm, GSMA improved the accuracy of Chl estimats by 22%, while for CHL.acdm, it was AO.GSM-derived Chl retrievals that were less biased. As for waters with high CDM, the MAEs of GSMA were larger than that of AO.GSM. The reason why GSMA outperformed AO.GSM for these water types was that GSMA generated 14 more valid retrievals with however low accuracy (see the 'diamond' symbols in Figure 2.4(a)). In other words, GSMA only increased its robustness for waters with high CDM but not its accuracy when compared with AO.GSM.

$a_{cdm}(443)$ is another retrieval of GSM models. Comparison between measured and estimated $a_{cdm}(443)$ derived from AO.GSM and GSMA is shown in Table 2.4 and Figure 2.3(b). There was obvious underestimation when $a_{cdm}(443)$ < 0.2 and $a_{cdm}(443)$ > 2.0 m^{-1} by AO.GSM, resulting in scattered circles showed in Figure 2.3(b). Besides, the high MAE (2.99) and 33.7% failures confirmed the poor performance of $a_{cdm}(443)$ retrievals via AO.GSM. While for our tuned algorithm GSMA, the 168% improvement in the accuracy and wins as high as 91.6% showed overwhelming superiority over AO.GSM in terms of $a_{cdm}(443)$ estimates.

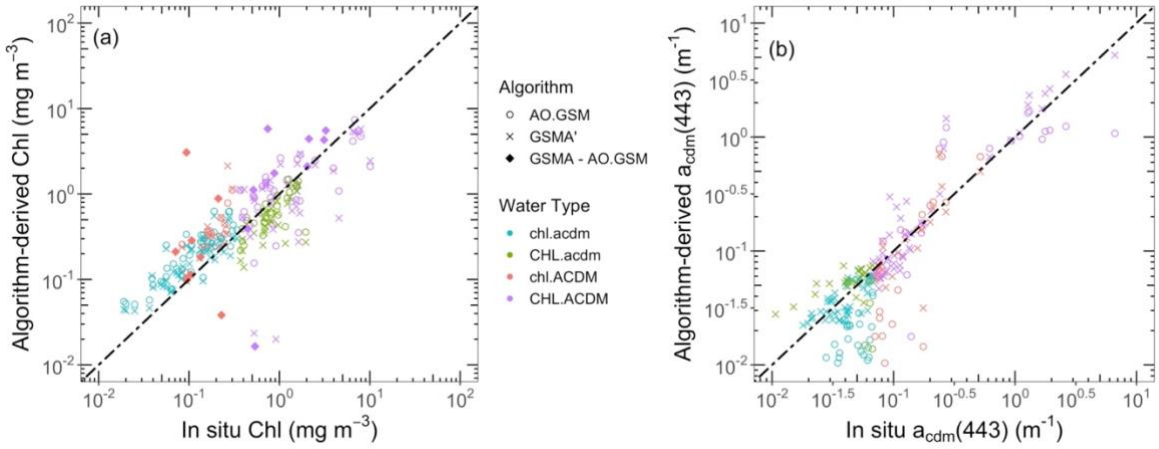

Figure 2.3 Results of AO.GSM and GSMA algorithms for (a) Chl, and (b) $a_{cdm}(443)$ using T-Arctic dataset. circles and x symbols refer to the same data pairs derived through AO.GSM and GSMA, diamonds refer to the data failed via AO.GSM but succeeded via GSMA.

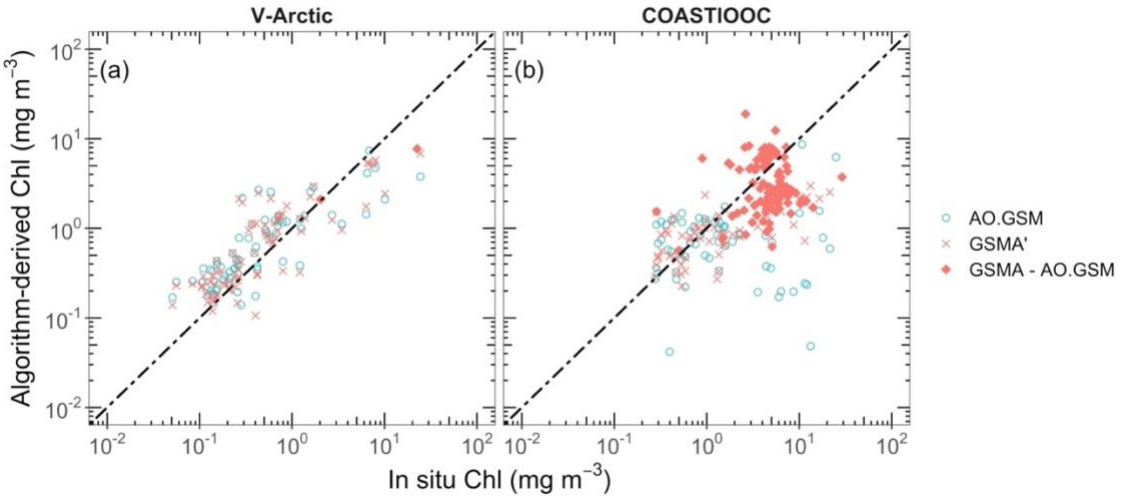

Figure 2.4 Validation of AO.GSM and GSMA using the (a) V-Arctic and (b) COASTlOOC datasets. Circles and x symbols refer to the same data pairs derived through AO.GSM and GSMA, diamonds refer to the retrievals failed using AO.GSM but succeeded using GSMA.

It is well acknowledged that algorithm tuning and validation should base on different independent datasets. Thus, another Arctic data set (V-Arctic) was applied to validate Chl performance of our tuned algorithm GSMA. For comparison, Chl estimates derived through AO.GSM were also shown in Figure 2.4(a) and Table 2.4. No

matter the metric among bias, MAE, wins, slope or r^2, GSMA showed better performance than AO.GSM, indicating that our tuned algorithm indeed improved the performance of Chl estimates in the AO. However, the overall improvement of accuracy is merely 8%.

Table 2.4 Performance matrices of Chl and $a_{cdm}(443)$ derived by AO.GSM and GSMA using T-Arctic, V-Arctic, and COASTlOOC datasets, respectively.

Data	Algorithm	n	bias	MAE	Wins (%)	Failure	r^2	slope
T-Arctic n = 148	**chl.acdm, n = 48**							
	AO.GSM	48	1.74	1.78	10.4		0.75	0.92
	GSMA	48	1.48	1.56	89.6		0.74	0.88
	CHL.acdm, n = 26							
	AO.GSM	26	0.74	1.41	92.3		0.50	1.11
	GSMA	26	0.59	1.71	7.7		0.47	1.26
	chl.ACDM, n = 26							
	AO.GSM	15	2.02	2.02	19.2	11 (42.3%)	0.65	1.25
	GSMA	23	1.98	2.31	69.2	3 (11.5%)	0.08	1.26
	CHL.ACDM, n = 48							
	AO.GSM	35	0.92	1.81	39.6	13 (27.1%)	0.47	0.79
	GSMA	44	0.82	2.25	52.1	4 (8.3%)	0.27	1.26
	Across all, n = 148							
	AO.GSM	124	1.24	1.73	35.8	24 (16.2%)	0.79	0.77
	GSMA	141	1.09	1.90	59.5	7 (4.7%)	0.55	0.94
	$a_{cdm}(443)$, n = 95							
	AO.GSM	63	0.36	2.99	8.4	32 (33.7%)	0.74	1.46
	GSMA	95	0.89	1.31	91.6		0.92	1.15
V-Arctic n = 77	AO.GSM	74	1.38	1.92	35.1	3 (3.9%)	0.70	0.78
	GSMA	76	1.28	1.84	63.6	1 (1.3%)	0.71	0.84
COASTlOOC n = 168	AO.GSM	65	0.46	3.19	17.3	103 (61.3%)	0.00	0.05
	GSMA	161	0.65	2.26	81.5	7 (4.2%)	0.36	0.77

2.6.2 Satellite application

A general insight of the applicability of AO.GSM and GSMA for coastal waters was obtained by applying them to the OLCI image taken by Sentinel 3B around the Lena River delta on 10 September 2020 (see Figure 2.5). We can see that AO.GSM failed to generate valid Chl retrievals along the coastal areas, resulting in a blank gap between the shelf and the open ocean. The performance of the accompanied retrieval $a_{cdm}(443)$ was even worse. Contrary to Chl, AO.GSM was only capable to produce $a_{cdm}(443)$ along the coastal areas but led to missing values in the open ocean (see Figure 2.5(b)). For GSMA, it filled in the missing pixels caused by AO.GSM both for Chl and $a_{cdm}(443)$ estimates (see Figure 2.5(c)-(d)), indicating its strong robustness for coastal waters.

Figure 2.6 shows the kernel density plot of AO.GSM and GSMA generated Chl estimates for further comparisons. Failures of AO.GSM and GSMA accounted for 11.2% and 1.3% of the total effective pixels (7207409), respectively. GSMA-derived Chl reached up to ~40.0 mg m^{-3}, and the median value is 2.09 mg m^{-3}. While the maximum and median of AO.GSM-derived Chl were ~10.0 and 1.39 mg m^{-3} separately. As for $a_{cdm}(443)$, GSMA produced 7204683 (accounted 99.96%) retrievals, while the number of effective retrievals

generated via AO.GSM was merely 834325 (11.6%). Thus, GSMA exhibited much better robustness than AO.GSM when applied to the AO, especially for coastal waterbodies.

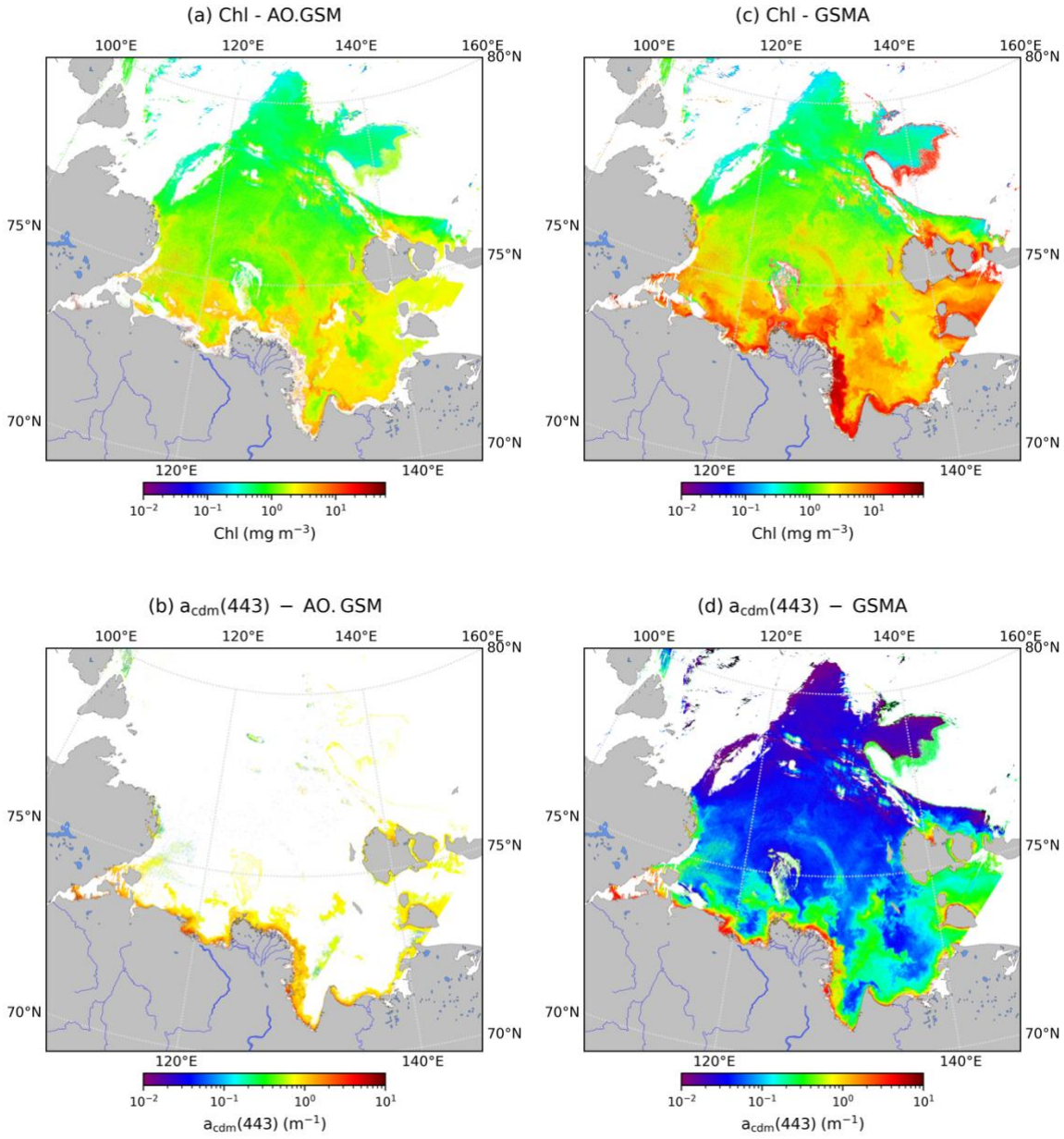

Figure 2.5 AO.GSM-derived (a) Chl, (b) $a_{cdm}(443)$, and GSMA-derived (c) Chl, (d) $a_{cdm}(443)$ using the OLCI reflectance image taken by Sentinel 3B around the Lena River plume on 10 September 2020.

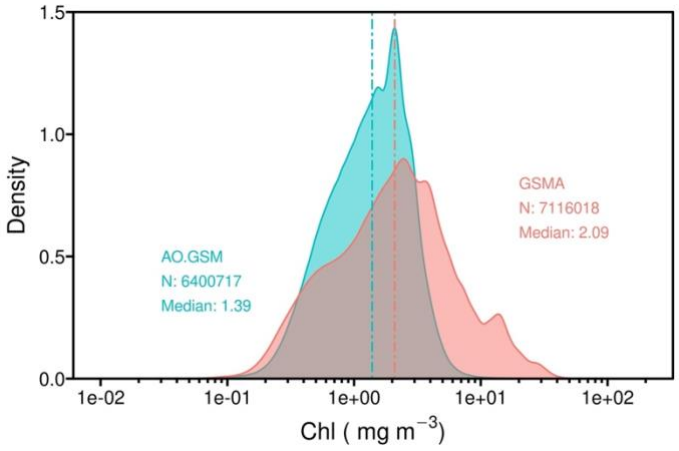

Figure 2.6 Kernel density plot of Chl estimates through AO.GSM and GSMA using the OLCI reflectance product taken by Sentinel 3B around the Lena River plume on 10 September 2020.

2.6.3 Application for coastal waters

Given that our major concern is to tune the GSM model for coastal waterbodies, and due to the lack of in *situ* measurements along the Arctic coastal areas, especially in and around large river plumes, the COASTlOOC dataset was introduced to test the applicability of our GSMA model for coastal waterbodies. Results are shown in Figure 2.4(b) and Table 2.4. AO.GSM-generated Chl estimates showed significant underestimation when Chl > 2.0 mg m^{-3} where most of the failures occurred. In addition, the metrics such as MAE (3.19), r^2 (0), slope (0.05) and 61.3% failures demonstrate that AO.GSM was not appropriate for turbid coastal waters. While for GSMA, there was only 4.2% failures. It generated 57% more valid retrievals and improved the accuracy by 93% compared to AO.GSM. Therefore, GSMA showed remarkable superiority over AO.GM for coastal waters. In the absence of other algorithms that can be applied to coastal waters with high accuracy, GSMA might be an alternative to estimate Chl for coastal waters.

2.6.4 Model limitations

The basic principle of the GSM model is to minimize the difference between measured and modeled $R_{rs}(\lambda)$ using non-linear optimization until a predefined convergence threshold is met. Substantially, it is a spectral fitting method. Thus, it is more likely to obtain the optimal solution of Chl when more spectral information is inputted, which is also the motivation of the present study to tune the GSM model by adding 620 nm. However, the most important reason why adding 620 nm works maybe because that signal observed at 620 nm helps better distinguish the absorption of phytoplankton from CDM, and absorption from scattering, which in return would lead to more accurate retrievals. For oceanic waters where CDM level is usually low, the signal at 620 nm is often too weak to differ absorption from scattering, that might be the reason why GSMA performed similarly with AO.GSM for such type of waters. While for coastal waters where CDM level is generally high, signal observed at 620 nm is strong enough to be used by GSMA to better distinguish the role of phytoplankton from CDM, leading to remarkable improvement when compared with AO.GSM.

However, the GSM model itself has some limitations as it adopts several simplified assumptions to limit the number of unknowns. For instance, g_0 and g_1 were used to described oceanic case 1 waters (Gordon et al., 1988). Lee et al. (1999) has found that $g_0 = 0.084$ and $g_1 = 0.17$ work better for higher-scattering coastal waters. In particular, Ψ is held constant to describe the spectral shapes of IOP (Inherent Optical Properties), which actually varies in nature. $a_{ph}^*(\lambda)$ is expressed as a constant mean spectrum, while true phytoplankton absorption spectra vary dramatically due to photoadaptation and/or composition of phytoplankton assemblage (Bricaud et al., 1998). S actually depends on a complex system involving land/sea interactions, the productivity and state of the phytoplankton communities, the microbial loop and photochemistry (Maritorena et al., 2002). Similarly, b_{bp} is modeled using a simple function with a fixed spectral dependence (η), while η varies in the world ocean and such wavelength dependence tends to disappear in turbid waters. Furthermore, GSM is a blue-light-dependent algorithm. That is to say, for extremely eutrophic waters where Chl is high, the blue signal might drop below the limits of detection due to the high absorption of phytoplankton. Then GSM becomes less efficient and even useless. Nevertheless, GSM has been extensively and widely used by oceanographers as it can outperform standard empirical algorithms, such as in the AO (Mustapha et al., 2012; Lewis and Arrigo, 2020).

2.6.5 Conclusion

In the AO, since the currently best semi-analytical algorithm AO.GSM fails too often for waters with high CDM, we further tuned GSM for the AO by adding 620 nm which is useful to better distinguish the absorption of phytoplankton from CDM, and absorption from scattering. In terms of the performance of Chl estimates, our tuned algorithm GSMA performed similarly to AO.GSM for oceanic waters where CDM level is generally low, but showed much more robustness than AO.GSM for waters with high CDM, and the improvement that GSMA has made for coastal waters could reach up to ~93%. Besides, GSMA exhibited remarkable advantage over AO.GSM regarding the performance of $a_{cdm}(443)$ estimates as the improvement was as high as 168%. These findings imply that, in the absence of other algorithms that can be applied to coastal waters with high accuracy, GSMA might be an alternative to retrieve Chl and $a_{cdm}(443)$ simultaneously.

However, we should keep in mind that the success of GSMA depends on the reliable detection of blue signal. When the observed blue signal drops below the limits of detection due to the high absorption of phytoplankton, GSMA becomes less efficient and even useless. Thus, semi-analytical algorithm that does not rely on blue signal (such as fluorescence-based algorithms) is still expected in future research, especially for eutrophic coastal waters.

Chapitre 3 A novel coupled full-spectral chlorophyll *a* algorithm: a fluorescence-based approach

Juan Li, Atsushi Matsuoka, Stanford B. Hooker, Xiaoping Pang, Marcel Babin

3.1 Résumé

Étant donné que les algorithmes standards de couleur de l'océan qui n'exploitent que le spectre visible sont peu performants dans l'océan Arctique (AO) en raison de l'interférence de la matière organique dissoute colorée (CDOM), il est crucial d'inclure des longueurs d'onde plus grandes qui sont moins affectées par la CDOM pour récupérer les propriétés de l'eau, en particulier pour les eaux turbides. Cependant, les algorithmes basés sur la fluorescence qui n'exploitent que la région rouge du spectre ne sont pas non plus appropriés pour les eaux côtières turbides car le signal de fond est difficile à décrire correctement en raison des interactions complexes entre les composants optiques significatifs dans la colonne d'eau. Il semble que les algorithmes qui n'exploitent que la région bleu-vert ou rouge soient problématiques lorsqu'ils sont appliqués à des eaux turbides. Dans ce contexte, nous avons proposé un algorithme full-spectral en couplant le GSMA (version ajustée du GSM pour l'AO) avec le modèle d'émission de fluorescence. Nous avons constaté que notre nouvel algorithme couplé, FGSM, générait 4 à 10 % de données valides en plus par rapport à GSMA, et améliorait la précision des estimations de la Chl, en particulier pour les eaux eutrophes, l'amélioration atteignant jusqu'à 44 %. Les applications satellitaires du FGSM dans le delta de la rivière Lena ont montré des modèles assez différents de ceux dérivés d'un algorithme à réseau de neurone. Cependant, des mesures coincidentes satellite-in *situ* correspondances sont nécessaires à des fins de validation.

3.2 Abstract

Since standard ocean color algorithms exploiting only visible spectrum perform poorly in the Arctic Ocean (AO) due to the interference of colored dissolved organic matter (CDOM), it is crucial to include longer wavelengths which are less affected by CDOM to retrieve water properties especially for turbid waters. However, fluorescence-based algorithms that only exploit the red region of the spectrum are not appropriate for turbid coastal waters as well because the background signal is difficult to described properly due to the complex interactions between optical-significant components in the water column. It seems that algorithms only exploit blue-green or red region are problematic when applied to turbid waters. Within this context, we proposed a full-spectral algorithm by coupling GMSA (tuned version of GSM for the AO) with fluorescence emission model. We found that our new coupled algorithm, FGSM, generated 4%~10% more valid retrievals when compared with GSMA, and improved the accuracy of Chl estimates, especially for for eutrophic waters, the improvement reached up to ~44%. Satellite applications of FGSM at the Lena River Delta showed quite different patterns with that derived from neural network algorithm. However, coincident satellite-in *situ* matchups are needed for validation purposes.

3.3 Introduction

Ocean color remote sensing (OCRS) has been a powerful tool for monitoring ocean phytoplankton at various spatio-temporal scales and has been used extensively and widely by oceanographers, especially in the Arctic Ocean (AO) where in *situ* measurements are scarce due to the harsh environment, logistical difficulties and cost constrains. However, around the runoff of several major rivers and in shallow areas of a huge continental shelf (more than 50% of the area of this ocean), the AO contains large amounts of colored dissolved organic matter (CDOM) (Matsuoka et al., 2014, 2013; Matsuoka et al., 2007), CDOM strongly absorbs towards short wavelengths of the visible spectrum, where it strongly interferes with the phytoplankton signal. Therefore, standard operational ocean color algorithms such as OC4v6 (O'Reilly et al., 2000; O'Reilly et al., 1998), OC3Mv6 (O'Reilly et al., 2000), OC3V (Wang et al., 2013) and OC4Me (Antoine and Morel, 1999) which only exploit blue and green spectral bands, show poor performance when applied to high-CDOM areas of the AO, as multiple studies have suggested (Lewis and Arrigo, 2020; Mustapha et al., 2012). To circumvent this problem, the use of spectral bands in the red and near-infrared spectral regions, which are less affected by CDOM, has been proposed (e.g., Gons et al., 2002). The latter approach performs well only at high chlorophyll a concentrations (Chl) though. Another solution for addressing CDOM-rich waters for the AO is to use the fluorescence of chlorophyll a (Gower and Borstad, 2004).

Since fluorescence spectral bands have been proposed and implemented on few satellite OCRS sensors (see Babin et al., 1996 and Gower et al., 2004, and references therein), algorithms have been proposed and applied (Behrenfeld et al., 2009; Gower et al., 2004; Huot et al., 2005; Morrison and Goodwin, 2010) to interpret satellite-observed Sun-induced chlorophyll a fluorescence (SICF) to retrieve Chl or quantum yield of fluorescence (ϕ, defined as the fraction of absorbed photons re-emitted as fluorescence). These algorithms are generally based on an analytical function describing water-leaving radiance due to fluorescence but with a series of empirical or semi-empirical relationships. By setting the ϕ to some known value, Chl can be estimated through SICF (Behrenfeld et al., 2009; Huot et al., 2005; Sathyendranath et al., 2004).

Fluorescence line height (FLH) has been routinely implemented on MODIS/OLCI to obtain SICF, which has been used to invert Chl by multiple studies (Behrenfeld et al., 2009; Huot et al., 2007, 2005). There are, however, some problems when using FLH algorithm to derive Chl. Firstly, FLH is described as the radiance at fluorescence emission band distinguished from the background elastic signal using a baseline obtained through linear regression between two wavebands around the fluorescence emission band. However, due to the various composition of optical-significant constituents (i.e., seawater, phytoplankton, CDOM and non-algal particles) in the water column, the background radiance spectra in the fluorescence emission wavelengths are not actually spectrally flat and varies in shape, making it difficult to extract the fluorescence signal accurately. This problem is especially acute in highly turbid waters (Gower et al., 1999). Secondly, since FLH contains information both on ϕ and Chl, to obtain information about a given one requires assumptions/measurements of the other one (Behrenfeld et al., 2009; Huot et al., 2005). Therefore, it is difficult to distinguish Chl from ϕ variations to obtain accurate estimates. Usually, ϕ is given a statistic mean value, but in essence, ϕ, described as the ratio of

photons fluoresced by chlorophyll a over the whole fluorescence band to the photons absorbed by all cellular pigments, is related to much more complex processes. It varies over an order of magnitude among various phytoplankton communities with different functional organization of the photosynthetic apparatus, and depends on nutrient and dyrological conditions (Babin et al., 1996). Lastly, some bio-optical models incorporated in FLH were established for case 1 waters. For instance, the attenuation coefficient for upwelling fluorescence radiance was approximated as the sum of water and phytoplankton absorption, which is not valid for waters with high colored detrital matter.

In this study, to circumvent the problems of blue-green algorithms in high-CDOM waters, and the limitations of the FLH approach, we propose a semi-analytical algorithm that covers the whole visible spectrum and includes fluorescence emission in addition to inherent optical properties of optically-significant substances present in seawater. More specifically, we couple GSMA (tuned version for the AO) with a fluorescence-based model. The development of this new algorithm and its validation were carried out using in *situ* optical data from various coastal waters in the AO and elsewhere.

3.4 Data

3.4.1 Bio-optical in *situ* data sets

Data sets used in this study are summarized in Table 3.1. The algorithm-developing data set consists of 8 Arctic cruises: MALINA, ICESCAPE2010, ICESCAPE2011, ARCTICNET2011, ARCTICNET2013, TARA, GREEN EDGE and AREX. Given the similarity in optical properties among coastal waters, the COASTlOOC data set was added into the algorithm-developing data set to compensate the lack of measurements in Arctic coastal areas. The validation data set contributed by SB Hooker covers both high and low latitude waters.

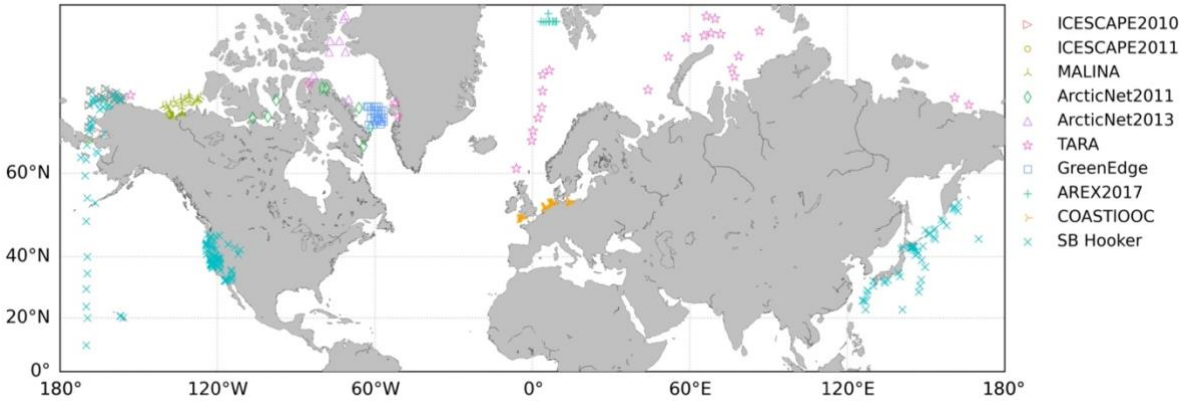

Figure 3.1 Sample locations of various datasets.

Table 3.1 Summary of in *situ* datasets.

Data	Station[a]	Year	Month	Region	Source
MALINA	37	2009	July-August	Southern Beaufort Sea	SeaBASS
ICESCAPE2010	34	2010	June-July	Chukchi and Beaufort Sea	SeaBASS
ICESCAPE2011	3	2011	June-July	Chukchi and Beaufort Sea	SeaBASS
ARCTICNET2011	9	2011	August	Baffin Bay	Individual
ARCTICNET2013	9	2013	August	Baffin Bay	Individual
TARA	27	2013	May-November	Polar circle	SeaBASS
GREEN EDGE	34	2016	June-July	Baffin Bay	Individual
AREX	11	2017	July	Greenland Sea	Individual
COASTlOOC	168	1997-1998	January-December	Europe coastal areas	Individual
SB Hooker	300	2010, 2013-2017	March-December	Global scale	Individual

[a]The number of concurrent measurements of $R_{rs}(\lambda)$ and Chl.

$R_{rs}(\lambda)$ measurements

Except the COASTlOOC data set, all $R_{rs}(\lambda)$ (sr^{-1}) was determined using the Compact-Optical Profiling System (C-OPS, Hooker et al. (2013)). Briefly, in-water upwelling radiance $L_u(\lambda, z)$, in-water downward irradiance $E_d(\lambda, z)$, above-water downward solar irradiance ($E_s(\lambda)$), pressure/depth, and dual axes tilts were measured simultaneously. After normalization by $E_s(\lambda)$ and 5° tilt filtering, $L_u(\lambda, z)$ and $E_d(\lambda, z)$ were extrapolated to subsurface $L_u^{0-}(\lambda)$ and $E_d^{0-}(\lambda)$ through progressively optimized depth interval within the surface layer. Finally,

$R_{rs}(\lambda)$ was calculated as: $R_{rs}(\lambda) = 0.54L_u^{0-}(\lambda)/(E_d^{0-}(\lambda)/0.97)$. Details of the process protocols are documented in Antoine et al. (2013).

As for the COASTlOOC data set, in-water upwelling irradiance $E_u(\lambda, z)$ and downwelling irradiance just above the sea surface $E_d^{0+}(\lambda)$ were measured with a Satlantic free-fall SPMR (SeaWiFS Profiling Multichannel Radiometer) and a SMSR (SeaWiFS Multichannel Surface Reference), respectively (Bélanger et al., 2008). $E_u^{0-}(\lambda)$ was obtained by extrapolating $E_u(\lambda, z)$ to subsurface by fitting a certain exponential function. Then $L_u^{0-}(\lambda)$ was calculated as $L_u^{0-}(\lambda) = E_u^{0-}(\lambda)/3.8$ (Bélanger et al., 2008). Afterwards, $R_{rs}(\lambda)$ was calculated through the same equation described above. Note that, in the present study, only common wavebands (412,443,490,510,555,620,670,683,710 nm) were used.

Chl measurements

Chlorophyll a concentrations were determined via High-Performance Liquid Chromatography (HPLC). Generally, 25 mm GF/F filters were used to collect phytoplankton from seawater samples. Filters were extracted in 100% methanol, disrupted by sonication and clarified by filtration (GF/F Whatman) before being analyzed by HPLC later in the laboratory to obtain separated pigments (Ras et al., 2008; Van Heukelem and Thomas, 2001). Finally, total chlorophyll a pigment concentration was defined as the sum of mono- and divinyl chlorophyll a concentrations, chlorophyllide a and the allomeric and epimeric forms of chlorophyll a (Hooker and Zibordi, 2005; Reynolds et al., 2016).

Absorption measurements

Only the absorption measurements of the algorithm-developing data set were used in the present study. Absorption spectra of particulate $a_p(\lambda)$ (m^{-1}) and non-algal particles $a_{nap}(\lambda)$ (m^{-1}) were determined using a Perkin-Elmer Lambda-19 spectrophotometer equipped with a 15 cm integrating sphere following the methodology described in (Bricaud et al., 2010; Kishino et al., 1985; Stramski et al., 2015). Phytoplankton absorption spectra $a_{ph}(\lambda)$ were calculated by subtracting $a_{nap}(\lambda)$ from $a_p(\lambda)$. $a_{cdom}(\lambda)$ was measured using a liquid core waveguide system, UltraPath following (Miller et al., 2002). Absorption spectra of colored detrital and dissolved material (CDM, $a_{cdm}(\lambda)$, m^{-1}) was calculated as the sum of $a_{cdom}(\lambda)$ and $a_{nap}(\lambda)$. The number of concurrent $a_{cdm}(443)$ along with $R_{rs}(\lambda)$ and Chl is 238.

3.4.2 Satellite image

A Sentinel 3B OLCI (Ocean and Land Colour Instrument) image (file name: S3B_OL_2_WFR____20200910T031808_20200910T032108_20200911T114327_0179_043_175_1620_MAR_O_NT_002.SEN3) with full resolution (~300 m) around the Lena River Delta taken on 10 September 2020 was downloaded from https://catalogue.onda-dias.eu for assessment purpose. $R_{rs}(\lambda)$ was derived from reflectance products by dividing π, which was then used to generate Chl and $a_{cdm}(443)$.

3.5 Methods

3.5.1 FGSM algorithm

A vertically-resolved fluorescence emission model (Huot et al., 2005) is incorporated into the GSMA model to infer the radiative signal observed both in the blue-green and red spectrum. Basically, GSMA is adopted to describe the elastic signal across the whole spectrum, besides, except that at the red wavelengths (670,683,710 nm) where the inelastic signal due to fluorescence is modeled using the semi-analytical fluorescence model. Note that the water-leaving signal due to Raman scattering is neglected as its contribution does not exceed a few percent (Huot et al., 2007; Matsuoka et al., 2017). Briefly, modeled $r_{rs}(\lambda)$ is described using this coupled full-spectral semi-analytical algorithm FGSM. By minimizing the mean square difference between measured and modeled $r_{rs}(\lambda)$, we can retrieve the unknowns.

Table 3.2 Symbols, descriptions and units of variables used in this study.

Model	Symbol	Description	Unit
Inputs	$R_{rs}(\lambda)$	above-surface remote-sensing reflectance	sr^{-1}
	θ_s	solar zenith angle	radians
Outputs	Chl	chlorophyll a concentration	mg m^{-3}
	$a_{cdm}(443)$	absorption coefficient of colored dissolved and detrital material at 443 nm	m^{-1}
	$b_{bp}(443)$	particlulate backscattering coefficient at 443 nm	m^{-1}
	σ	factor that adjusts the fluorescence emission spectrum	unitless
	ϕ	quantum yield of fluorescence	unitless
Variables	$a_w(\lambda)$	absorption coefficient of water at λ nm	m^{-1}
	$a_{ph}(\lambda)$	absorption coefficient of phytoplankton at λ nm	m^{-1}
	$a^*_{ph}(\lambda)$	chlorophyll-specific phytoplankton absorption coefficient at λ nm	m^2 mg Chl^{-1}
	$a^*_{sol}(\lambda)$	chlorophyll-specific absorption coefficient of chlorophyll in solution at λ nm	m^2 mg Chl^{-1}
	$\overline{a^*_{ph}}$	irradiance-weighted chlorophyll-specific absorption coefficient	m^2 mg Chl^{-1}
	$a_{cdm}(\lambda)$	absorption coefficient of colored dissolved and detrital material at λ nm	m^{-1}
	$a_f(\lambda)$	attenuation coefficient of upwelling fluorescence radiance at λ nm	m^{-1}
	$a(\lambda)$	total absorption coefficient at λ nm	m^{-1}
	$Q^*_a(\lambda)$	portion of emitted fluorescence not reabsorbed within the cell at λ nm	unitless
	$b_{bw}(\lambda)$	backscattering coefficient of water at λ nm	m^{-1}
	$b_{bp}(\lambda)$	particulate backscattering coefficient at λ nm	m^{-1}
	$b_b(\lambda)$	total backscattering coefficient at λ nm	m^{-1}
	S	spectral decay constant of $a_{cdm}(\lambda)$ in visible range	nm^{-1}
	η	power-law exponent of $b_{bp}(\lambda)$ in visible range	unitless
	$C_f(\lambda)$	a proportionality factor which converts fluorescence signal at λ nm to the whole fluorescence band	nm
	$K_{abs}(\lambda)$	attenuation coefficient of absorbed radiation at λ nm	m^{-1}
	$K_d(\lambda)$	attenuation coefficient of downwelling irradiance at λ nm	m^{-1}
	$L_w(\lambda)$	upwelling radiance at λ nm	mol $m^{-2}s^{-1}nm^{-1}sr^{-1}$
	$L_{wN}(\lambda)$	normalized upwelling radiance at λ nm	mol $m^{-2}s^{-1}nm^{-1}sr^{-1}$
	$L_{wf}(\lambda)$	upwelling fluoresced radiance at λ nm	mol $m^{-2}s^{-1}nm^{-1}sr^{-1}$
	$E_d(\lambda)$	downwelling irradiance at λ nm	mol $m^{-2}s^{-1}nm^{-1}$
	$F_0(\lambda)$	solar irradiance at λ nm at top of atmosphere	mol $m^{-2}s^{-1}nm^{-1}$
	$\dot{E}_{PAR}$	irradiance in the photosynthetically available radiation waveband	mol $m^{-2}s^{-1}nm^{-1}$
	FLH	fluorescence line height	mol $m^{-2}s^{-1}nm^{-1}sr^{-1}$

Generally, $r_{rs}(\lambda)$ due to elastic scattering is described as:

$$r^E_{rs}(\lambda) = g_0 \frac{b_b(\lambda)}{a(\lambda)+b_b(\lambda)} + g_1\left(\frac{b_b(\lambda)}{a(\lambda)+b_b(\lambda)}\right)^2 \quad (14)$$

Where $g_0 = 0.089$ and $g_1 = 0.1245$ (Lee et al., 2002). Absorption and backscattering spectra can be expanded as:

$$a(\lambda) = a_w(\lambda) + \text{Chl}\, a^*_{ph}(\lambda) + a_{cdm}(443)e^{-S(\lambda-443)} \quad (15)$$

$$b_b(\lambda) = b_{bw}(\lambda) + b_{bp}(443)(\lambda/443)^{-\eta} \quad (16)$$

Seawater absorption spectra ($a_w(\lambda)$) and backscattering spectra $b_{bw}(\lambda)$ are assumed to be known constants (Morel, 1974; Pope and Fry, 1997). $a^*_{ph}(\lambda)$ is the chlorophyll-specific absorption coefficient. Values at 412, 443, 490, 510, 555, 620, and 670 were inherited from GSMA (Li et al., in preparation), while as for $a^*_{ph}(683{,}710)$, measured median values 0.0188 and 0.0013 m^2mg Chl^{-1} were adopted, respectively. a_{cdm} is the absorption coefficient of colored detrital material (CDM), and b_{bp} is the particulate backscattering coefficient. S is the spectral decay constant for $a_{cdm}(\lambda)$ (Bricaud et al., 1981; Green and Blough, 1994), and η is the power-law exponent for $b_{bp}(\lambda)$. They were both inherited from GSMA, and the values used were 0.0196 nm^{-1} and 1.0316 for S and η separately.

In the fluorescence emission wavelengths (670, 683, 710), $r_{rs}(\lambda_{fluo})$ is expressed as the sum of the elastic signal ($r^E_{rs}(\lambda_{fluo})$) and the inelastic signal ($r^F_{rs}(\lambda_{fluo})$) due to fluorescence emission:

$$r_{rs}(\lambda_{fluo}) = r^E_{rs}(\lambda_{fluo}) + r^F_{rs}(\lambda_{fluo}) \quad (17)$$

Where $r^F_{rs}(\lambda_{fluo})$ is approximated via the following fluorescence emission model (Huot et al., 2005):

$$r^F_{rs}(\lambda_{fluo}) = \frac{\text{Chl}\,\phi\, Q^*_a(\lambda_{fluo})\,\overline{a^*_{ph}}\,\bar{E}_{PAR}}{4\pi\, c_f(\lambda_{fluo})\,[K_{abs}(\lambda_{fluo}) + a_f(\lambda_{fluo})]\,\bar{E_d}(\lambda_{fluo})} \quad (18)$$

Where ϕ is the quantum yield of fluorescence, which is the 4th unknown besides Chl, $a_{cdm}(443)$ and $b_{bp}(443)$. $Q^*_a(\lambda_{fluo})$ is the fraction of emitted fluorescence not reabsorbed within the cell, which can be expressed as below according to (Morel and Bricaud, 1981):

$$Q^*_a(\lambda_{fluo}) = a^{*\prime}_{ph}(\lambda_{fluo})/a^*_{sol}(\lambda_{fluo}) \quad (19)$$

Where $a^*_{sol}(\lambda_{fluo})$ is the chlorophyll a specific absorption coefficient in solution. $a^*_{sol}(\lambda_{fluo})$ were taken as 0.0207, 0.0120 and 0.0003 $mg^{-1}m^2$, at 670, 683, and 710 nm, respectively, because mostly chlorophyll a absorbs at these wavelengths (Bidigare et al., 1990). It should be noticed that $a^{*\prime}_{ph}$ used here was not a fixed constant as used in equation (15), thus the symbol $a^{*\prime}_{ph}$ is used to differ from the constant one. Here, $a^{*\prime}_{ph}(\lambda)$ is expressed as:

$$a^{*\prime}_{ph}(\lambda) = a_{ph}(\lambda)/[\text{Chl}] \quad (20)$$

Where $a_{ph}(\lambda)$ was modeled as a function of $a_{ph}(443)$ (see Figure 3.2 and Table 3.3) using the algorithm-developing data sets (see section 3.4.1):

$$a_{ph}(443) = 0.0532\,[\text{Chl}]^{0.769} \quad (21)$$

To make this fluorescence algorithm routinely applicable to satellite data, we introduced $K_d(490)$, a standard ocean color product, to derive $Q^*_a(\lambda_{fluo})$ and $\overline{a^*_{ph}}$ (see description below) like what has been done by Huot et al. (2005). To do so, the relationship between $K_d(490)$ and [Chl] described in Morel and Maritorena (2001) was adopted:

$$K_d(490) = 0.0166 + 0.07242\,[\mathrm{Chl}]^{0.68955} \quad (22)$$

Note that [Chl] (used in equations (20)-(22)) is a temporary intermediate variable aiming to describe $Q_a^*(\lambda_{fluo})$ as a function of $K_d(490)$. That is to say, in the process to determine $Q_a^*(\lambda_{fluo})$, it is not necessary to know the value of [Chl]. Therefore, the symbol [Chl] is used to differ from the retrieval Chl. Finally, by solving equations (19)-(22), $Q_a^*(\lambda_{fluo})$ is expressed as a function as $K_d(490)$:

$$Q_a^*(670) = 0.0136(K_d(490) - 0.0166)^{-0.2174}/0.0207 \quad (23)$$

$$Q_a^*(683) = 0.0117(K_d(490) - 0.0166)^{-0.2008}/0.0120 \quad (24)$$

$$Q_a^*(710) = 0.0011(K_d(490) - 0.0166)^{-0.1088}/0.0003 \quad (25)$$

Note that, due to residual absorption by accessory pigments or some technical errors, Q_a^* might exceed 1 (Babin et al., 1996). Thus, a theoretical upper limit 1 is assigned to Q_a^*.

$\overline{a_{ph}^*}$ is the irradiance-weighted chlorophyll-specific absorption coefficient, which can be approximated as a function of $K_d(490)$ as well (Huot et al., 2005):

$$\overline{a_{ph}^*} = 0.00663(K_d(490) - 0.016)^{-0.3611} \quad (26)$$

$\dot{E}_{PAR}^-$ is the irradiance in the photosynthetically available radiation wavebands from 400 to 700 nm, and $E_d^-(\lambda)$ is the downwelling irradiance just below sea surface at λ nm. In the present study, HydroLight is used to generate a comprehensive data set of $\dot{E}_{PAR}^-$ and $E_d^-(\lambda)$ covering wide range of absorption and backscattering spectral following the procedure described at https://www.ioccg.org/groups/lee_data.pdf. The ratio of $\dot{E}_{PAR}^-$ to $E_d^-(\lambda_{fluo})$ is then summarized in Table 3.4. It can be seen that the variances are quite small (< 2.3). Therefore, $\dot{E}_{PAR}^-/E_d^-(\lambda_{fluo})$ was assumed as constant using the mean value listed in the table.

$C_f(\lambda_{fluo})$ is a proportionality factor which converts fluorescence signal at λ_{fluo} to the whole fluorescence emission spectrum:

$$C_f(\lambda_{fluo}) = \int_{-\infty}^{\infty} F(\lambda) d\lambda / F(\lambda_{fluo}) \quad (27)$$

Where $F(\lambda)$ is the fluorescence emission spectrum. In this study, the fluorescence emission spectrum of *Thallassiosira pseudonana spp.* expressed as the sum of two gaussian curves (Huot, 2004) with a factor σ determining the magnitude of the main peak is adopted:

$$F(\lambda) = 67.5\,\sigma\, e^{\frac{-(\lambda-682.8)^2}{2\sigma^2}} + 98.55\, e^{\frac{-(\lambda-721.5)^2}{233.3^2}} \quad (28)$$

Thus, the fifth unknown σ is introduced.

$K_{abs}(\lambda_{fluo})$ is the attenuation coefficient of absorbed irradiance, which is simply approximated by $K_d(\lambda_{fluo})$ which can be obtained according to Lee et al. (2013):

$$K_d(\lambda) = (1 + 0.005\,\theta_s)\,a(\lambda) + 4.259(1 - 0.265\,\frac{b_{bw}(\lambda)}{b_b(\lambda)})(1 - 0.52\,e^{-10.8\,a(\lambda)})b_b(\lambda) \quad (29)$$

Where θ_s is the solar zenith angle, $a(\lambda)$ and $b_b(\lambda)$ are generated through QAAv6, which are different from those used in equations (14)-(16).

$a_f(\lambda_{fluo})$ is the attenuation coefficient of upwelling fluorescence radiance, which is expressed as:

$$a_f(\lambda_{fluo}) = a(\lambda_{fluo}) + b_b(\lambda_{fluo}) \quad (30)$$

Overall, remote-sensing reflectance can be modeled using the approach described above with five unknowns (Chl, $a_{cdm}(443)$, $b_{bp}(443)$, ϕ and σ). To differ from the measured remote-sensing reflectance $Mr_{rs}(\lambda)$, the estimated value is noted as $Er_{rs}(\lambda)$ hereafter. By matching $Er_{rs}(\lambda)$ with $Mr_{rs}(\lambda)$ using the cost function described below we can estimate the five unknowns.

$$\text{CF} = sum(Mr_{rs}(\lambda) - Er_{rs}(\lambda))^2 \quad (31)$$

However, given the small magnitude of fluorescence, for eutrophic waters, the signals observed in the red needs to be amplified to put more weights on the fluorescence signals. For this purpose, when $R_{rs}(\lambda_{green}) > \max\{R_{rs}(\lambda_{blue}), R_{rs}(\lambda_{nir})\}$, water-leaving signals in the red were multiplied by am amplification factor described as $\text{AF} = max\{R_{rs}(\lambda_{green})\}/R_{rs}(683)$. The cost function is thus then:

$$\text{CF} = sum(Mr_{rs}(\lambda_{vis}) - Er_{rs}(\lambda_{vis}))^2 + sum(\text{AF} * (Mr_{rs}(\lambda_{fluo}) - Er_{rs}(\lambda_{fluo})))^2 \quad (32)$$

For convenience, this GSMA and fluorescence coupled model is named as FGSM from hereafter. An illustrative flowchart is shown in Figure 3.4.

Table 3.3 Coefficients of the nonlinear regression expressed as $a_{ph}(\lambda) = A(\lambda)[a_{ph}(443)]^{B(\lambda)}$, where λ is the wavelength, r^2 is the determination coefficient of the regression.

λ (nm)	$A(\lambda)$	$B(\lambda)$	r^2
412	1.011	1.032	0.978
443	1.0	1.0	1.0
490	0.581	0.983	0.990
510	0.443	1.025	0.984
555	0.267	1.134	0.949
620	0.285	1.162	0.973
670	0.620	1.106	0.972
683	0.531	1.121	0.967
710	0.051	1.203	0.853

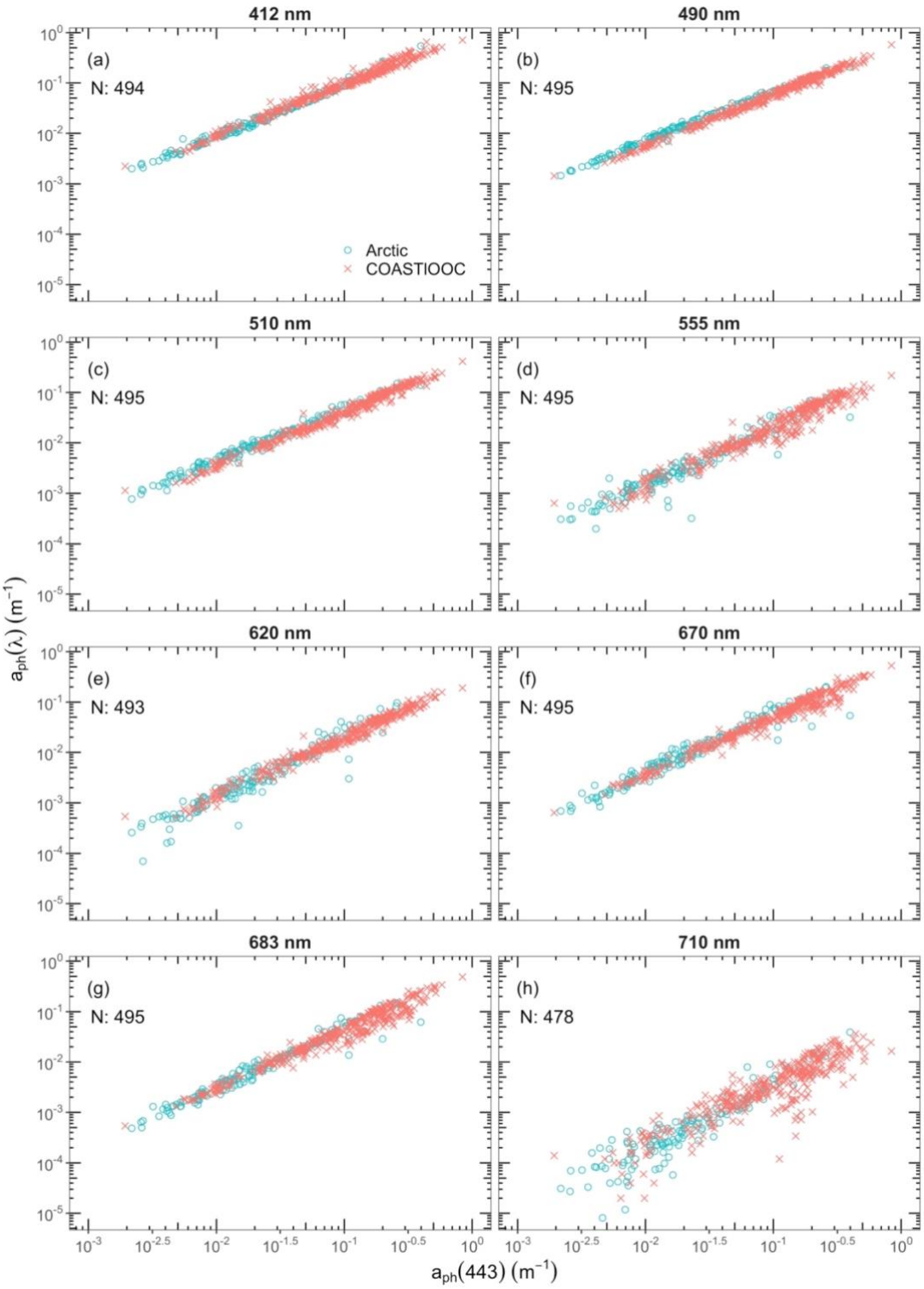

Figure 3.2 Relationships between $a_{ph}(\lambda)$ at 412, 490, 510, 555, 620, 670, 683, 710 nm and $a_{ph}(443)$, respectively.

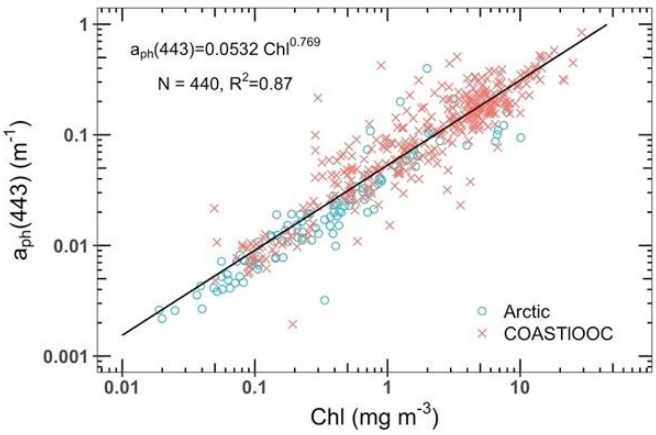

Figure 3.3 Relationship between $a_{ph}(443)$ and Chl.

Table 3.4 Summary of the variation of EWF.

Wavelength	Min	Max	Mean	Median	Variance
670	257.97	266.92	260.39	260.31	0.439
683	267.49	279.20	271.59	271.74	1.233
710	270.40	284.47	275.98	276.35	2.288

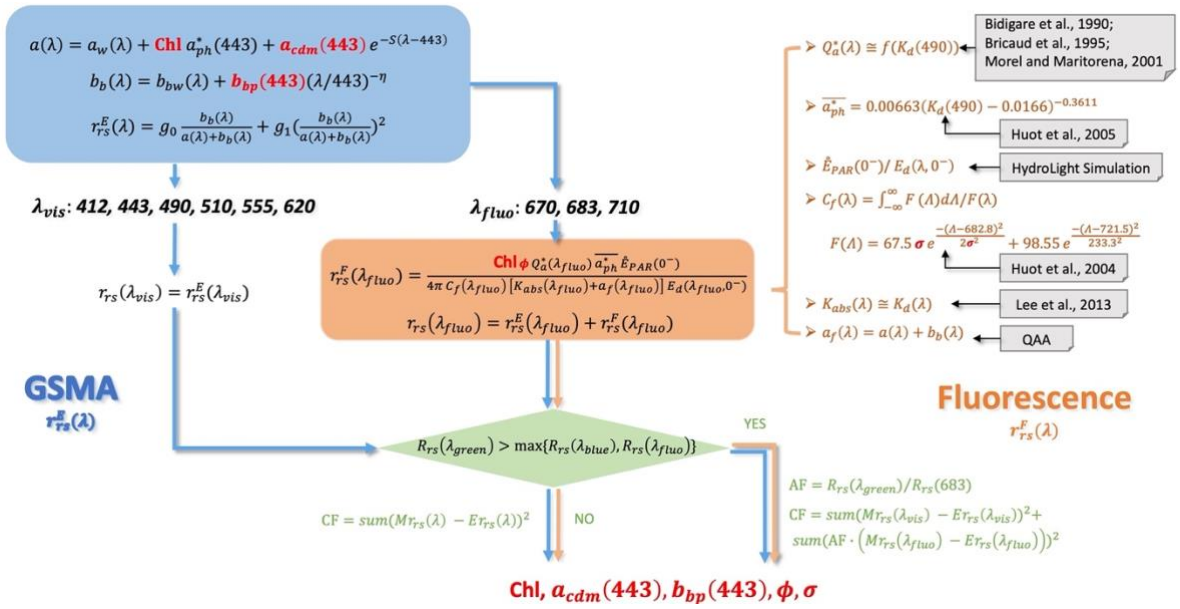

Figure 3.4 Flowchart of FGSM algorithm. Briefly, GSMA was used to describe the elastic signal in the whole spectrum. While in the red region, except the elastic signal, the fluorescence emission model was adopted to express the fluorescence signal. In addition, for waters where blue signal is relative low, more weights were put on the fluorescence signal. Finally, the five unknows including Chl were obtained by spectral-fitting optimization.

3.5.2 FLH algorithm

FLH algorithm makes use of the fluorescence emitted by phytoplankton in the red to retrieve chlorophyll a concentration. Generally, the sensor-observed fluorescence line height (FLH) is calculated as:

$$\mathrm{FLH}(683) = L_{wN}(683) - \frac{27}{40}L_{wN}(670) - \frac{13}{40}L_{wN}(710) \quad (33)$$

Where L_{wN} is normalized water-leaving radiance, which can be described as:

$$L_{wN}(\lambda) = F_0(\lambda)\frac{L_w(\lambda)}{E_d^+(\lambda)} = F_0(\lambda)R_{rs}(\lambda) \quad (34)$$

$F_0(\lambda)$ is 1516.040, 1464.849, and 1401.801 mol m^{-2} s^{-1} nm^{-1} at 670, 683 and 710 nm, respectively. Then, upwelling fluoresced radiance just above sea surface is calculated as:

$$L_{wf}^+ = \mathrm{FLH}(683)E_d^+(683)/F_0(683) \quad (35)$$

Transmitting L_{wf}^+ across the sea-air surface, we can obtain the upwelling fluoresced radiance just below sea surface:

$$L_{wf}^- = \frac{FLH(683)E_d^-(683)}{0.54\times0.97F_0(683)} \quad (36)$$

By integrating fluorescence signal over depth with several simplification between attenuation coefficient and optical properties, we can approximate the total amount of fluorescence radiance at the surface (Huot et al., 2005):

$$L_{wf}^- = \frac{Chl\ \phi\ Q_a^*(683)\ \overline{a_{ph}^*}\ \dot{E}_{PAR}^-}{4\pi\ C_f(683)[K_{abs}(683)+a_f(683)]} \quad (37)$$

Combining equation (36) and (37):

$$\frac{Chl\ \phi\ Q_a^*(683)\ \overline{a_{ph}^*}\ \dot{E}_{PAR}^-}{4\pi\ C_f(683)[K_{abs}(683)+a_f(683)]} = \frac{\mathrm{FLH}(683)E_d^-(683)}{0.54\times0.97F_0(683)} \quad (38)$$

$K_{abs}(683)$, $a_f(683)$, $Q_a^*(683)$, $\overline{a_{ph}^*}$, $\dot{E}_{PAR}^-/E_d^-(683)$ are used as the values described in section 3.5.1, $C_f(685)$ is taken as 43.38 nm (Huot et al., 2005). Therefore, if we know Chl, we can get ϕ, and vice versa. In order to obtain Chl, firstly, Chl estimated through empirical algorithm OC4v6 (Chl_{oc4}, O'Reilly et al. (2000)) is substituted into equation (38) to derive ϕ, then the mean ϕ (ϕ_{mean}) is substituted back into equation (38) to get the final Chl estimates.

3.5.3 Evaluation metrics

Algorithm performance was assessed following the metrics described in Seegers et al. (2018), that is, the number of effective retrievals, bias and mean absolute error (MAE) and percent wins through pair-wise comparison.

$$\mathrm{bias} = 10^{\mathrm{mean}(log10(X^M)-log10(X^E))} \quad (39)$$

$$\mathrm{MAE} = 10^{\mathrm{mean}|log10(X^M)-log10(X^E)|} \quad (40)$$

Where X stands for Chl or $a_{cdm}(443)$. Besides, slope and coefficient of determination (r^2) for log-transformed variable via type II reduced major axis (RMA) regression (Legendre, 1998) are also adopted as complementary metrics.

3.5.4 Classification

Based on measured median value of Chl (1.21 mg m^{-3}), we split the in *situ* data set by half. For the part with Chl $\leq$ 1.21 mg m^{-3}, samples with $a_{cdm}(443) \leq 0.118$ m^{-1} were classified as chl.acdm, the others with $a_{cdm}(443) > 0.118$ m^{-1} were regarded as chl.ACDM. The same procedure was applied to the other part of the data set with Chl > 1.21 mg m^{-3}, therefore we got CHL.acdm and CHL.ACDM. The illustration of the classification approach is summarized in Table 3.5.

Table 3.5 Classification criteria.

Water type	Threshold	Number
chl.acdm	Chl ≤ 1.21 mg m^{-3}, $a_{cdm}(443) \leq 0.118$ m^{-1}	136
CHL.acdm	Chl > 1.21 mg m^{-3}, $a_{cdm}(443) \leq 0.118$ m^{-1}	30
chl.ACDM	Chl ≤ 1.21 mg m^{-3}, $a_{cdm}(443) > 0.118$ m^{-1}	30
CHL.ACDM	Chl > 1.21 mg m^{-3}, $a_{cdm}(443) > 0.118$ m^{-1}	136

3.6 Results and discussions

3.6.1 Performance of FGSM

The FGSM model was applied to the 332 reflectance spectra with corresponding sun zenith angle from the Arctic and COASTlOOC data sets to retrieve Chl, $a_{cdm}(443)$, $b_{bp}(443)$, ϕ and σ. For comparison purposes, Chl estimates derived through the Arctic empirical algorithm AO.emp (Lewis and Arrigo, 2020), FLH algorithm, the Arctic semi-analytical algorithm GSMA (described in chapter 3) are also showed in Figure 3.5. Symbols representing FLH-derived Chls are the most scattered around the 1:1 regression line, while FGSM-derived Chls are the most evenly distributed along the 1:1 regression line. AO.emp performed the best in water type CHL.acdm but worst in chl.ACDM. It seems that this empirical algorithm is not able to provide good performance for all waters with very different optical properties. For water types chl.acdm and CHL.acdm, except FLH, there is no significant difference between the performance of the other algorithms. In water type CHL.ACDM, AO.emp and GSMA showed obvious underestimation, FLH exhibited a notable trend of overestimation, and FGSM-derived Chls were the least biased. Different levels of overestimation occurred in chl.ACDM were the common problem of all algorithms.

Given GSMA is currently the best semi-analytical algorithm for the Arctic Ocean, it was further compared with our new coupled algorithm FGSM pair by pair (see Figure 3.6(a)). For water type chl.acdm and CHL.acdm, there is no significant difference between GSMA- and FGSM-derived Chls. FGSM produced 2 and 11 more valid Chl estimates than GSMA in chl.ACDM and CHL.ACDM, respectively, although some of them were located far from the 1:1 regression line. In addition, diamonds and ‘x’ symbols representing Chl estimates in CHL.ACDM using FGSM, they were much more concentrated along the 1:1 regression than estimates derived from GSMA. This pair-wise comparison demonstrated that FGSM outperformed GSMA for waters with high levels of both Chl and CDM.

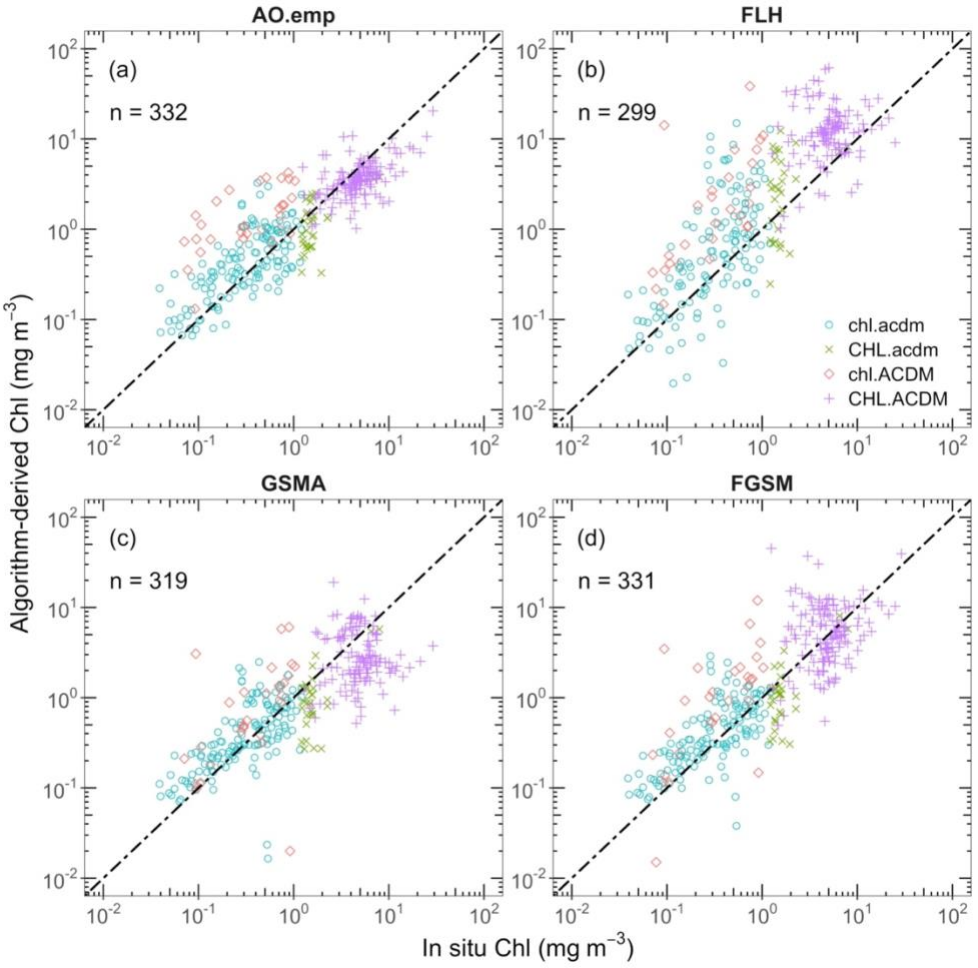

Figure 3.5 Comparison between measured and estimated Chl in 4 water types - chl.acdm, CHL.acdm, chl.ACDM, and CHL.ACDM (see context for definition) using (a) AO.emp, (b) FLH, (c) GSMA, and (d) FGSM algorithms.

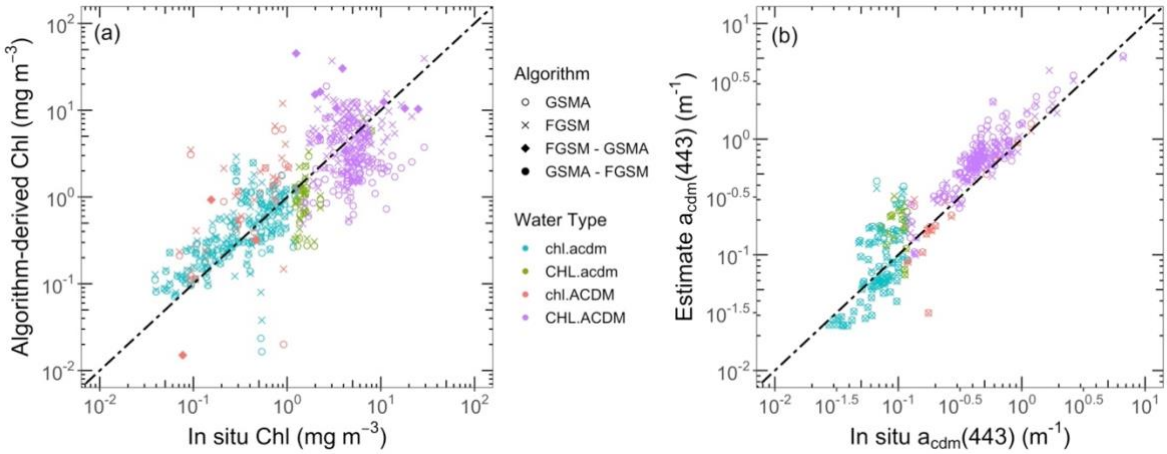

Figure 3.6 Comparison of (a) Chl and (b) $a_{cdm}(443)$ estimates, from GSMA and FGSM for 4 water types. "FGSM-GSMA" represents the Chl estimates derived using FGSM but failed using GSMA, while "GSMA-FGSM" refers to the opposite.

Performance metrics of each algorithm are listed in Table 3.6 and Table 3.7. Generally, AO.emp, FLH and FGSM overestimated Chl by 10%, 114% and 17%, respectively. While GSMA showed 14% underestimation. AO.emp had the lowest MAE but highest r^2, and it was the only algorithm with no failure. As for decision metric wins (Table 3.6), AO.emp outperformed the other algorithms through pair-wise comparison, ranking the first among all algorithms tested. FLH had the highest MAE (2.77) and most failures accounting for 10.9% of the total samples. Its wins did not exceed 30% when compared to the other algorithm, indicating it was the worst chlorophyll a algorithm tested. FGSM showed better results than GSMA in terms of MAE, failures, r^2 and slope. While their wins were quite close. To look closer, further analysis between GSMA and FGSM was carried out with respect to water type. For oligotrophic waters (in this study referred as Chl < 1.21 mg m^{-3}), GSMA won 67.6% for chl.acdm and 83.3% for chl.ACDM. However, we noticed that, for water type chl.acdm, there was no significant difference between Chl estimates derived from GSMA and FGSM concerning bias, MAE, r^2 and slope. For water type chl.ACDM, even though FGSM obtained larger bias and MAE, its overall MAE (1.95) was smaller than GSMA, indicating that the inferiority of FGSM in chl.ACDM was overcome by the winners in other water types. As for eutrophic waters, FGSM showed overwhelming superiority over GSMA as all the metrics listed in Table 3.7 suggested.

$a_{cdm}(443)$ is another common retrieval of GSMA and FGSM models. Comparisons between measured and estimated $a_{cdm}(443)$ using GSMA and FGSM were carried out as well. As seen from Figure 3.6(b), there is no obvious difference between GSMA- and FGSM-derived $a_{cdm}(443)$. Metrics (i.e., bias, MAE, wins, r^2 and $slope$) showed in Table 3.7 demonstrate that FGSM worked slightly better than GSMA. Combined with the improvement FGSM had made in the estimation of Chl especially for eutrophic waters, FGSM overtook GSMA as the best semi-analytical algorithm retrieving Chl and $a_{cdm}(443)$ simultaneously for the Arctic Ocean.

Table 3.6 Chlorophyll *a* algorithm performance assessed through pair-wise comparison.

Data	Algorithm	Percent Wins			
		AO.emp	FLH	GSMA	FGSM
Arctic + COASTlOOC	AO.emp	-	29.2	43.1	48.8
	FLH	70.8	-	71.7	73.8
	GSMA	56.9	26.5	-	47.6
	FGSM	51.2	26.2	52.4	-
	Overall Wins	59.6	27.3	55.7	56.7
	Failure		33 (10.0%)	13 (3.9%)	1 (0.3%)
SB Hooker	AO.emp	-	33.3	53.7	58
	FLH	65.3	-	62	70.7
	GSMA	44.7	30	-	51.3
	FGSM	42	29.3	48.3	-
	Overall Wins	50.7	30.9	54.7	60
	Failure	5 (1.7%)	72 (24.0%)	33 (11.0%)	3 (1.0%)

Table 3.7 Metrics comparing algorithm performance.

Data	Algorithm	n	bias	MAE	Overall Wins (%)	Failure	r^2	slope
Arctic + COASTlOOC n = 332	AO.emp	332	1.10	1.83	59.6		0.73	0.80
	FLH	299	2.14	2.77	27.3	33 (10.9%)	0.67	1.19
	GSMA	319	0.86	2.06	55.7	13 (4.3%)	0.61	0.78
	FGSM	331	1.17	1.95	56.7	1 (0.3%)	0.70	0.94
	chl.acdm, n = 136							
	GSMA	136	1.22	1.72	67.6		0.42	0.87
	FGSM	136	1.29	1.73	32.4		0.46	0.90
	CHL.acdm, n = 30							
	GSMA	30	0.57	1.89	40.0		0.36	1.89
	FGSM	30	0.63	1.79	60.0		0.38	1.86
	chl.ACDM, n = 30							
	GSMA	28	1.86	2.53	83.3	2 (6.7%)	0.25	1.10
	FGSM	29	2.55	3.24	16.7	1 (3.3%)	0.44	1.26
	CHL.ACDM, n = 136							
	GSMA	125	0.54	2.44	33.1	11 (8.1%)	0.00	8.84
	FGSM	136	1.02	2.00	66.9		0.05	1.37
	acdm(443), n = 238							
	GSMA	232	1.31	1.53	42.7	6 (2.5%)	0.86	1.18
	FGSM	232	1.25	1.48	57.3	6 (2.5%)	0.86	1.15
SB Hooker n = 300	AO.emp	295	0.87	2.25	50.7	5 (1.7%)	0.70	1.04
	FLH	228	1.72	2.69	30.9	72 (24.0%)	0.58	1.34
	GSMA	267	0.90	2.03	54.7	33 (11.0%)	0.66	0.95
	FGSM	297	1.12	2.15	60.0	3 (1.0%)	0.66	1.02

In addition, another independent global data set contributed by SB Hooker was adopted to validate FGSM with respect to robustness. For comparison, results generated from AO.emp, FLH and GSMA are also showed in Figure 3.7. AO.emp showed obvious overestimation when Chl < 0.2 mg m^{-3} and > 10.0 mg m^{-3}. FLH-derived Chl estimates were the most scattered, distributed along the 1:1 regression line. Same as before, GSMA and FGSM were taken out for pair-wise comparison (see Figure 3.8). When Chl < 0.3 mg m^{-3}, FGSM generated several large Chl estimates located far above the regression, while for Chl > 2.0 mg m^{-3}, GSMA was more likely to produce lower Chl estimates distributed far below the regression line. Besides, FGSM derived 30 more valid Chl estimates as the diamonds showed in Figure 3.8, although some of them were distributed far from the 1:1 regression line. As for statistic metrics, AO.emp generated 2 more failures than FGSM, but the r^2 was the highest among all. Given FLH had 72 failures accounting for 24% of the total samples, it was excluded for

further comparisons. Bias of GSMA was the closest to 1, however, the failures of GSMA reached 11.0%, exhibiting instability in its application to global waters. Regarding FGSM, unlike at the Arctic scale, it surpassed AO.emp and GSMA by pair-wise comparisons, obtaining 60% overall wins, and thus became the best algorithm of all at a global scale.

Overall, FLH performed the worst of all. AO.emp outperformed the other algorithms in the AO, however, its performance degraded when applied to global waters. FGSM improved the accuracy of Chl estimates by ~10% when compared with GSMA, while for eutrophic waters, the improvement reached up to ~44%. In addition, the failures of FGSM did not exceed 1%, which was even less than the empirical algorithm sometimes, indicating its robustness regardless of the complex optical properties in the water column.

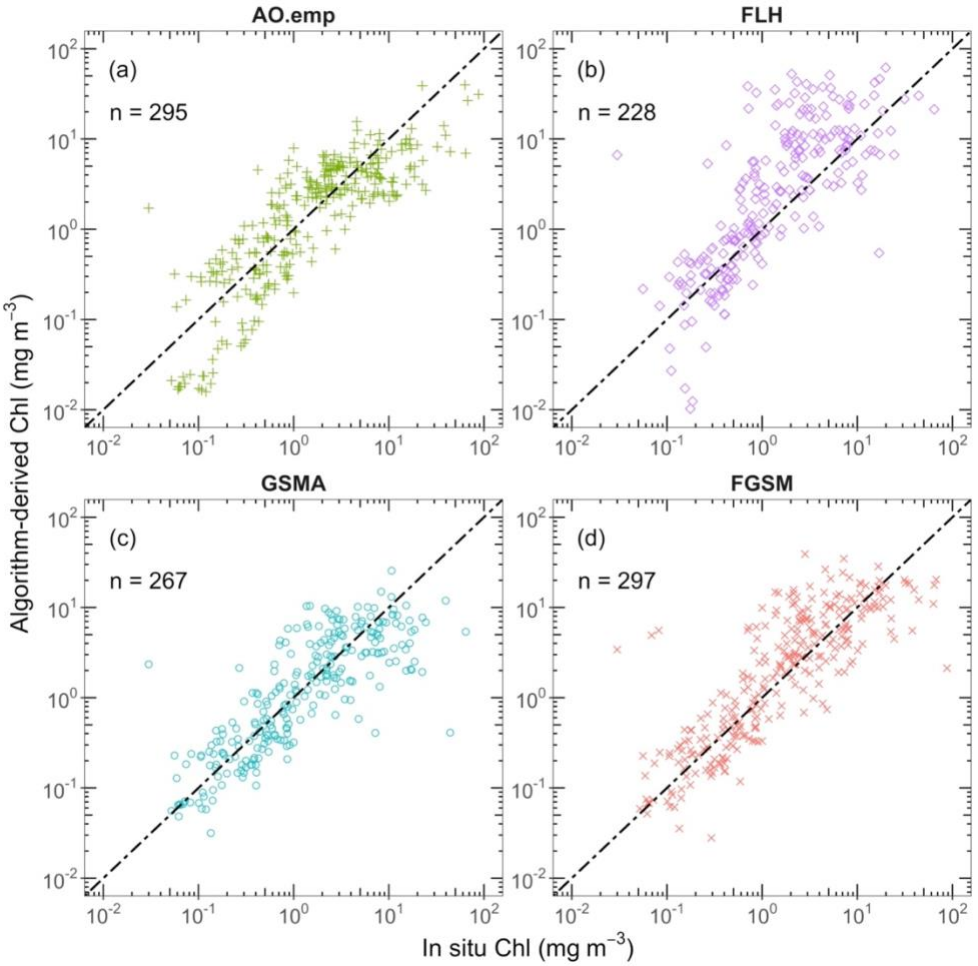

Figure 3.7 Comparison between measured and estimated Chl derived from (a) AO.emp, (b) FLH, (c) GSMA, and (d) FGSM using the dataset contributed by S.B. Hooker.

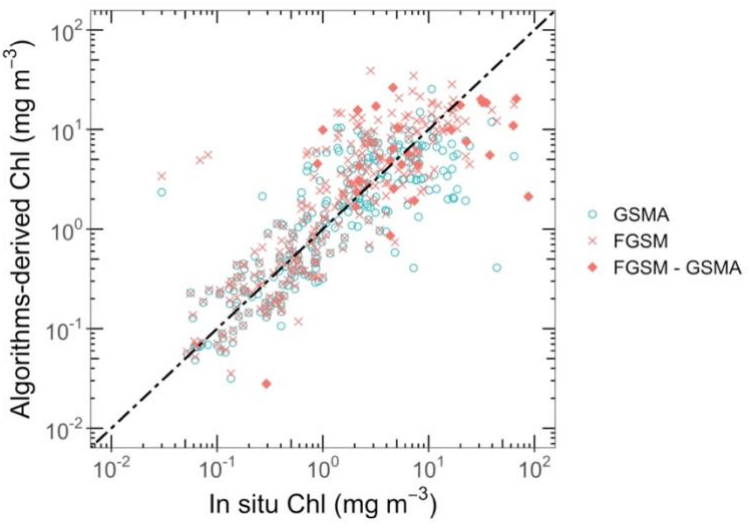

Figure 3.8 Comparison of Chl estimates between GSMA and FGSM. FGSM-GSMA represents the Chl estimates derived using FGSM but using via GSMA.

3.6.2 Satellite application

FGSM and GSMA were applied to the OLCI reflectance product around the Lena River Delta on 10 September 2020 to produce Chl and $a_{cdm}(443)$ estimates (see Figure 3.9 and Figure 3.11). Standard Chl products generated through NN (neural network algorithm) and global algorithm OC4Me (Morel et al., 2007) are also showed for comparison purposes. Seen from Figure 3.9, as the black circle suggested, FGSM had more Chl retrievals along the shelf than GSMA, and the number of valid Chl estimates was compatible with the empirical algorithm OC4Me. Besides more pixels along the coast, FGSM-derived Chl estimates in area 1 and 2 were larger than that obtained from GSMA. NN got the most Chl retrievals, but showed significant differences in area 1, 3, and 4 when compared with the images produced by GSMA and FGSM. As for OC4Me, it generated relative lower Chl estimates in area 1, 2, and 3 than GSMA and FGSM.

For further analysis, kernel density plots of individual algorithm derived Chl products were illustrated in Figure 3.10. Generally, the density curve belonging to GSMA was nearly normally distributed with median value 2.09 mg m^{-3}. Unlike GSMA, the FGSM curve had two visible crests located around the GSMA crest. Because the righter crest lay further to the GSMA crest, the median value of FGSM-derived Chl estimates was slightly higher than that of GSMA. The OC4Me curve seems to be a shift of FGSM curve to the left, but more compactly distributed resulting in higher crests. NN curve also had two crests but located at the farthest ends. Since the left crest was much higher than the right one, NN obtained the smallest median value (0.65 mg m^{-3}). In addition, numbers of Chl estimates were summed up for statistics in terms of Chl level (Table 3.8) according to the classification criteria described in section 3.5.4. NN obtained the most Chl estimates, followed by OC4Me. FGSM indeed had more Chl retrievals for eutrophic waters than GSMA, but the total number was less than that of GSMA. This was because that FGSM adopted reflectance at 710 nm which is more likely to be negative for oligotrophic waters due to the problems of atmospheric correction.

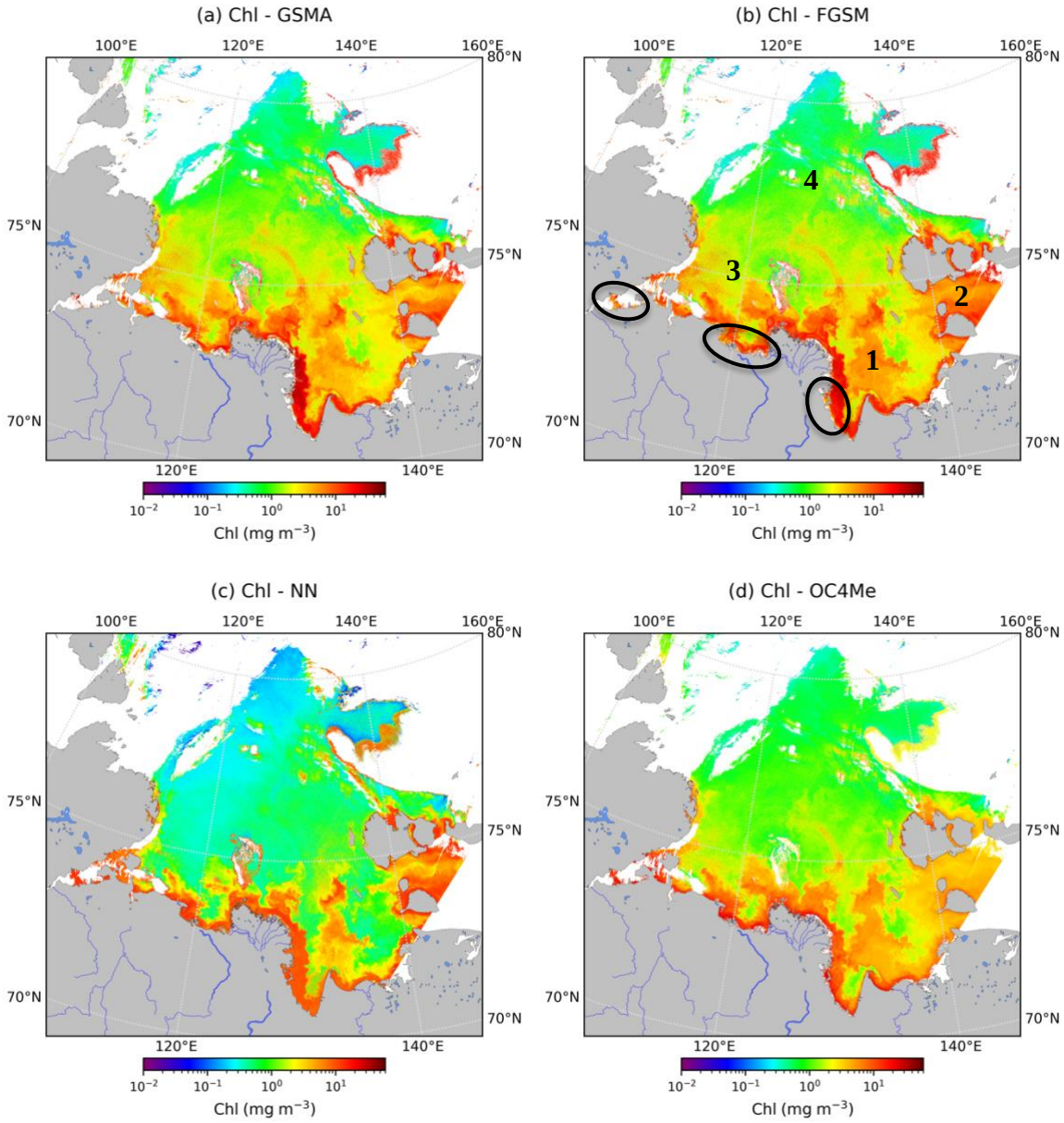

Figure 3.9 (a) GSMA, (b) FGSM, (c) NN and (d) OC4Me derived Chl estimates using the OLCI reflectance product taken by Sentinel 3B around the Lena River plume on 10 September 2020.

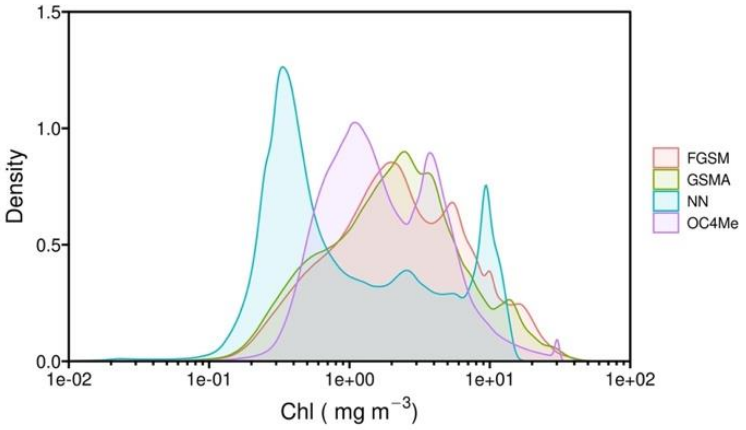

Figure 3.10 Kernel density plot of Chl estimates from GSMA, FGSM and NN using the OLCI reflectance product taken by Sentinel 3B around the Lena River plume on 10 September 2020.

Table 3.8 Statistical outputs of satellite-derived Chl and $a_{cdm}(443)$ estimates.

	Chl (mg m^{-3})			$a_{cdm}(443)$ (m^{-1})		
Algorithm	N ($\leq$ 1.21)	N (> 1.21)	Median	N ($\leq$ 0.118)	N (> 0.118)	Median
FGSM	2075178	4840813	2.16	4629815	2244335	0.058
GSMA	2282003	4834015	2.09	4919912	2284771	0.058
NN	4693371	2992636	0.65	4169165	3531814	0.097
OC4Me	2914266	4384852	1.55	-	-	-

As for $a_{cdm}(443)$ products, because no empirical algorithm is available, only GSMA, FGSM and NN derived $a_{cdm}(443)$ products are showed in Figure 3.11. No matter from the images or the density plots, there was no significant difference between GSMA- and FGSM-derived values. While NN tended to generate less $a_{cdm}(443)$ retrievals at the range from 0.02 to 0.08 m^{-1} but more values larger than 0.3 m^{-1}, leading to a higher median value than that of GSMA and FGSM.

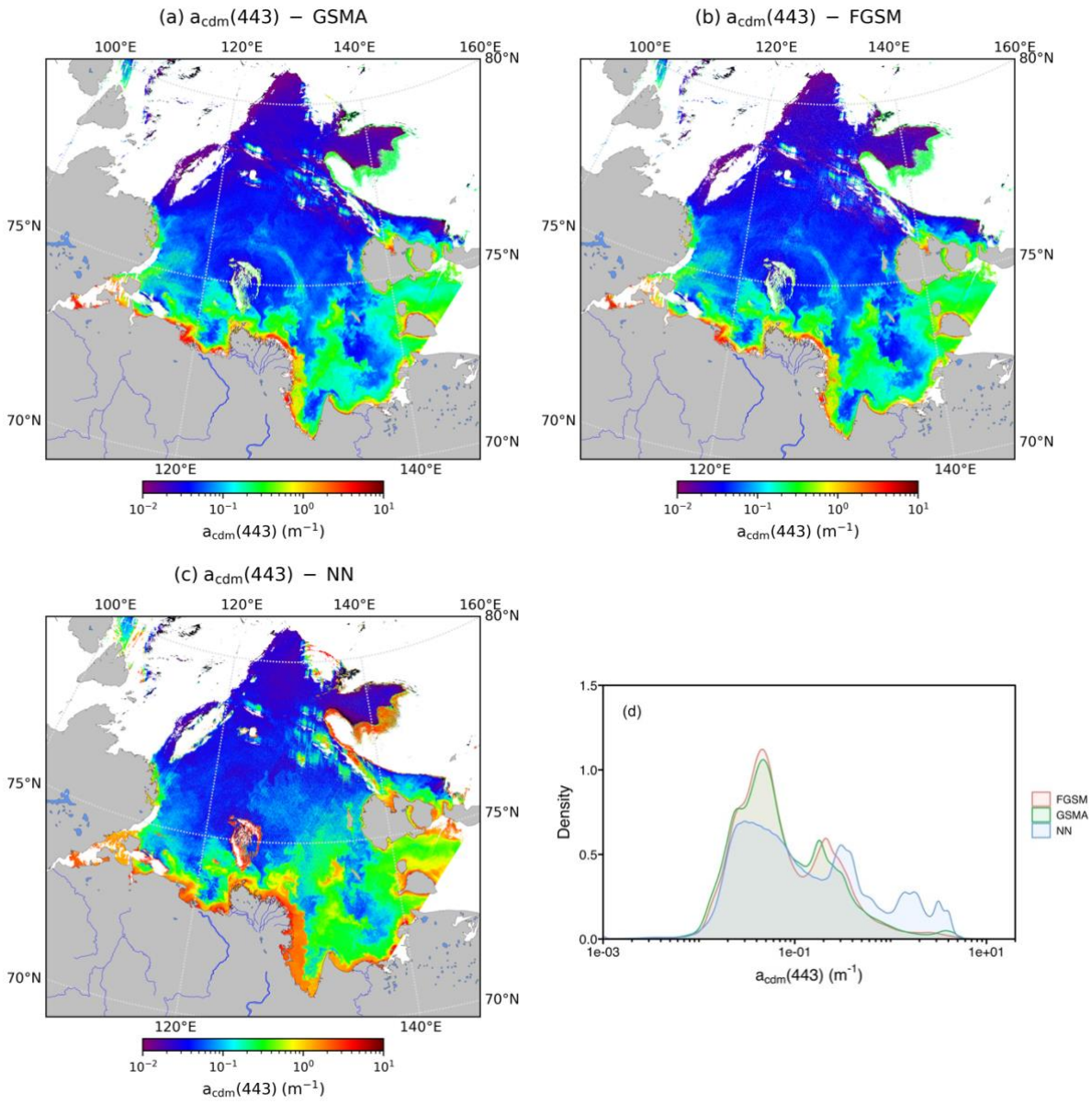

Figure 3.11 (a) GSMA, (b) FGSM, and (c) NN derived $a_{cdm}(443)$ estimates using the OLCI reflectance product taken by Sentinel 3B around the Lena River plume on 10 September 2020. (d) Corresponding kernel density plot of $a_{cdm}(443)$ estimates by individual algorithm.

3.6.3 Model limitations

The basic principle of the FGSM model is to search for optimal solutions for designed retrievals by matching the modeled reflectance spectrum to the measured one. The addition of 2 more bands in the red region will help to shape the reflectance spectrum, which will in return lead to better results. However, due to the complexity of SICF driven by variables such as phytoplankton biomass, ambient light, phytoplankton physiological state, 2 more unknowns are introduced to the FGSM model. Consequently, the problem to be solved becomes much

more complex and time-consuming. To obtain optimal results at minimal cost, for oligotrophic waters, it is not necessary to use FGSM as GSMA can produce better results quickly. Only eutrophic waters such as coastal waters are worth using FGSM.

Since FGSM incorporates a series of simplified assumptions during the inversion process, we should keep in mind that the model itself has some limitations. Firstly, FGSM inherits the limitations from GSMA as it is deployed to describe the elastic signal. That is, a_{ph}^{*}, S, and η are held constant to describe the spectral shapes of IOP (Inherent Optical Properties), which actually vary in nature (Lee and others, 2006; Maritorena et al., 2002). Besides, the limitations of the fluorescence model are also passed into the FGSM model: 1) In reality, $Q_a^{*}(\lambda_{nir})$ variations depend on the intracellular pigment concentration and cell diameter (Morel et al., 2007; Roesler and Boss, 2008). Besides these factors, the variance of $\overline{a_{ph}^{*}}$ also relies on pigment composition and environment factors such as light and nutrient (Babin et al., 2008, 1996). However, $Q_a^{*}(\lambda_{nir})$ and $\overline{a_{ph}^{*}}$ are finally approximated via $K_d(490)$ (equation (19)-(22)) using multiple intermediate variables (Huot et al., 2005). The uncertainty in OCRS-derived K_d is 7~26% (Lee et al., 2013), but how it will bias $Q_a^{*}(\lambda_{nir})$ and $\overline{a_{ph}^{*}}$ is not known yet. 2) Fluorescence emission spectral adopted in FGSM was simulated using σ controlling the magnitude by two gaussian curves with a main peak centered at 682.8 nm and a secondary shoulder at 721.5 nm. In nature, the fluorescence peaks shift between various species. The secondary peak may even shift to the left of the main peak, such as *Storeatula major* (MacIntyre et al., 2010). 3) K_{abs}, describing the fraction of fluorescence signal reabsorbed by phytoplankton, is related to cellular pigment composition and pigment packaging (Bidigare et al., 1990; Bricaud et al., 2004; Ciotti et al., 2002). However, it was simply approximately by K_d. In addition, a_f describing the attenuation of fluorescence in the upwelling process was obtained through QAA-derived absorption and backscattering coefficients. Errors occurring in QAA will pass into a_f as well. 4) The fluorescence emission model only accounts for fluorescence emitted by the most significant pigment chlorophyll a. Furthermore, except the uncertainties caused by the usage of model parameters, since it is solved by optimization, retrievals might interfere with each other. For instance, effects caused by ϕ and σ on the modeling of fluorescence signal probably cancel each other out. In other words, different combination of ϕ and σ might give the same fluorescence signal, as a result, it is hard to distinguish from each other to obtain accurate retrievals.

Although there are multiple limitations, FGSM indeed makes improvement in the estimation of Chl, especially for eutrophic waters. For oligotrophic waters, sensor-observed water-leaving reflectance in the red region are usually quite small, which is difficult to detected accurately. Under such circumstance, simulating the elastic and fluorescence signals separately in FGSM inevitably generated more uncertainties than GSMA which only accounts for elastic signal. This might be the reason why FGMS did not outperform GSMA for this type of water. For eutrophic waters, the fluorescence signal emitted at the red wavelengths is much more sensitive to the variance of Chl than that detected through maximum blue-to-green ratios at the short wavelengths, thus playing an important role in the observed reflectance. Therefore, the introduction of fluorescence to GSMA would help to improve the performance of Chl estimates.

3.6.4 Conclusion

In the AO, due to the existence of high proportion of CDOM which will interfere the phytoplankton signal in short wavelengths, it is critical to include longer wavelengths to retrieve optical properties especially for CDOM-rich waters. Therefore, to obtain better results in the estimation of Chl, fluorescence model was introduced to describe the signal observed in the red region along with the GSMA model. By coupling GSMA with the fluorescence emission model, FGSM has made a range of improvements: 1) The model could work for waters from oligotrophic to very turbid; 2) bio-optical properties of phytoplankton in the whole spectrum were accounted; 3) background radiance at the red wavelengths was modeled using GSMA-related IOPs rather than assumed spectrally flat; 4) the role of σ was switched from parameters to retrieval as Chl, relieving the dependence on each other; 5) parameters (e.g., a_{ph}^{*}, S, η) used in the fluorescence model has been optimized for the AO by GSMA; 6) The bio-optical model used to derive a_f for case 1 waters in the fluorescence model have been adapted for case 2 waters; 7) Chl, common retrieval of both models, is more likely to invert accurately under the dual constrains from both models than using a single model; 8) the inversion scheme can derive information on phytoplankton physiological state (e.g., ϕ). Although the uncertainty is unknown, to some extent, it will help for the better understanding of phytoplankton dynamics due to climate changes.

No matter applied to the algorithm-developing or validation data set, in terms of the estimation of Chl, AO.emp showed obvious underestimations when Chl > 10.0 mg m^{-3}, while FLH manifested a trend of overestimation when Chl > 1.0 mg m^{-3}. As for GSMA and FGSM, FGSM generated more than 4% valid retrievals than GSMA, and the accuracy of FGSM-derived Chl estimates improved ~10% when compared with GSMA. Besides, FGSM showed obvious superiority over GSMA for eutrophic waters, the improvement reached up to 44%. With respect to the performance of $a_{cdm}(443)$, FGSM outperformed GSMA, but with limited improvement within 5%.

Satellite application based on OLCI reflectance in the Lena River Delta further confirmed that FGSM tends to generate much more valid Chl retrievals in coastal areas. However, in the open ocean, probably due to the impact of atmospheric correction, satellite-observed surface reflectance at 710 nm is more likely to be negative which will lead to more blank pixels by FGSM. Therefore, it is GSMA that is more efficient and robust for oceanic waters. Given the complexity and time-consuming nature of FGSM, we should keep in mind that only eutrophic coastal waterbodies are worth using it. In addition, NN-derived Chl and $a_{cdm}(443)$ showed a quite different pattern when compared with FGSM. Thus, matchups are badly needed for validation purposes in the future.

Conclusion and perspectives

The main purpose of this thesis was to improvement the accuracy of algorithm-derived Chl for the AO, especially for productive CDOM-rich and turbid coastal waters. We aimed to overcome the main interference on phytoplankton signal caused by the high proportion of CDM in the water column. To achieve this goal, we have thoroughly evaluated operational ocean color algorithms and typical Arctic algorithms from the perspective of the impact of CDM, tuned GSM for the Arctic Ocean, and developed a full-spectral algorithm accounting the phytoplankton fluorescence signal for dark absorbing waters. However, more can be done to further improve the performance, such as considering phytoplankton function type (PFT), developing machine learning or neural network approaches, etc. Moreover, there is still a number of problems that need to be addressed in terms of remote sensing of phytoplankton in the AO, such as the persistence of clouds, sea ice contamination, SCM (subsurface chlorophyll maximum), ice-edge and under-ice bloom. Hence, in this conclusion part, general recommendations about the use of chlorophyll a algorithms in the AO are given. Then we propose directions for future research with regard to remote sensing of phytoplankton in the AO.

General recommendations

Given the advantages and disadvantages of the 3 types of ocean color algorithms (summarized in Table 0.4), here are several suggestions for application in the AO.

- At regional scale, we can always believe empirical algorithms designed for waters under study, but the use of empirical algorithm for the entire AO should be avoided due to the heterogeneous optical properties in the AO.
- It is recommended to use semi-analytical models which allow discrimination and quantification of the roles of non-phytoplankton constituents to the optical properties of seawater for the AO. For CDOM-rich turbid coastal waters, FGSM should be the first choice, while for oceanic waters, GSMA seems to be a better choice for the reason that it performs similarly to FGSM but with much lower computational cost. Under the circumstance of rapidly and widely changing Arctic, the monitoring of marine ecosystems, especially phytoplankton dynamics, is a long-term activity which needs more attention and thus require more effort.
- The C2RCC processor (operational neural network algorithm for OLCI) inverts satellite-observed top of atmosphere water-leaving reflectance spectrum directly to retrieve water constituents or its optical properties based on radiative transfer theory. Inside the processor, atmospheric correction and the retrieval of IOPs are trained by a series of neural nets. In the near future, an Arctic version of C2RCC is expected. To achieve this objective, neural nets accounting for the spectral characteristics (central wavelengths, bandwidth and spectral response function) of ocean color sensors (e.g., SeaWiFS, MODIS, VIIRS, MERIS, OLCI) can be directly adopted, while other neural nets need to be retrained by the Arctic boundary conditions (e.g., atmospheric conditions, sea state, sun and viewing geometries,

etc) and specific bio-optical properties (e.g., higher package effect, CDOM-dominated, etc) using HydroLight simulations.

- In *situ* data is of significant importance as they do provide the most accurate data used for calibration and validation of airborne and satellite observations, development and improvement of algorithms, and acquire information not accessible from space. However, there is discrepancy between variables measured from different approaches, which might bias the predictions from algorithm and confound the parameterization/interpretation of these algorithms. For example, in the harsh Arctic, much of the older and historical data only consists fluoremetrically-derived Chl (notes as FChl hereafter), which showed significant discrepancy compared to HPLC-derived Chl. Mustapha et al. (2012) noted that in the southeastern Beaufort Sea, FChl were often about two times greater than Chl determined on the same sample. Such degree of discrepancy in the determination of pigment estimates might lead to non-negligible uncertainties in ocean color algorithms (e.g., OC4L, AO.emp, AO.GSM) developed utilizing FChl, or combination of pigment estimates from both approaches. Therefore, it is recommended to use HPLC-derived Chl in terms of algorithm evaluation, tuning and development. This not only gives more accurate results, but also facilitates comparison with other relevant studies.
- As sea ice continues to decrease in the AO, ice-edge and under-ice blooms are frequently observed (Ardyna et al., 2020; Perrette et al., 2010). As a result, the MIZ (marginal ice zones) becomes more and more important with regard to marine biology and primary production. To improve data coverage and data quality, new approaches need to be developed to address the problems arising from sea ice contamination. Besides, data gaps due to the prevalence of clouds in the AO also need to be filled by data fusion between multiple sensors and in *situ* autonomous systems to keep the continuity of satellite data, thus providing long-term monitoring the marine ecosystem in the AO.
- The main purpose of developing ocean color algorithms is to use satellite data to obtain synoptic observations of the oceans. However, most evaluation of ocean color algorithms are currently based on in *situ* measurements. Hence, in *situ* and satellite observed matchups are urgently needed for validation purposes in terms of Chl and primary production estimates.

Perspectives and challenges

In addition to the achievable objectives mentioned above in a short term, there are still several challenges of phytoplankton remote sensing in the Arctic which requires long-term persistent exploration and research, such as the detection of SCM and under-ice bloom, and interpretation of PFT.

Subsurface Chlorophyll Maximum

In the AO, a SCM is frequently observed (Ardyna et al., 2013; Brown et al., 2015; Martin et al., 2010). The large export of freshwater due to river discharge, precipitation, and melt of sea ice and glaciers, produces a pronounced haline stratification within the surface layer. A SCM is often associated with this vertical

stratification in post-bloom conditions, and its vertical position is regarded as a compromise between nutrient limitation near the surface and light limitation at depth (Martin et al., 2010). That is, after spring bloom in the upper euphotic zone which depletes the low initial inventories of nitrate in the surface mixed layer, a transient SCM community replaces the fast-growing bloomers once nutrients are exhausted from the surface (Pommier et al., 2009), and the vertical position reported to be driven mainly by a shortage of inorganic nitrogen in the upper euphotic zone, usually locates below the pycnocline in close association with the nitracline (Martin et al., 2010).

Due to the intrinsic biogeochemical processes and complex optical properties in the AO, the statistical relationships between Chl(0^-) and Chl(z) (chlorophyll concentration at depth) developed for lower latitudes (Morel and Berthon, 1989) are problematic when applied to the AO (Martin et al., 2010). For instance, Chl might be overestimated by 2 to 3 folds at neritic stations due to the exclusion of turbid waters with limited euphotic depth in these regressions. For oceanic stratified waters with a pronounced SCM, Chl could be underestimated by a factor of 3 to 5 (Martin et al., 2010).

Different from lower latitude waters, Arctic SCM are more pronounced and thrive higher in the euphotic zone (3 to 10% light level), and often corresponds to a maximum in particulate carbon, which will result a maximum in primary production (IOCCG, 2015; Martin et al., 2010). Therefore, as important contributors to water-column productivity, the neglection of SCMs in the AO may lead to significant errors in the estimation of primary production (Ardyna et al., 2013; Hill et al., 2013; Pabi et al., 2008). Arrigo and van Dijken (2011) has reported that errors in pan-Arctic NPP increase from 0.2% in January to 16% in July due to omission of the SCMs. Later, Ardyna et al. (2013) accounted for the vertical structure of Chl in PP estimations based on empirical statistic relationships. However, remote sensing detectable Chl(z) is still expected.

A solution might be the combination of active and passive remote sensors. Hill and Zimmerman (2010) has proven that active sensors such as LIDAR (Light Detection and Ranging), can, in combination with passive ocean color, dramatically improve our ability to estimate PP for the Arctic. When the vertical distribution of Chl was determined to a resolution of 1 m using modeled LIDAR retrievals of the beam attenuation coefficient, the accuracy of PP estimates improved within a factor of 2–3 compared with measured values.

Ice-edge and under-ice bloom

Receding ice-edges have long been recognized as high biological production sites (Arrigo et al., 2014; Mundy et al., 2009; Perrette et al., 2010). After winter mixing, sea ice retreats, breaking up and letting light into the dark reaches of the AO. This process triggers phytoplankton blooms that readily deplete nutrients in the upper mixed layer along the marginal ice zone (MIZ). Ice-edge bloom, referred as the peak in Chl immediately found after the sea-ice retreat, have been reported in many locations in the Arctic and sub-Arctic marine regions, such as the Bering Sea (Alexander and Niebauer, 1981; Niebauer et al., 1995), Chukchi and Beaufort Seas (Gradinger, 2009; Hill et al., 2005; Mundy et al., 2009), Canadian Archipelago (Tremblay et al., 2006), Baffin Bay (Burgers et al., 2020; Randelhoff et al., 2019), Hudson Bay (Barbedo et al., 2020), Barents Sea (Hegseth

and Sundfjord, 2008), and Laptev Sea (Janout et al., 2016). Ice-edge blooms are significant features of Arctic primary production (Perrette et al., 2010), and show substantial spatial and inter-annual variability (Barbedo et al., 2020).

In addition, thinning sea ice (transition from multi-year ice type to first-year ice), reducing snow cover, and increasing melt ponds proportion and lead formation have dramatically increased the availability of photosynthetically active radiation (PAR, 400–700 nm) for primary production in the ice-covered upper ocean over recent decades (Katlein et al., 2019; Matthes et al., 2020). Multiple studies have suggested that even small leads, cracks, melt ponds or thin ice without snow can in fact let enough light pass to favor under-ice blooms (e.g., Mundy et al. (2009); Arrigo et al. (2014); Lowry et al. (2014); Assmy et al. (2017)). Even under the light- and nutrient-limited central Arctic sea ice, phytoplankton bloom can be noticed with maximum values reaching up to 1.48 mg m^{-3} (Boles et al., 2020). Due to the heterogeneity in PAR transmission caused by various sea ice features (Katlein et al., 2016, 2014; Matthes et al., 2019) and different environment settings, the Pacific inflow upwelling sector (Arrigo et al., 2014), the Atlantic inflow advective sector (Assmy et al., 2017), outflow shelves (Mundy et al., 2014) and the central Arctic (Boles et al., 2020) showed different patterns of under-ice blooms in terms of biomass, community composition and phytoplankton phenology (Ardyna et al., 2020).

The detection of ice-edge blooms may be problematic due to sea ice contamination. And the near ubiquitous under-ice blooms cannot be observed through OCRS. Besides, the impact of under-ice blooms on pan-Arctic estimates of seasonal and annual primary production remains unknown. Furthermore, our understanding of under-ice blooms in the rapidly changing Arctic environment is based on limited observations at specific locations. Additional multi-scale and multi-perspective long-term monitorings are needed to study the ecology and environmental forcing of the under-ice blooms, as well as their regional peculiarities (e.g., occurrence, magnitude, and assemblages). For these purposes, multidisciplinary approaches, i.e., combining expeditions with modern autonomous technologies (e.g., AUVs (Autonomous Underwater Vehicles; Laney et al. (2017); Boles et al. (2020)), BGC-Argo floats (Mayot et al., 2018; Randelhoff et al., 2019), WARM (Warming and Irradiance Measurements; Hill et al. (2018)), ROVs (remotely operated vehicles; Bowen et al. (2014); McFarland et al. (2015))), satellite (e.g., active and passive sensors, aircraft), and modeling analyses, could be powerful tools to provide an overview of phytoplankton blooms under various conditions (i.e., pelagic, ice-edge, under-ice blooms), and help figuring out how they may play an increasingly important role in future marine Arctic biogeochemical cycles (Ardyna et al., 2020).

Peculiar phytoplankton photosynthetic parameters

In the AO, photosynthetic parameters P_B^{max} (maximum rate of carbon fixation at saturating irradiance, mgC mgChl^{-1} h^{-1}) and E_k (light saturation parameter, μmol photon $m^{-2}s^{-1}$) are generally lower than those from lower latitudes (Babin et al., 2015) mostly because of the low irradiance and low seawater temperatures in the Arctic. These associated bio-optical and photosynthetic parameters must be accounted for in PP models. But only a few authors (e.g., Arrigo et al. (2008); Bélanger et al. (2013b)) have tried to do so. Besides, the consideration of phytoplankton functional types (PFTs) which represent dominant taxonomic groups of the

phytoplankton community can help to improve the estimation of phytoplankton biomass, PP, and the transfer of carbon to upper trophic layers or the benthos (Sathyendranath and others, 2014). However, only a few local algorithms have been developed for the AO to detect PFTs from OCRS (e.g., Fujiwara et al. (2014)). Therefore, sensors with higher spectral range and resolution are expected in the future to discriminate the spectral shapes of individual seawater constituents, thus leading to better understanding of the bio-optical properties of the water column. In addition, the use of bio-optical sensors on a variety of autonomous in *situ* platforms (e.g., gliders, floats, ice-tethered moorings; see Figure 4.1) needs to be increased to enhance our observational capabilities and provide more detailed and comprehensive information for better understanding the unique Arctic marine ecosystem (IOCCG, 2015).

All in all, the Arctic Ocean still has much to be studied over the long term to unravel its mysteries.

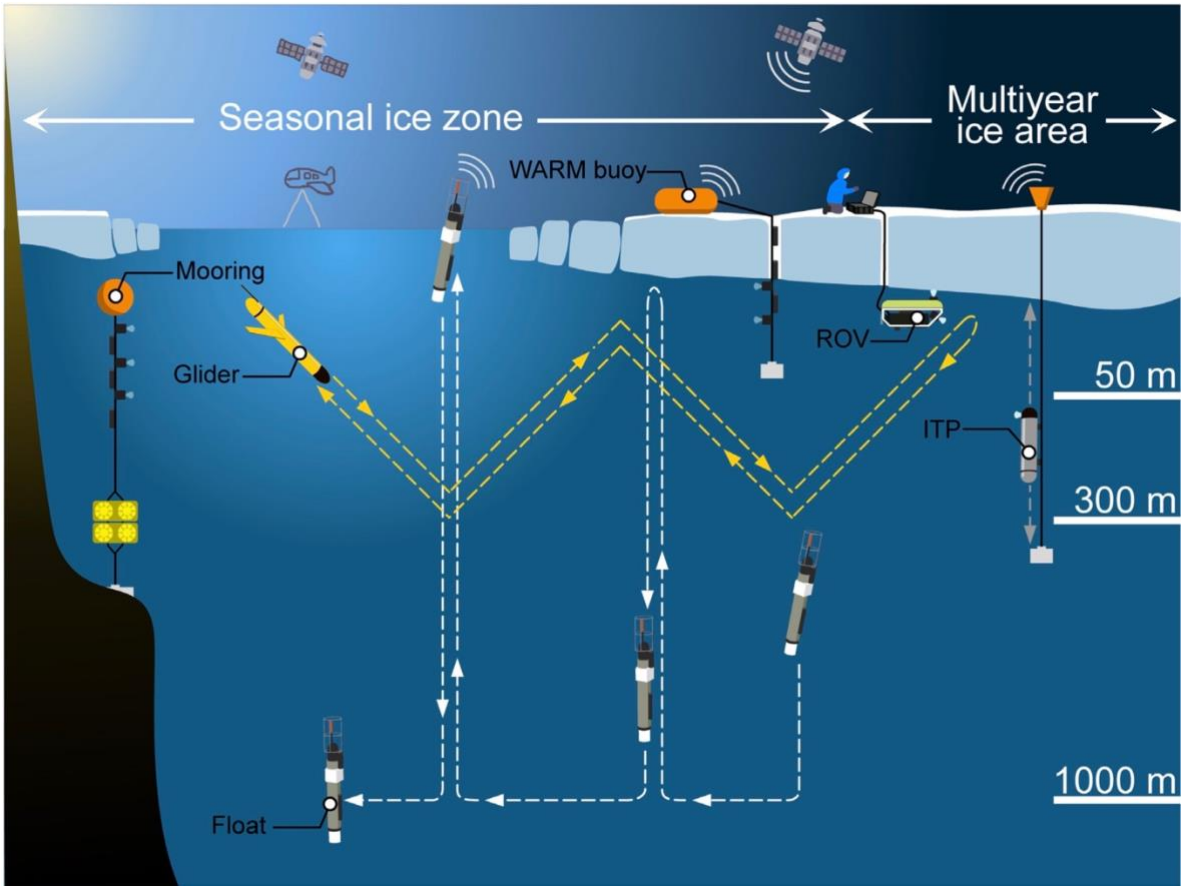

Figure 4.1 Schematic illustration of various above-water and in-water observing systems in the Arctic Ocean. Slightly modified from (Ardyna et al., 2020).

Bibliographie

Alexander, V., Niebauer, H., 1981. Oceanography of the eastern Bering Sea ice-edge zone in spring 1. Limnology and Oceanography 26, 1111–1125. https://doi.org/10.4319/lo.1981.26.6.1111

AMAP, 2017. Snow, water, ice and permafrost in the Arctic (SWIPA) 2017.

Antoine, D., Hooker, S., Bélanger, S., Matsuoka, A., Babin, M., 2013. Apparent optical properties of the Canadian Beaufort Sea 1: Observational overview and water column relationships. Biogeosciences (Online) 10, 4493–4509. https://doi.org/10.5194/bg-10-4493-2013

Antoine, D., Morel, A., 1999. A multiple scattering algorithm for atmospheric correction of remotely sensed ocean colour (MERIS instrument): Principle and implementation for atmospheres carrying various aerosols including absorbing ones. International Journal of Remote Sensing 20, 1875–1916. https://doi.org/10.1080/014311699212533

Ardyna, M., Arrigo, K.R., 2020. Phytoplankton dynamics in a changing arctic ocean. Nature Climate Change 10, 892–903. https://doi.org/10.1038/s41558-020-0905-y

Ardyna, M., Babin, M., Gosselin, M., Devred, E., Bélanger, S., Matsuoka, A., Tremblay, J.-É., 2013. Parameterization of vertical chlorophyll a in the Arctic Ocean: Impact of the subsurface chlorophyll maximum on regional, seasonal, and annual primary production estimates. Biogeosciences (Online) 10, 4383–4404. https://doi.org/10.5194/bg-10-4383-2013

Ardyna, M., Babin, M., Gosselin, M., Devred, E., Rainville, L., Tremblay, J.-É., 2014. Recent Arctic Ocean sea ice loss triggers novel fall phytoplankton blooms. Geophysical Research Letters 41, 6207–6212. https://doi.org/10.1002/2014GL061047

Ardyna, M., Mundy, C., Mayot, N., Matthes, L.C., Oziel, L., Horvat, C., Leu, E., Assmy, P., Hill, V., Matrai, P.A., others, 2020. Under-ice phytoplankton blooms: Shedding light on the "invisible" part of Arctic primary production. Frontiers in Marine Science 7, 985. https://doi.org/10.3389/fmars.2020.608

Arrigo, K.R., Perovich, D.K., Pickart, R.S., Brown, Z.W., van Dijken, G.L., Lowry, K.E., Mills, M.M., Palmer, M.A., Balch, W.M., Bates, N.R., others, 2014. Phytoplankton blooms beneath the sea ice in the Chukchi Sea. Deep Sea Research Part II: Topical Studies in Oceanography 105, 1–16. https://doi.org/10.1016/j.dsr2.2014.03.018

Arrigo, K.R., van Dijken, G.L., 2015. Continued increases in Arctic Ocean primary production. Progress in Oceanography, Synthesis of Arctic Research (SOAR) 136, 60–70. https://doi.org/10.1016/j.pocean.2015.05.002

Arrigo, K.R., van Dijken, G.L., 2011. Secular trends in Arctic Ocean net primary production. Journal of Geophysical Research: Oceans 116. https://doi.org/10.1029/2011JC007151

Arrigo, K.R., van Dijken, G., Pabi, S., 2008. Impact of a shrinking Arctic ice cover on marine primary production. Geophysical Research Letters 35, L19603. https://doi.org/10.1029/2008GL035028

Assmy, P., Fernández-Méndez, M., Duarte, P., Meyer, A., Randelhoff, A., Mundy, C.J., Olsen, L.M., Kauko, H.M., Bailey, A., Chierici, M., Cohen, L., Doulgeris, A.P., Ehn, J.K., Fransson, A., Gerland, S., Hop, H., Hudson, S.R., Hughes, N., Itkin, P., Johnsen, G., King, J.A., Koch, B.P., Koenig, Z., Kwasniewski, S., Laney, S.R., Nicolaus, M., Pavlov, A.K., Polashenski, C.M., Provost, C., Rösel, A., Sandbu, M., Spreen, G., Smedsrud, L.H., Sundfjord, A., Taskjelle, T., Tatarek, A., Wiktor, J., Wagner, P.M., Wold, A., Steen, H., Granskog, M.A., 2017. Leads in Arctic pack ice enable early phytoplankton blooms below snow-covered sea ice. Scientific Reports 7, 40850. https://doi.org/10.1038/srep40850

Babin, Marcel, Arrigo, K., Bélanger, S., Forget, M.-H., others, 2015. Ocean colour remote sensing in polar seas. International Ocean Colour Coordinating Group (IOCCG). http://ioccg.org/wp-content/uploads/2015/10/ioccg-report-16.pdf

Babin, M., Bélanger, S., Ellingsen, I., Forest, A., Le Fouest, V., Lacour, T., Ardyna, M., Slagstad, D., 2015. Estimation of primary production in the Arctic Ocean using ocean colour remote sensing and coupled physicalbiological models: Strengths, limitations and how they compare. Progress in Oceanography 139, 197–220. https://doi.org/10.1016/j.pocean.2015.08.008

Babin, M., Morel, A., Gentili, B., 1996. Remote sensing of sea surface Sun-induced chlorophyll fluorescence: Consequences of natural variations in the optical characteristics of phytoplankton and the quantum yield of chlorophyll a fluorescence. International Journal of Remote Sensing 17, 2417–2448. https://doi.org/10.1080/01431169608948781

Babin, M., Roesler, C.S., Cullen, J.J., 2008. Real-time coastal observing systems for marine ecosystem dynamics and harmful algal blooms: Theory, instrumentation and modelling. Unesco.

Babin, M., Stramski, D., Ferrari, G.M., Claustre, H., Bricaud, A., Obolensky, G., Hoepffner, N., 2003. Variations in the light absorption coefficients of phytoplankton, nonalgal particles, and dissolved organic matter in coastal waters around Europe. Journal of Geophysical Research: Oceans 108. https://doi.org/10.1029/2001JC000882

Barbedo, L., Bélanger, S., Tremblay, J.-É., 2020. Climate control of sea-ice edge phytoplankton blooms in the Hudson Bay system. Elementa: Science of the Anthropocene 8. https://doi.org/10.1525/elementa.039

Basu, S., Mackey, K.R., 2018. Phytoplankton as key mediators of the biological carbon pump: Their responses to a changing climate. Sustainability 10, 869. https://doi.org/10.3390/su10030869

Behrenfeld, M.J., Westberry, T.K., Boss, E., O'Malley, R.T., Siegel, D.A., Wiggert, J.D., Franz, B.A., Feldman, G.C., Doney, S.C., Moore, J.K., Dall'Olmo, G., Milligan, A.J., Lima, I., Mahowald, N., 2009. Satellite-Detected Fluorescence Reveals Global Physiology of Ocean Phytoplankton. Biogeosciences 6, 779–794. https://doi.org/10.5194/bg-6-779-2009

Bélanger, S., Babin, M., Larouche, P., 2008. An empirical ocean color algorithm for estimating the contribution of chromophoric dissolved organic matter to total light absorption in optically complex waters. Journal of Geophysical Research 113, C04027. https://doi.org/10.1029/2007JC004436

Bélanger, S., Babin, M., Tremblay, J.-É., 2013a. Increasing cloudiness in Arctic damps the increase in phytoplankton primary production due to sea ice receding. Biogeosciences (Online) 10, 4087–4101. https://doi.org/10.5194/bg-10-4087-2013

Bélanger, S., Cizmeli, S., Ehn, J., Matsuoka, A., Doxaran, D., Hooker, S., Babin, M., 2013b. Light absorption and partitioning in Arctic Ocean surface waters: Impact of multiyear ice melting. Biogeosciences (Online) 10, 6433–6452. https://doi.org/10.5194/bg-10-6433-2013

Bélisle, C.J.P., 1992. Convergence theorems for a class of simulated annealing algorithms on ℝ d. Journal of Applied Probability 29, 885–895. https://doi.org/10.2307/3214721

Bidigare, R.R., Ondrusek, M.E., Morrow, J.H., Kiefer, D.A., 1990. In-vivo absorption properties of algal pigments, in: Ocean Optics x. International Society for Optics and Photonics, pp. 290–302. https://doi.org/10.1117/12.21451

Bliss, A., Anderson, M., 2014. Snowmelt onset over Arctic sea ice from passive microwave satellite data: 1979. The Cryosphere 8, 2089–2100. https://doi.org/10.5194/tc-8-2089-2014

Blix, K., Li, J., Massicotte, P., Matsuoka, A., 2019. Developing a New Machine-Learning Algorithm for Estimating Chlorophyll-a Concentration in Optically Complex Waters: A Case Study for High Northern Latitude Waters by Using Sentinel 3 OLCI. Remote Sensing 11, 2076. https://doi.org/10.3390/rs11182076

Boles, E., Provost, C., Garcon, V., Bertosio, C., Athanase, M., Koenig, Z., Sennéchael, N., 2020. Under-ice phytoplankton blooms in the Central Arctic Ocean: Insights from the first biogeochemical IAOOS platform drift in 2017. Journal of Geophysical Research: Oceans 125, e2019JC015608. https://doi.org/10.1029/2019JC015608

Bowen, A.D., Yoerger, D.R., German, C.C., Kinsey, J.C., Jakuba, M.V., Gomez-Ibanez, D., Taylor, C.L., Machado, C., Howland, J.C., Kaiser, C.L., others, 2014. Design of Nereid-UI: A remotely operated underwater vehicle for oceanographic access under ice, in: 2014 Oceans-St. John's. IEEE; IEEE, pp. 1–6. https://ieeexplore.ieee.org/document/7003125

Bricaud, A., Babin, M., Claustre, H., Ras, J., Tièche, F., 2010. Light absorption properties and absorption budget of Southeast Pacific waters. Journal of Geophysical Research 115, C08009. https://doi.org/10.1029/2009JC005517

Bricaud, A., Babin, M., Morel, A., Claustre, H., 1995. Variability in the chlorophyll-specific absorption coefficients of natural phytoplankton: Analysis and parameterization. Journal of Geophysical Research 100, 13321. https://doi.org/10.1029/95JC00463

Bricaud, A., Claustre, H., Ras, J., Oubelkheir, kadija, 2004. Natural variability of phytoplanktonic absorption in oceanic waters: Influence of the size structure of algal populations. Journal of Geophysical Research 109, C11010. https://doi.org/10.1029/2004JC002419

Bricaud, A., Morel, A., Babin, M., Allali, K., Claustre, H., 1998. Variations of light absorption by suspended particles with chlorophyll a concentration in oceanic (case 1) waters: Analysis and implications for

bio-optical models. Journal of Geophysical Research: Oceans 103, 31033–31044. https://doi.org/10.1029/98JC02712

Bricaud, A., Morel, A., Prieur, L., 1981. Absorption by dissolved organic matter of the sea (yellow substance) in the UV and visible Domains1. Limnology and Oceanography 26, 43–53. https://doi.org/10.4319/lo.1981.26.1.0043

Brockmann, C., Doerffer, R., Peters, M., 2016. Evolution of the C2RCC neural network for Sentinel 2 and 3 for the retrieval of ocean colour products in normal and extreme optically complex waters. Living Planet Symposium 740, 54. https://ui.adsabs.harvard.edu/abs/2016ESASP.740E..54B

Brown, Z.W., Lowry, K.E., Palmer, M.A., van Dijken, G.L., Mills, M.M., Pickart, R.S., Arrigo, K.R., 2015. Characterizing the subsurface chlorophyll a maximum in the Chukchi Sea and Canada Basin. Deep Sea Research Part II: Topical Studies in Oceanography 118, 88–104. https://doi.org/10.1016/j.dsr2.2015.02.010

Burgers, T.M., Tremblay, J.-É., Else, B.G., Papakyriakou, T.N., 2020. Estimates of net community production from multiple approaches surrounding the spring ice-edge bloom in Baffin Bay. Elementa: Science of the Anthropocene 8. https://doi.org/10.1525/elementa.013

Carmack, E.C., Yamamoto-Kawai, M., Haine, T.W., Bacon, S., Bluhm, B.A., Lique, C., Melling, H., Polyakov, I.V., Straneo, F., Timmermans, M.-L., others, 2016. Freshwater and its role in the Arctic Marine System: Sources, disposition, storage, export, and physical and biogeochemical consequences in the Arctic and global oceans. Journal of Geophysical Research: Biogeosciences 121, 675–717. https://doi.org/10.1002/2015JG003140

Chapman, R.L., 2013. Algae: The world's most important "plants"an introduction. Mitigation and Adaptation Strategies for Global Change 18, 5–12. https://doi.org/10.1007/s11027-010-9255-9

Chaves, J.E., Werdell, P.J., Proctor, C.W., Neeley, A.R., Freeman, S.A., Thomas, C.S., Hooker, S.B., 2015. Assessment of ocean color data records from MODIS-Aqua in the western Arctic Ocean. Deep Sea Research Part II: Topical Studies in Oceanography 118, 32–43. https://doi.org/10.1016/j.dsr2.2015.02.011

Church, J.A., Monselesan, D., Gregory, J.M., Marzeion, B., 2013. Evaluating the ability of process based models to project sea-level change. Environmental Research Letters 8, 014051. https://doi.org/10.1088/1748-9326/8/1/014051

Ciotti, A.M., Lewis, M.R., Cullen, J.J., 2002. Assessment of the relationships between dominant cell size in natural phytoplankton communities and the spectral shape of the absorption coefficient. Limnology and Oceanography 47, 404–417. https://doi.org/10.4319/lo.2002.47.2.0404

Cohen, J., Screen, J.A., Furtado, J.C., Barlow, M., Whittleston, D., Coumou, D., Francis, J., Dethloff, K., Entekhabi, D., Overland, J., Jones, J., 2014. Recent Arctic amplification and extreme mid-latitude weather. Nature Geoscience 7, 627–637. https://doi.org/10.1038/ngeo2234

Coleman, H.M., Eggins, B.R., Byrne, J.A., Palmer, F.L., King, E., 2000. Photocatalytic degradation of 17-β-oestradiol on immobilised TiO2. Applied Catalysis B: Environmental 24, L1–L5. https://doi.org/10.1016/S0926-3373(99)00091-0

Comiso, J.C., 2012. Large decadal decline of the Arctic multiyear ice cover. Journal of Climate 25, 1176–1193.

Comiso, J.C., Parkinson, C.L., Gersten, R., Stock, L., 2008. Accelerated decline in the Arctic sea ice cover. Geophysical Research Letters 35, L01703. https://doi.org/10.1029/2007GL031972

Cota, G.F., Harrison, W.G., Platt, T., Sathyendranath, S., 2003. Bio-optical properties of the Labrador Sea. Journal of Geophysical Research 108, 3228. https://doi.org/10.1029/2000JC000597

Cota, G.F., Wang, J., Comiso, J.C., 2004. Transformation of global satellite chlorophyll retrievals with a regionally tuned algorithm. Remote Sensing of Environment 90, 373–377. https://doi.org/10.1016/j.rse.2004.01.005

Crawford, A.D., Krumhardt, K.M., Lovenduski, N.S., van Dijken, G.L., Arrigo, K.R., 2020. Summer High-Wind Events and Phytoplankton Productivity in the Arctic Ocean. Journal of Geophysical Research: Oceans 125, e2020JC016565. https://doi.org/10.1029/2020JC016565

Cullen, J.J., Ciotti, A.M., Davis, R.F., Neale, P.J., 1997. Relationship between near-surface chlorophyll and solar-stimulated fluorescence: Biological effects, in: Ocean Optics XIII. SPIE, pp. 272–277. https://doi.org/10.1117/12.266454

Dall'Olmo, G., Gitelson, A.A., Rundquist, D.C., Leavitt, B., Barrow, T., Holz, J.C., 2005. Assessing the potential of SeaWiFS and MODIS for estimating chlorophyll concentration in turbid productive waters

using red and near-infrared bands. Remote Sensing of Environment 96, 176–187. https://doi.org/10.1016/j.rse.2005.02.007

Darecki, M., Stramski, D., 2004. An evaluation of MODIS and SeaWiFS bio-optical algorithms in the Baltic Sea. Remote Sensing of Environment 89, 326–350. https://doi.org/10.1016/j.rse.2003.10.012

Dittmar, T., Kattner, G., 2003. The biogeochemistry of the river and shelf ecosystem of the Arctic Ocean: A review. Marine Chemistry 83, 103–120. https://doi.org/10.1016/S0304-4203(03)00105-1

Doerffer, R., Schiller, H., 2007. The MERIS Case 2 water algorithm. International Journal of Remote Sensing 28, 517–535. https://doi.org/10.1080/01431160600821127

Doron, M., Babin, M., Mangin, A., Hembise, O., 2007. Estimation of light penetration, and horizontal and vertical visibility in oceanic and coastal waters from surface reflectance. Journal of Geophysical Research: Oceans 112. https://doi.org/10.1029/2006JC004007

Falkowski, P.G., Dubinsky, Z., Wyman, K., 1985. Growth-irradiance relationships in Phytoplankton1: Growth-irradiance relationships. Limnology and Oceanography 30, 311–321. https://doi.org/10.4319/lo.1985.30.2.0311

Falkowski, P.G., Owens, T.G., 1980. Light: TWO STRATEGIES IN MARINE PHYTOPLANKTON. Plant Physiology 66, 592–595. https://doi.org/10.1104/pp.66.4.592

Fan, Y., Li, W., Gatebe, C.K., Jamet, C., Zibordi, G., Schroeder, T., Stamnes, K., 2017. Atmospheric correction over coastal waters using multilayer neural networks. Remote Sensing of Environment 199, 218–240. https://doi.org/10.1016/j.rse.2017.07.016

Fell, F., Babin, M., Ferrari, M., Obolensky, G., 1999. The potential of chlorophyll fluorescence for the space-borne retrieval of phytoplankton in European coastal and open ocean waters, in: IEEE 1999 International Geoscience and Remote Sensing Symposium. IGARSS'99 (Cat. No.99CH36293). pp. 2087–2091 vol.4. https://doi.org/10.1109/IGARSS.1999.775040

Feng, D., Gleason, C.J., Lin, P., Yang, X., Pan, M., Ishitsuka, Y., 2021. Recent changes to Arctic river discharge. Nature Communications 12, 6917. https://doi.org/10.1038/s41467-021-27228-1

Field, C.B., Behrenfeld, M.J., Randerson, J.T., Falkowski, P., 1998. Primary production of the biosphere: Integrating terrestrial and oceanic components. Science 281, 237–240. https://doi.org/10.1126/science.281.5374.237

Fischer, J., Kronfeld, U., 1990. Sun-stimulated chlorophyll fluorescence 1: Influence of oceanic properties. International Journal of Remote Sensing 11, 2125–2147. https://doi.org/10.1080/01431169008955166

Flanner, M.G., Shell, K.M., Barlage, M., Perovich, D.K., Tschudi, M.A., 2011. Radiative forcing and albedo feedback from the Northern Hemisphere cryosphere between 1979 and 2008. Nature Geoscience 4, 151–155. https://doi.org/10.1038/ngeo1062

Frey, K.E., McClelland, J.W., 2009. Impacts of permafrost degradation on arctic river biogeochemistry. Hydrological Processes 23, 169–182. https://doi.org/10.1002/hyp.7196

Fujiwara, A., Hirawake, T., Suzuki, K., Imai, I., Saitoh, S.-I., 2014. Timing of sea ice retreat can alter phytoplankton community structure in the western Arctic Ocean. Biogeosciences (Online) 11, 1705–1716. https://doi.org/10.5194/bg-11-1705-2014

Garver, S.A., Siegel, D.A., 1997. Inherent optical property inversion of ocean color spectra and its biogeochemical interpretation: 1. Time series from the Sargasso Sea. Journal of Geophysical Research: Oceans 102, 18607–18625. https://doi.org/10.1029/96JC03243

Gons, H.J., Rijkeboer, M., Ruddick, K., 2002. A chlorophyll-retrieval algorithm for satellite imagery (Medium Resolution Imaging Spectrometer) of inland and coastal waters. Journal of Plankton Research 24, 947–951. https://doi.org/10.1093/plankt/24.9.947

Gordon, H.R., Brown, O.B., Evans, R.H., Brown, J.W., Smith, R.C., Baker, K.S., Clark, D.K., 1988. A semianalytic radiance model of ocean color. Journal of Geophysical Research 93, 10909. https://doi.org/10.1029/JD093iD09p10909

Gower, J.F., Brown, L., Borstad, G., 2004. Observation of chlorophyll fluorescence in west coast waters of Canada using the MODIS satellite sensor. Canadian Journal of Remote Sensing 30, 17–25. https://doi.org/10.5589/m03-048

Gower, J.F.R., Borstad, G.A., 2004. On the potential of MODIS and MERIS for imaging chlorophyll fluorescence from space. International Journal of Remote Sensing 25, 1459–1464. https://doi.org/10.1080/01431160310001592445

Gower, J.F.R., Doerffer, R., Borstad, G.A., 1999. Interpretation of the 685nm peak in water-leaving radiance spectra in terms of fluorescence, absorption and scattering, and its observation by MERIS. International Journal of Remote Sensing 20, 1771–1786. https://doi.org/10.1080/014311699212470

Gradinger, R., 2009. Sea-ice algae: Major contributors to primary production and algal biomass in the Chukchi and Beaufort Seas during May/June 2002. Deep Sea Research Part II: Topical Studies in Oceanography 56, 1201–1212. https://doi.org/10.1016/j.dsr2.2008.10.016

Green, S.A., Blough, N.V., 1994. Optical absorption and fluorescence properties of chromophoric dissolved organic matter in natural waters. Limnology and Oceanography 39, 1903–1916. https://doi.org/10.4319/lo.1994.39.8.1903

Hegseth, E.N., Sundfjord, A., 2008. Intrusion and blooming of Atlantic phytoplankton species in the high Arctic. Journal of Marine Systems 74, 108–119. https://doi.org/10.1016/j.jmarsys.2007.11.011

Hessen, D.O., Carroll, J., Kjeldstad, B., Korosov, A.A., Pettersson, L.H., Pozdnyakov, D., Sørensen, K., 2010. Input of organic carbon as determinant of nutrient fluxes, light climate and productivity in the Ob and Yenisey estuaries. Estuarine, Coastal and Shelf Science 88, 53–62. https://doi.org/10.1016/j.ecss.2010.03.006

Hieronymi, M., 2019. Spectral band adaptation of ocean color sensors for applicability of the multi-water biogeo-optical algorithm ONNS. Optics Express 27, A707. https://doi.org/10.1364/OE.27.00A707

Hieronymi, M., Müller, D., Doerffer, R., 2017. The OLCI Neural Network Swarm (ONNS): A Bio-Geo-Optical Algorithm for Open Ocean and Coastal Waters. Frontiers in Marine Science 4, 140. https://doi.org/10.3389/fmars.2017.00140

Hill, V., Cota, G., Stockwell, D., 2005. Spring and summer phytoplankton communities in the Chukchi and Eastern Beaufort Seas. Deep Sea Research Part II: Topical Studies in Oceanography 52, 3369–3385. https://doi.org/10.1016/j.dsr2.2005.10.010

Hill, V.J., Light, B., Steele, M., Zimmerman, R.C., 2018. Light availability and phytoplankton growth beneath Arctic sea ice: Integrating observations and modeling. Journal of Geophysical Research: Oceans 123, 3651–3667. https://doi.org/10.1029/2017JC013617

Hill, V.J., Matrai, P.A., Olson, E., Suttles, S., Steele, M., Codispoti, L.A., Zimmerman, R.C., 2013. Synthesis of integrated primary production in the Arctic Ocean: II. In situ and remotely sensed estimates. Progress in Oceanography 110, 107–125. https://doi.org/10.1016/j.pocean.2012.11.005

Hill, V.J., Zimmerman, R.C., 2010. Estimates of primary production by remote sensing in the Arctic Ocean: Assessment of accuracy with passive and active sensors. Deep Sea Research Part I: Oceanographic Research Papers 57, 1243–1254. https://doi.org/10.1016/j.dsr.2010.06.011

Hooker, S.B., Morrow, J.H., Matsuoka, A., 2013. Apparent optical properties of the Canadian Beaufort Sea Part 2: The 1% and 1 cm perspective in deriving and validating AOP data products. Biogeosciences 10, 4511–4527. https://doi.org/10.5194/bg-10-4511-2013

Hooker, S.B., Zibordi, G., 2005. Platform perturbations in above-water radiometry. Applied Optics 44, 553. https://doi.org/10.1364/AO.44.000553

Huot, Y., 2004. Sun-induced fluorescence of phytoplankton in the ocean - linking physiology and remote sensing (PhD thesis). Dalhousie University, Halifax.

Huot, Y., Brown, C.A., Cullen, J.J., 2007. Retrieval of phytoplankton biomass from simultaneous inversion of reflectance, the diffuse attenuation coefficient, and Sun-induced fluorescence in coastal waters. Journal of Geophysical Research 112, C06013. https://doi.org/10.1029/2006JC003794

Huot, Y., Brown, C.A., Cullen, J.J., 2005. New algorithms for MODIS sun-induced chlorophyll fluorescence and a comparison with present data products: MODIS fluorescence algorithms. Limnology and Oceanography: Methods 3, 108–130. https://doi.org/10.4319/lom.2005.3.108

Jackson, T., Grant, M., 2016. Ocean Colour Algorithm Blending.

Janout, M.A., Hölemann, J., Waite, A.M., Krumpen, T., von Appen, W.-J., Martynov, F., 2016. Sea-ice retreat controls timing of summer plankton blooms in the Eastern Arctic Ocean. Geophysical Research Letters 43, 12–493. https://doi.org/10.1002/2016GL071232

Katlein, C., Arndt, S., Belter, H.J., Castellani, G., Nicolaus, M., 2019. Seasonal evolution of light transmission distributions through Arctic sea ice. Journal of Geophysical Research: Oceans 124, 5418–5435. https://doi.org/10.1029/2018JC014833

Katlein, C., Nicolaus, M., Petrich, C., 2014. The anisotropic scattering coefficient of sea ice. Journal of Geophysical Research: Oceans 119, 842–855. https://doi.org/10.1002/2013JC009502

Katlein, C., Perovich, D.K., Nicolaus, M., 2016. Geometric effects of an inhomogeneous sea ice cover on the under ice light field. Frontiers in Earth Science 4, 6. https://doi.org/10.3389/feart.2016.0000

Kiefer, D.A., Chamberlin, W.S., Booth, C.R., 1989. Natural fluorescence of chlorophyll a: Relationship to photosynthesis and chlorophyll concentration in the western South Pacific gyre. Limnology and Oceanography 34, 868–881. https://doi.org/10.4319/lo.1989.34.5.0868

Kishino, M., Takahashi, M., Okami, N., Ichimura, S., 1985. Estimation of the spectral absorption coefficients of phytoplankton in the sea. BULLETIN OF MARINE SCIENCE 37, 9.

Kostadinov, T.S., Siegel, D.A., Maritorena, S., Guillocheau, N., 2007. Ocean color observations and modeling for an optically complex site: Santa Barbara Channel, California, USA. Journal of Geophysical Research 112, C07011. https://doi.org/10.1029/2006JC003526

Lammers, R.B., Shiklomanov, A.I., Vörösmarty, C.J., Fekete, B.M., Peterson, B.J., 2001. Assessment of contemporary Arctic river runoff based on observational discharge records. Journal of Geophysical Research: Atmospheres 106, 3321–3334. https://doi.org/10.1029/2000JD900444

Laney, S.R., Krishfield, R.A., Toole, J.M., 2017. The euphotic zone under Arctic Ocean sea ice: Vertical extents and seasonal trends. Limnology and Oceanography 62, 1910–1934. https://doi.org/10.1002/lno.10543

Lee, Z., Carder, K.L., Arnone, R.A., 2002. Deriving inherent optical properties from water color: A multiband quasi-analytical algorithm for optically deep waters. Applied Optics 41, 5755. https://doi.org/10.1364/AO.41.005755

Lee, Z., Carder, K.L., Mobley, C.D., Steward, R.G., Patch, J.S., 1999. Hyperspectral remote sensing for shallow waters: 2 Deriving bottom depths and water properties by optimization. Applied Optics 38, 3831. https://doi.org/10.1364/AO.38.003831

Lee, Z., Hu, C., Shang, S., Du, K., Lewis, M., Arnone, R., Brewin, R., 2013. Penetration of UV-visible solar radiation in the global oceans: Insights from ocean color remote sensing: PENETRATION OF UV-VISIBLE SOLAR LIGHT. Journal of Geophysical Research: Oceans 118, 4241–4255. https://doi.org/10.1002/jgrc.20308

Lee, Z.-P., others, 2006. Remote sensing of inherent optical properties: Fundamentals, tests of algorithms, and applications. International Ocean Colour Coordinating Group (IOCCG). http://ioccg.org/wp-content/uploads/2015/10/ioccg-report-05.pdf

Legendre, P., 1998. Model II regression user's guide, r edition. R Vignette 14.

Lewis, K.M., Arrigo, K.R., 2020. Ocean Color Algorithms for Estimating Chlorophyll a, CDOM Absorption, and Particle Backscattering in the Arctic Ocean. Journal of Geophysical Research: Oceans 125, e2019JC015706. https://doi.org/10.1029/2019JC015706

Lewis, K.M., Mitchell, B.G., van Dijken, G.L., Arrigo, K.R., 2016. Regional chlorophyll a algorithms in the Arctic Ocean and their effect on satellite-derived primary production estimates. Deep Sea Research Part II: Topical Studies in Oceanography 130, 14–27. https://doi.org/10.1016/j.dsr2.2016.04.020

Lewis, K., Van Dijken, G., Arrigo, K., 2020. Bio-optical Database of the Arctic Ocean. https://doi.org/10.5061/DRYAD.CNP5HQC17

Lindsay, R., Schweiger, A., 2015. Arctic sea ice thickness loss determined using subsurface, aircraft, and satellite observations. The Cryosphere 9, 269–283. https://doi.org/10.5194/tc-9-269-2015

Lorenzen, C.J., 1966. A method for the continuous measurement of in vivo chlorophyll concentration. Deep Sea Research and Oceanographic Abstracts 13, 223–227. https://doi.org/10.1016/0011-7471(66)91102-8

Lowry, K.E., van Dijken, G.L., Arrigo, K.R., 2014. Evidence of under-ice phytoplankton blooms in the Chukchi Sea from 1998 to 2012. Deep Sea Research Part II: Topical Studies in Oceanography 105, 105–117. https://doi.org/10.1016/j.dsr2.2014.03.013

MacIntyre, H.L., Lawrenz, E., Richardson, T.L., 2010. Taxonomic discrimination of phytoplankton by spectral fluorescence, in: Chlorophyll a Fluorescence in Aquatic Sciences: Methods and Applications. Springer, pp. 129–169. https:/doi.org/10.1007/978-90-481-9268-7_7

Maritorena, S., d'Andon, O.H.F., Mangin, A., Siegel, D.A., 2010. Merged satellite ocean color data products using a bio-optical model: Characteristics, benefits and issues. Remote Sensing of Environment 114, 1791–1804. https://doi.org/10.1016/j.rse.2010.04.002

Maritorena, S., Siegel, D.A., Peterson, A.R., 2002. Optimization of a semianalytical ocean color model for global-scale applications. Applied Optics 41, 2705. https://doi.org/10.1364/AO.41.002705

Martin, J., Tremblay, J., Gagnon, J., Tremblay, G., Lapoussière, A., Jose, C., Poulin, M., Gosselin, M., Gratton, Y., Michel, C., 2010. Prevalence, structure and properties of subsurface chlorophyll maxima in Canadian Arctic waters. Marine Ecology Progress Series 412, 69–84. https://doi.org/10.3354/meps08666

Maslanik, J., Stroeve, J., Fowler, C., Emery, W., 2011. Distribution and trends in Arctic sea ice age through spring 2011. Geophysical Research Letters 38. https://doi.org/10.1029/2011GL047735

Matsuoka, A., Babin, M., Doxaran, D., Hooker, S.B., Mitchell, B.G., Bélanger, S., Bricaud, A., 2014. A synthesis of light absorption properties of the Arctic Ocean: Application to semianalytical estimates of dissolved organic carbon concentrations from space. Biogeosciences 11, 3131–3147. https://doi.org/10.5194/bg-11-3131-2014

Matsuoka, A., Boss, E., Babin, M., Karp-Boss, L., Hafez, M., Chekalyuk, A., Proctor, C.W., Werdell, P.J., Bricaud, A., 2017. Pan-Arctic optical characteristics of colored dissolved organic matter: Tracing dissolved organic carbon in changing Arctic waters using satellite ocean color data. Remote Sensing of Environment 200, 89–101. https://doi.org/10.1016/j.rse.2017.08.009

Matsuoka, A., Bricaud, A., Benner, R., Para, J., Sempéré, R., Prieur, L., Bélanger, S., Babin, M., 2012. Tracing the transport of colored dissolved organic matter in water masses of the Southern Beaufort Sea: Relationship with hydrographic characteristics. Biogeosciences 9, 925–940. https://doi.org/10.5194/bg-9-925-2012

Matsuoka, A., Hill, V., Huot, Y., Babin, M., Bricaud, A., 2011. Seasonal variability in the light absorption properties of western Arctic waters: Parameterization of the individual components of absorption for ocean color applications. Journal of Geophysical Research 116, C02007. https://doi.org/10.1029/2009JC005594

Matsuoka, A., Hooker, S.B., Bricaud, A., Gentili, B., Babin, M., 2013. Estimating absorption coefficients of colored dissolved organic matter (CDOM) using a semi-analytical algorithm for southern Beaufort Sea waters: Application to deriving concentrations of dissolved organic carbon from space. Biogeosciences 10, 917–927. https://doi.org/10.5194/bg-10-917-2013

Matsuoka, A., Huot, Y., Shimada, K., Saitoh, S.-I., Babin, M., 2007. Bio-optical characteristics of the western Arctic Ocean: Implications for ocean color algorithms. Canadian Journal of Remote Sensing 33, 503–518. https://doi.org/10.5589/m07-059

Matsuoka, A., Ortega-Retuerta, E., Bricaud, A., Arrigo, K.R., Babin, M., 2015. Characteristics of colored dissolved organic matter (CDOM) in the Western Arctic Ocean: Relationships with microbial activities. Deep Sea Research Part II: Topical Studies in Oceanography 118, 44–52. https://doi.org/10.1016/j.dsr2.2015.02.012

Matthes, L.C., Mundy, C.J., L-Girard, S., Babin, M., Verin, G., Ehn, J.K., 2020. Spatial heterogeneity as a key variable influencing spring-summer progression in UVR and PAR transmission through Arctic sea ice. Frontiers in Marine Science 7, 183. https://doi.org/10.3389/fmars.2020.00183

Matthes, L., Ehn, J., L-Girard, S., Pogorzelec, N., Babin, M., Mundy, C., Arrigo, K., 2019. Average cosine coefficient and spectral distribution of the light field under sea ice: Implications for primary production. Elementa: Science of the Anthropocene 7. https://doi.org/10.1525/elementa.363

Mayot, N., Matrai, P., Ellingsen, I., Steele, M., Johnson, K., Riser, S., Swift, D., 2018. Assessing phytoplankton activities in the seasonal ice zone of the Greenland Sea over an annual cycle. Journal of Geophysical Research: Oceans 123, 8004–8025. https://doi.org/10.1029/2018JC014271

McFarland, C.J., Jakuba, M.V., Suman, S., Kinsey, J.C., Whitcomb, L.L., 2015. Toward ice-relative navigation of underwater robotic vehicles under moving sea ice: Experimental evaluation in the arctic sea, in: 2015 IEEE International Conference on Robotics and Automation (ICRA). IEEE, pp. 1527–1534. https://doi.org/10.1109/ICRA.2015.7139392

Mebane Jr, W.R., Sekhon, J.S., 2011. Genetic optimization using derivatives: The rgenoud package for R. Journal of Statistical Software 42, 1–26. https://doi.org/10.18637/jss.v042.i11

Miller, R.L., Belz, M., Castillo, C.D., Trzaska, R., 2002. Determining CDOM absorption spectra in Diverse Aquatic Environment Using a multiple pathlength liquid core waveguide system. Continental Shelf Research 22, 1301–1310. https://doi.org/10.1016/S0278-4343(02)00009-2

Mitchell, B.G., 1992. Predictive bio-optical relationships for polar oceans and marginal ice zones. Journal of Marine Systems 3, 91–105. https://doi.org/10.1016/0924-7963(92)90032-4

Morel, A., 1978. Available usable and stored radiant energy in relation to marine photosynthesis. Deep Sea Research 25, 673–688. https://doi.org/10.1016/0146-6291(78)90623-9

Morel, A., 1974. Optical properties of pure water and pure sea water. Optical aspects of oceanography 1, 1–24.

Morel, A., Berthon, J.-F., 1989. Surface pigments, algal biomass profiles, and potential production of the euphotic layer: Relationships reinvestigated in view of remote-sensing applications. Limnology and oceanography 34, 1545–1562. https://doi.org/10.4319/lo.1989.34.8.1545

Morel, A., Bricaud, A., 1981. Theoretical Results Concerning the Optics of Phytoplankton, with Special Reference to Remote Sensing Applications. https://doi.org/10.1007/978-1-4613-3315-9_35

Morel, A., Huot, Y., Gentili, B., Werdell, P.J., Hooker, S.B., Franz, B.A., 2007. Examining the consistency of products derived from various ocean color sensors in open ocean (Case 1) waters in the perspective of a multi-sensor approach. Remote Sensing of Environment 111, 69–88. https://doi.org/10.1016/j.rse.2007.03.012

Morel, A., Maritorena, S., 2001. Bio-optical properties of oceanic waters: A reappraisal. Journal of Geophysical Research: Oceans 106, 7163–7180. https://doi.org/10.1029/2000JC000319

Morel, A., Prieur, L., 1977. Analysis of variations in ocean Color1: Ocean color analysis. Limnology and Oceanography 22, 709–722. https://doi.org/10.4319/lo.1977.22.4.0709

Morrison, J.R., Goodwin, D.S., 2010. Phytoplankton photocompensation from space-based fluorescence measurements. Geophysical Research Letters 37. https://doi.org/10.1029/2009GL041799

Mu, X., Shen, Q., Li, Z.-L., Yan, G., Sobrino, J.A., 2011. A comparison of different optimization algorithms for retrieving aerosol optical depths from satellite data: An example of using a dual-angle algorithm. International Journal of Remote Sensing 32, 8949–8968. https://doi.org/10.1080/01431161.2010.531780

Mullen, K., Ardia, D., Gil, D.L., Windover, D., Cline, J., 2011. DEoptim: An R package for global optimization by differential evolution. Journal of Statistical Software 40, 1–26. https://ssrn.com/abstract=1526466

Mundy, C.J., Gosselin, M., Ehn, J., Gratton, Y., Rossnagel, A., Barber, D.G., Martin, J., Tremblay, J.-É., Palmer, M., Arrigo, K.R., Darnis, G., Fortier, L., Else, B., Papakyriakou, T., 2009. Contribution of under-ice primary production to an ice-edge upwelling phytoplankton bloom in the Canadian Beaufort Sea. Geophysical Research Letters 36, L17601. https://doi.org/10.1029/2009GL038837

Mundy, C.J., Gosselin, M., Gratton, Y., Brown, K., Galindo, V., Campbell, K., Levasseur, M., Barber, D., Papakyriakou, T., Bélanger, S., 2014. Role of environmental factors on phytoplankton bloom initiation under landfast sea ice in Resolute Passage, Canada. Marine Ecology Progress Series 497, 39–49. https://doi.org/10.3354/meps10587

Mustapha, S.B., Bélanger, S., Larouche, P., 2012. Evaluation of ocean color algorithms in the southeastern Beaufort Sea, Canadian Arctic: New parameterization using SeaWiFS, MODIS, and MERIS spectral bands. Canadian Journal of Remote Sensing 38, 535–556. https://doi.org/10.5589/m12-045

Naik, P., D'Sa, E.J., Goés, J.I., Gomes, H.R., 2010. Assessment of particulate absorption properties in the southeastern Bering Sea from in-situ and remote sensing data. Journal of Applied Remote Sensing 4, 043561. https://doi.org/10.1117/1.3525572

Neville, R.A., Gower, J.F.R., 1977. Passive remote sensing of phytoplankton via chlorophyll α fluorescence. Journal of Geophysical Research 82, 3487–3493. https://doi.org/10.1029/JC082i024p03487

Niebauer, H., Alexander, V., Henrichs, S.M., 1995. A time-series study of the spring bloom at the Bering Sea ice edge I. Physical processes, chlorophyll and nutrient chemistry. Continental Shelf Research 15, 1859–1877. https://doi.org/10.1016/0278-4343(94)00097-7

O'Reilly, J.E., Maritorena, S., Mitchell, B.G., Siegel, D.A., Carder, K.L., Garver, S.A., Kahru, M., McClain, C., 1998. Ocean color chlorophyll algorithms for SeaWiFS. Journal of Geophysical Research: Oceans 103, 24937–24953. https://doi.org/10.1029/98JC02160

O'Reilly, J.E., Maritorena, S., Siegel, D.A., O'Brien, M.C., Toole, D., Mitchell, B.G., Kahru, M., Chavez, F.P., Strutton, P., Cota, G.F., Hooker, S.B., McClain, C.R., Carder, K.L., Muller-Karger, F., Harding, L., Magnuson, A., Phinney, D., Moore, G.F., Aiken, J., Arrigo, K.R., Letelier, R., Culver, M., 2000. Ocean Color Chlorophyll a Algorithms for SeaWiFS, OC2 and OC4: Version 4. Journal of Geophysical Research: Oceans 103, 15. https://doi.org/10.1029/98JC02160

Onarheim, I.H., Eldevik, T., Smedsrud, L.H., Stroeve, J.C., 2018. Seasonal and Regional Manifestation of Arctic Sea Ice Loss. Journal of Climate 31, 4917–4932. https://doi.org/10.1175/JCLI-D-17-0427.1

Overeem, I., Syvitski, J.P.M., 2010. Shifting discharge peaks in arctic rivers, 1977. Geografiska Annaler: Series A, Physical Geography 92, 285–296. https://doi.org/10.1111/j.1468-0459.2010.00395.x

Pabi, S., van Dijken, G.L., Arrigo, K.R., 2008. Primary production in the Arctic Ocean, 1998. Journal of Geophysical Research 113, C08005. https://doi.org/10.1029/2007JC004578

Parkinson, C.L., Comiso, J.C., 2013. On the 2012 record low Arctic sea ice cover: Combined impact of preconditioning and an August storm. Geophysical Research Letters 40, 1356–1361. https://doi.org/10.1002/grl.50349

Perovich, D., Jones, K., Light, B., Eicken, H., Markus, T., Stroeve, J., Lindsay, R., 2011. Solar partitioning in a changing Arctic sea-ice cover. Annals of Glaciology 52, 192–196. https://doi.org/doi:10.3189/172756411795931543

Perrette, M., Yool, A., Quartly, G.D., Popova, E.E., 2010. Near-ubiquity of ice-edge blooms in the Arctic. Biogeosciences Discussions 7, 8123–8142. https://doi.org/10.5194/bgd-7-8123-2010

Peterson, B.J., Holmes, R.M., McClelland, J.W., Vörösmarty, C.J., Lammers, R.B., Shiklomanov, A.I., Shiklomanov, I.A., Rahmstorf, S., 2002. Increasing River Discharge to the Arctic Ocean. Science 298, 2171–2173. https://doi.org/10.1126/science.1077445

Platt, T., Gallegos, C.L., 1980. Modelling primary production. Springer 339–362. https://doi.org/10.1007/978-1-4684-3890-1_19

Pommier, J., Gosselin, M., Michel, C., 2009. Size-fractionated phytoplankton production and biomass during the decline of the northwest Atlantic spring bloom. Journal of plankton research 31, 429–446. https://doi.org/10.1093/plankt/fbn127

Pope, R.M., Fry, E.S., 1997. Absorption spectrum (380 nm) of pure water II Integrating cavity measurements. Applied Optics 36, 8710. https://doi.org/10.1364/AO.36.008710

Randelhoff, A., Oziel, L., Massicotte, P., Bécu, G., Galí, M., Lacour, L., Dumont, D., Vladoiu, A., Marec, C., Bruyant, F., others, 2019. The evolution of light and vertical mixing across a phytoplankton ice-edge bloom. Elementa: Science of the Anthropocene 7. https://doi.org/10.1525/elementa.357

Ras, J., Claustre, H., Uitz, J., 2008. Spatial variability of phytoplankton pigment distributions in the Subtropical South Pacific Ocean: Comparison between in situ and predicted data. Biogeosciences 5, 353–369. https://doi.org/10.5194/bg-5-353-2008

Raymond, P.A., McClelland, J.W., Holmes, R.M., Zhulidov, A.V., Mull, K., Peterson, B.J., Striegl, R.G., Aiken, G.R., Gurtovaya, T.Y., 2007. Flux and age of dissolved organic carbon exported to the Arctic Ocean: A carbon isotopic study of the five largest arctic rivers: ARCTIC RIVER DOC. Global Biogeochemical Cycles 21, n/a–n/a. https://doi.org/10.1029/2007GB002934

Reynolds, R.A., Stramski, D., Neukermans, G., 2016. Optical backscattering by particles in Arctic seawater and relationships to particle mass concentration, size distribution, and bulk composition: Particle backscattering in Arctic seawater. Limnology and Oceanography 61, 1869–1890. https://doi.org/10.1002/lno.10341

Roesler, C.S., Boss, E., n.d. 5 In Situ Measurement of the Inherent Optical Properties (IOPs) and Potential for Harmful Algal Bloom Detection and Coastal Ecosystem Observations 68.

Sathyendranath, S., Cota, G., Stuart, V., Maass, H., Platt, T., 2001. Remote sensing of phytoplankton pigments: A comparison of empirical and theoretical approaches. International Journal of Remote Sensing 22, 249–273. https://doi.org/10.1080/014311601449925

Sathyendranath, S., others, 2014. Phytoplankton functional types from Space. International Ocean Colour Coordinating Group (IOCCG). http://ioccg.org/wp-content/uploads/2018/09/ioccg_report_15_2014.pdf

Sathyendranath, S., Platt, T., Irwin, B., Horne, E., Borstad, G., Stuart, V., Payzant, L., Maass, H., Kepkay, P., Li, W., others, 2004. A multispectral remote sensing study of coastal waters off Vancouver Island. International Journal of Remote Sensing 25, 893–919. https://doi.org/10.1080/0143116031000139836

Screen, J.A., Simmonds, I., 2010. The central role of diminishing sea ice in recent Arctic temperature amplification. Nature 464, 1334–1337. https://doi.org/10.1038/nature09051

Seegers, B.N., Stumpf, R.P., Schaeffer, B.A., Loftin, K.A., Werdell, P.J., 2018. Performance metrics for the assessment of satellite data products: An ocean color case study. Optics Express 26, 7404. https://doi.org/10.1364/OE.26.007404

Serreze, M.C., Barrett, A.P., Stroeve, J.C., Kindig, D.N., Holland, M.M., 2009. The emergence of surface-based Arctic amplification. The Cryosphere 3, 11–19. https://doi.org/10.5194/tc-3-11-2009

Serreze, M.C., Holland, M.M., Stroeve, J., 2007. Perspectives on the Arctic's Shrinking Sea-Ice Cover. Science 315, 1533–1536. https://doi.org/10.1126/science.1139426

Shang, S., Lee, Z., Lin, G., Li, Y., Li, X., 2019. Progressive scheme for blending empirical ocean color retrievals of absorption coefficient and chlorophyll concentration from open oceans to highly turbid waters. Applied Optics 58, 3359. https://doi.org/10.1364/AO.58.003359

Son, Y.-S., Kim, H., 2018. Empirical ocean color algorithms and bio-optical properties of the western coastal waters of Svalbard, Arctic. ISPRS Journal of Photogrammetry and Remote Sensing 139, 272–283. https://doi.org/10.1016/j.isprsjprs.2018.03.024

Stramska, M., Stramski, D., Hapter, R., Kaczmarek, S., Stoń-Egiert, J., 2003. Bio-optical relationships and ocean color algorithms for the north polar region of the Atlantic. Journal of Geophysical Research 108, 3143. https://doi.org/10.1029/2001JC001195

Stramski, D., Reynolds, R.A., Kaczmarek, S., Uitz, J., Zheng, G., 2015. Correction of pathlength amplification in the filter-pad technique for measurements of particulate absorption coefficient in the visible spectral region. Applied Optics 54, 6763. https://doi.org/10.1364/AO.54.006763

Stroeve, J.C., Serreze, M.C., Holland, M.M., Kay, J.E., Malanik, J., Barrett, A.P., 2012. The Arctic's rapidly shrinking sea ice cover: A research synthesis. Climatic Change 110, 1005–1027. https://doi.org/10.1007/s10584-011-0101-1

Stroeve, J., Holland, M.M., Meier, W., Scambos, T., Serreze, M., 2007. Arctic sea ice decline: Faster than forecast: ARCTIC ICE LOSS-FASTER THAN FORECAST. Geophysical Research Letters 34. https://doi.org/10.1029/2007GL029703

Stroeve, J., Markus, T., Boisvert, L., Miller, J., Barrett, A., 2014. Changes in Arctic melt season and implications for sea ice loss. Geophysical Research Letters 41, 1216–1225. https://doi.org/10.1002/2013GL058951

Tremblay, J.-É., Bélanger, S., Barber, D.G., Asplin, M., Martin, J., Darnis, G., Fortier, L., Gratton, Y., Link, H., Archambault, P., Sallon, A., Michel, C., Williams, W.J., Philippe, B., Gosselin, M., 2011. Climate forcing multiplies biological productivity in the coastal Arctic Ocean: Upwelling and productivity in the Arcti. Geophysical Research Letters 38. https://doi.org/10.1029/2011GL048825

Tremblay, J.-E., Michel, C., Hobson, K.A., Gosselin, M., Price, N.M., 2006. Bloom dynamics in early opening waters of the Arctic Ocean. Limnology and Oceanography 51, 900–912. https://doi.org/10.4319/lo.2006.51.2.0900

Uchimiya, M., Motegi, C., Nishino, S., Kawaguchi, Y., Inoue, J., Ogawa, H., Nagata, T., 2016. Coupled Response of Bacterial Production to a Wind-Induced Fall Phytoplankton Bloom and Sediment Resuspension in the Chukchi Sea Shelf, Western Arctic Ocean. Frontiers in Marine Science 3. https://doi.org/10.3389/fmars.2016.002

Van Heukelem, L., Thomas, C.S., 2001. Computer-assisted high-performance liquid chromatography method development with applications to the isolation and analysis of phytoplankton pigments. Journal of Chromatography A 910, 31–49. https://doi.org/10.1016/S0378-4347(00)00603-4

Vermaire, J.C., Pisaric, M.F.J., Thienpont, J.R., Courtney Mustaphi, C.J., Kokelj, S.V., Smol, J.P., 2013. Arctic climate warming and sea ice declines lead to increased storm surge activity. Geophysical Research Letters 40, 1386–1390. https://doi.org/10.1002/grl.50191

Vörösmarty, C.J., Fekete, B.M., Meybeck, M., Lammers, R.B., 2000. Global system of rivers: Its role in organizing continental land mass and defining land-to-ocean linkages. Global Biogeochemical Cycles 14, 599–621. https://doi.org/10.1029/1999GB900092

Wadhams, P., 2012. Arctic Ice Cover, Ice Thickness and Tipping Points. AMBIO 41, 23–33. https://doi.org/10.1007/s13280-011-0222-9

Wang, J., Cota, G.F., 2003. Remote-sensing reflectance in the Beaufort and Chukchi seas: Observations and models. Applied Optics 42, 2754. https://doi.org/10.1364/AO.42.002754

Wang, J., Cota, G.F., Ruble, D.A., 2005. Absorption and backscattering in the Beaufort and Chukchi Seas. Journal of Geophysical Research 110, C04014. https://doi.org/10.1029/2002JC001653

Wang, M., Liu, X., Tan, L., Jiang, L., Son, S., Shi, W., Rausch, K., Voss, K., 2013. Impacts of VIIRS SDR performance on ocean color products: VIIRS OCEAN COLOR PRODUCTS. Journal of Geophysical Research: Atmospheres 118, 10, 347–10, 360. https://doi.org/10.1002/jgrd.50793

Wang, M., Overland, J.E., 2012. A sea ice free summer Arctic within 30 years: An update from CMIP5 models: SUMMER ARCTIC SEA ICE. Geophysical Research Letters 39. https://doi.org/10.1029/2012GL052868

Wang, M., Son, S., Shi, W., 2009. Evaluation of MODIS SWIR and NIR-SWIR atmospheric correction algorithms using SeaBASS data. Remote Sensing of Environment 113, 635–644. https://doi.org/10.1016/j.rse.2008.11.005

Werdell, P.J., Franz, B.A., Bailey, S.W., Feldman, G.C., Boss, E., Brando, V.E., Dowell, M., Hirata, T., Lavender, S.J., Lee, Z., others, 2013. Generalized ocean color inversion model for retrieving marine inherent optical properties. Applied optics 52, 2019–2037. https://doi.org/10.1364/AO.52.002019

Williams, W.J., Carmack, E.C., 2008. Combined effect of wind-forcing and isobath divergence on upwelling at Cape Bathurst, Beaufort Sea. Journal of Marine Research 66, 645–663. https://doi.org/10.1357/002224008787536808

Winder, M., Sommer, U., 2012. Phytoplankton response to a changing climate. Hydrobiologia 698, 5–16. https://doi.org/10.1007/s10750-012-1149-2

Xiang, Y., Gubian, S., Martin, F., 2017. Generalized simulated annealing. Computational Optimization in Engineering-Paradigms and Applications 25–46. https://doi.org/http://dx.doi.org/10.5772/66071

Xiang, Y., Gubian, S., Suomela, B., Hoeng, J., 2013. Generalized Simulated Annealing for Global Optimization: The GenSA Package. The R Journal 5, 13. https://doi.org/10.32614/RJ-2013-002

Xing, X.-G., Zhao, D.-Z., Liu, Y.-G., Yang, J.-H., Xiu, P., Wang, L., 2007. An overview of remote sensing of chlorophyll fluorescence. Ocean Science Journal 42, 49–59. https://doi.org/10.1007/BF03020910

Zheng, G., Stramski, D., Reynolds, R.A., 2014. Evaluation of the Quasi-Analytical Algorithm for estimating the inherent optical properties of seawater from ocean color: Comparison of Arctic and lower-latitude waters. Remote Sensing of Environment 155, 194–209. https://doi.org/10.1016/j.rse.2014.08.020